

Application of Microwave Techniques in Breast Imaging

Guangran Zhu



Department of Electrical & Computer Engineering
McGill University
Montreal, Canada

May 2011

A thesis submitted to McGill University in partial fulfilment of the requirements for the degree of Doctor of Philosophy.

© 2011 Guangran Zhu

Abstract

The detection of breast cancer at its early stage reduces the treatment cost and the mortality rate. Microwave imaging techniques have been proposed to complement the existing X-ray mammography to screen women. They exploit the dielectric contrast between malignant and healthy tissue in the microwave range.

The first subject of this thesis is to solve the problem of a plane wave scattered by a multi-layer sphere. From this model and the recent measurements of the dielectric properties of the breast tissue, we predict the strength of this response as the tumors are buried in different tissues. These results identify the requirements on the microwave radar systems for breast tumor detection.

The second subject of this thesis is to use a commercial software, SEMCAD, to construct numerical breast models. We use the classification and regression tree analysis to approximate the heterogeneous tissue region, which averages out the noise inherited in the magnetic resonance images and reduces the number of solids to fill the tissue region. These breast models can be combined with complex antennas for full-wave electromagnetic simulations.

A numerical evaluation of the microwave radar and microwave-induced thermoacoustic imaging technique is presented. We find that the contrast in radar signals is due to permittivity and conductivity, while the contrast in thermoacoustic signals is due to conductivity-heat capacity ratio. Due to the wave physics and the fact that human breast is electrically heterogeneous but acoustically homogeneous, images acquired from the thermoacoustic signals exhibit better quality than the images from the radar signals.

Finally, we show that the antennas in microwave tomographic systems are for transmitting and receiving microwave signals, and the antennas in microwave-induced thermoacoustic systems are for heating. It is not feasible to construct a single system with antennas that simultaneously meet the requirements of these two systems.

Resumé

La détection du cancer du sein au stade précoce réduit le coût du traitement et le taux de mortalité. Les techniques d'imagerie micro-ondes ont été proposées pour compléter la mammographie existante par rayon X pour ausculter les femme. Ils exploitent le contraste diélectrique entre le tissu malin et le tissu sain dans le champ des micro-ondes.

Le premier objet de cette thèse est de résoudre le problème d'une onde plane diffusée par une sphère multicouche. A partir de ce modèle et les mesures récentes des propriétés diélectriques du tissu mammaire, nous pouvons également prédire la grandeur de cette réponse car les tumeurs sont enterrées dans différents tissus. Ces résultats mettent en évidence les critères exigés avec des systèmes radar à micro-ondes pour la détection de tumeur du sein.

Le deuxième objet de cette thèse est d'utiliser un logiciel commercial, SEMCAD, pour construire des modèles numériques du sein. Nous utilisons la classification et l'analyse par arborescence pour estimer approximativement la zone de tissu hétérogène, ce qui représente en moyenne le bruit dans les images héritées par résonance magnétique et réduit le nombre de matières solides pour remplir la zone de tissu. Ces modèles du sein peuvent être combinés avec des antennes complexes pour des simulations complètes par ondes électromagnétiques.

Une évaluation numérique du radar micro-ondes des micro-ondes induites par la technique d'imagerie thermo-acoustique est présentée. Il est constaté que le contraste dans les signaux radar est dû à la permittivité et à la conductivité, tandis que le contraste dans les signaux thermo-acoustiques est dû au rapport entre la capacité de la chaleur et celle de la conductivité. En raison de la physique des ondes et du fait que le sein maternel humain est électriquement hétérogène mais acoustiquement homogène, les images acquises à partir des signaux thermo-acoustiques présentent une plus grande qualité que les images obtenues à partir des signaux radar.

Enfin, nous montrons que les antennes dans les systèmes à micro-ondes tomographiques

sont pour transmettre et recevoir des signaux micro-ondes, et les antennes micro-ondes induite par les systèmes thermo-acoustiques sont pour le chauffage. Il n'est pas possible de construire un système unique avec des antennes qui peut répondre simultanément aux exigences de ces deux systèmes.

Acknowledgements

I was fortunate to work with many ingenious people over the course of pursuing the Ph.D. degree at McGill University.

For the foremost, I thank Prof. Milica Popović for introducing me this exciting research topic. I learnt a great deal from her on how to do research, how to manage time, the need to have an open mind, and the need to have a good writing skill, all of which will benefit my career down the path.

My deepest gratitude also goes to Prof. Mark Coates, who has been a great role model in research. Also, his feedback greatly improved this work and strengthened my confidence.

I was fortunate to work with several people on the projects related to this thesis. In particular, I thank Dr. Qianqian Fang for his timely assistance in microwave tomography, when my research appeared stagnant. I thank Emily Porter with whom I worked on the construction of the breast models, Dr. Boris Oreshkin with whom I worked on the tissue property assignment and the general-likelihood detection algorithm, Evgeny Kirshin with whom I worked on the joint-detection scheme and frequency-domain beamforming algorithm, and Adam Santorelli with whom I worked on the numerical simulation using SEMCAD.

Several people have contributed to the growth of my knowledge inside and outside of the McGill community. Inside McGill, I thank Prof. Benoît Champagne and Prof. Ramesh Abhari for serving on my Ph.D. qualification exam and thesis proposal committee. I thank Prof. Jon Webb who provided insight on the electromagnetic scattering problems and functional analysis, and Prof. David Lowther for several constructive discussions on software engineering and optimization theory. In the office, I thank Dr. Houssam Kanj for being a great senior who helped me get started with microwave breast imaging in the early years, and shared his knowledge in ultra-wideband antenna designs. I express my gratitude to Dr. Asanee Suntives and Dr. Zhaolong Li, whose expert knowledge in

microwave engineering put my research on the physical ground, and Dr. Abhay Ghatpande who generously passed on his knowledge in administration of Linux clusters. I also shared constructive discussions with David Fernández Becerra on hardware-accelerated numerical simulations, with Dr. Helder Pinheiro on the finite-element methods and light scattering of small particles, and with Adrian Ngoly on the computation of special functions and the derivation of the results in Appendix A. For these, I am very grateful.

Outside McGill, I thank Dr. Guilin Sun from Lumerical Solutions Inc., for his inspiration in the finite-difference time-domain methods and his guidance on how to identify problems in research. I also thank Prof. John Schneider from Washington State University, who generously worked with me to iron out the technical details to implement the total-field scattered-field boundary using the analytic field propagation method. Dr. Stefan Schild and Dr. Chung-Huan Li from SPEAG assisted me in mastering SEMCAD and shared several discussions on the engineering issues of microwave-induced thermoacoustic systems. Dr. Hassan Rivaz from Johns Hopkins University greatly extended my general knowledge in medical imaging and particularly in ultrasound imaging. Dr. Jun Chen from University of Waterloo has been influential in my perspective on programming languages and computer architecture.

In addition to the aforementioned people, I also thank Maryam Golshayan, Huanhuan Gu, Amir Hajiabli, Min Li, Maryam Mehri, Hussein Moghnieh, Jun Ouyang, Prakash Paul, Dani Tannir, and Jian Wang who have kept the office life enjoyable.

Finally, I thank the support from my parents Huixian Yan and Wenzhao Zhu. Only with their love, I could overcome the fear from the World of Unknowns and move forward to enjoy the excitement of every discovery. I also thank my mother-in-law Haoying Li, who has been a great role model in life. I express my deepest gratitude to my wife Mengyao Li, who has been a strong supporter in both work and life. Without her, this work would not be possible.

Contents

Abstract	i
Resumé	ii
Acknowledgement	iv
Contents	viii
List of Figures	xiii
List of Tables	xiv
List of Abbreviations and Acronyms	xv
List of Notation	xvi
1 Introduction	1
1.1 Research Objectives	2
1.2 Thesis Contributions	3
1.3 Thesis Outline	4
2 Imaging Techniques for Breast Cancer	5
2.1 X-ray Mammography	6
2.2 Magnetic Resonance Imaging	7
2.3 Ultrasound Imaging	8
2.4 Dielectric Properties of the Human Breast	10
2.5 Microwave Imaging Techniques for Breast Cancer	11

2.5.1	Microwave Radar Imaging	11
2.5.2	Microwave Tomographic Imaging	14
2.5.3	Microwave-Induced Thermoacoustic Imaging	16
2.5.4	Microwave Elastic Imaging	17
2.6	Summary	18
3	Requirements on Microwave Radar Systems	19
3.1	Scattering of a Multi-layer Sphere	20
3.1.1	Solution Overview	20
3.1.2	Potentials and Construction of Solutions	21
3.1.3	Helmholtz's Equation in a Spherical Coordinate System	23
3.1.4	Wave Transformation	25
3.1.5	Boundary Conditions	27
3.1.6	System of Equations and its Solution	29
3.2	Implementation and Validation	30
3.3	Results	32
3.4	Conclusions	36
4	Building Numerical Breast Models	40
4.1	Model Construction	42
4.1.1	Image Segmentation	42
4.1.2	Tissue Approximation	43
4.1.3	Selection of the Complexity Penalty	46
4.1.4	Assignment of the Dielectric Properties	46
4.2	An Example	48
4.3	Comparison of the Dielectric and Debye Model	49
4.4	Conclusions	53
5	Comparison of Image Quality of Microwave Radar and Microwave-Induced Thermoacoustics	55
5.1	Physics of Microwave Radar and Microwave-Induced Thermoacoustics . . .	57
5.2	Endogenous Properties of the Human Breast	61
5.3	Numerical Modelling	64
5.3.1	Duality in Electromagnetic and Acoustic Wave Equations	65

5.3.2	Material Modelling	67
5.3.3	Thermoacoustic Wave of a Uniformly-Heated Cylinder	68
5.4	Comparison of Signals	70
5.5	Delay-And-Sum Algorithm	72
5.6	Imaging Results	75
5.6.1	Homogeneous Medium with One Inclusion	75
5.6.2	Homogeneous Medium with Two Inclusions	80
5.6.3	A Heterogeneous Breast Model	81
5.7	Conclusions	81
6	Microwave-Induced Thermoacoustics Assisting Microwave Tomography	89
6.1	System Design and Imaging Algorithm	90
6.2	Engineering Consideration	94
6.3	Conclusions	95
7	Summary	96
7.1	Thesis Contributions	96
7.2	Future Works	97
7.2.1	Measurements of Dielectric Properties	97
7.2.2	Contrast-Enhanced Microwave Imaging	97
7.2.3	Contrast Resolution Trade-off in Microwave Radar Imaging	98
A	Proof of (3.23)	99
	References	103

List of Figures

1.1	Drawing of the cross section of a human breast. The adipose tissue, glandular tissue (lobules), ducts are labelled. The fibrous connective tissue connects the gland and adipose tissue (not shown). The picture is adopted from [105].	2
2.1	X-ray attenuation as it passes through bone, skeletal muscle, average breast tissue, and adipose.	7
3.1	An x -polarized plane wave, propagating in the z direction, impinges upon an L -layer sphere. Starting from the inner core, each layer is characterized by its radius, permittivity, and permeability.	21
3.2	A plane wave propagating in the z direction expressed in terms of the spherical basis functions.	26
3.3	Normalized mono-static radar cross section of a dielectric sphere with a relative permittivity of 2.25 and a radius of one background wavelength [30].	32
3.4	Total field of (a) $ H_r $ and (b) $ H_\theta $ as the x -polarized plane wave interacts with a three-layer dielectric sphere with the relative permittivity of 2, 8 and 4 and the radii of 1.5, 1 and 0.6 of a background wavelength.	33
3.5	Reflected power as the surrounding tissue being (a) 40 mm, (b) 50 mm, and (c) 60 mm thick.	35
3.6	Differential power due to the presence of a tumor with the tissue being 40-mm thick and containing (a) 0-30%, (b) 31-85%, and (c) 86-100% of adipose.	37
3.7	Differential power due to the presence of a tumor with the tissue being 50-mm thick and containing (a) 0-30%, (b) 31-85%, and (c) 86-100% of adipose.	38
3.8	Differential power due to the presence of a tumor with the tissue being 60-mm thick and containing (a) 0-30%, (b) 31-85%, and (c) 86-100% of adipose.	39

4.1	Components commonly involved in an electromagnetic software. The direction of the arrow indicates the work flow.	41
4.2	A tomographic image of a patient's upper body, the segmented image (the black stroke traces out the skin), and the skin and tissue wire frames. . . .	43
4.3	A one-dimensional example to demonstrate the growing and pruning of the regression tree. The growing process (on the left) involves successive partitioning of a parent node by minimizing the mean-squared error of its two child nodes. The pruning process (on the right) involves comparing the mean-squared error of the parent node, the sum of the mean-squared errors of the child nodes, and the complexity penalty. If the mean-squared error of the parent node is smaller, the two child nodes are pruned.	45
4.4	Two-component Gaussian mixture model used to fit the distribution of the voxel intensity of a magnetic resonance image. The 25 th , 50 th , and 75 th percentile of each component are labelled. These critical percentiles determine the boundaries for the piecewise mapping from the voxel intensities to the Debye parameters. Voxel intensities falling within these boundaries are linearly mapped to the Debye parameters. The mapping to ϵ_∞ , σ_s and $\Delta\epsilon$ are shown in the top three graphs.	47
4.5	Relation between the empirical risk and the number of leaf nodes in the regression tree. Each point on the trace corresponds to a pruned tree. The label next to each point is the value of the complexity penalty. When the empirical risk is 0 and the complexity penalty is 0, the number of leaf nodes is 205,190 in this example.	49
4.6	Breast tissue filled with (a) 534 solids when the complexity penalty is 5×10^5 , and (b) 90 solids when the complexity penalty is 4×10^6	50
4.7	Screen shot of a breast model inside SEMCAD. The top layer is 5-mm thick muscle, followed by 3-mm thick fat. The tissue is filled with a set of solids identified through the regression analysis. The skin layer around the tissue is obtained by manually segmenting the magnetic resonance images. The average skin thickness is 1.5 mm.	50

4.8	Sagittal cross section showing the dielectric properties obtained by evaluating the Debye model at 6 GHz. (a) and (c) show the relative permittivity and conductivity mapped directly from a magnetic resonance image, voxel-by-voxel. (b) and (d) show the relative permittivity and conductivity when we fill the tissue with 1177 solids.	51
4.9	Attenuation of the tissue containing 0-30% adipose and the lower bound. The dielectric material is specified at a relative permittivity of 41 and a conductivity of 6.5 S/m.	52
4.10	Top view of the simulation scenario. The breast is surrounded by four antennas positioned 20 mm below the skin layer and at (0,-70 mm), (-70 mm,0), (0,70 mm) and (70 mm,0).	53
4.11	Received signals at Antenna C with dielectric and Debye materials in the tissue region (a) frequency-domain signals and (b) time-domain signals. . .	54
5.1	(a) Illustration of the microwave radar technique. An antenna radiates a wideband pulse towards the breast. After scattering, the pulse is received by the antenna. The locations of the scatterers are identified from the received signal. (b) A typical microwave pulse with a bandwidth from 3.1 GHz to 10.6 GHz. The half-magnitude width is 0.1 ns.	58
5.2	(a) Illustration of the microwave-induced thermoacoustic technique. A uniform field is created inside the breast, and each point becomes a source emitting acoustic signals, which are detected by the transducer. (b) Shape of the Gaussian-modulated continuous wave used to excite the thermoacoustic process. The envelope has a half-magnitude width of 0.5 μ s.	59
5.3	Dielectric properties of the six types of tissue, tumor, and skin listed Table 5.1 (a) relative permittivity and (b) effective conductivity.	63
5.4	Yee cell for the (a) electromagnetic and (b) acoustic FDTD simulations. . .	65
5.5	Thermoacoustic signal generated from a uniformly heated cylinder, (a) numerical evaluation of the Green function solution and (b) the FDTD result. . .	69
5.6	Contrast in (a) permittivity and (b) conductivity between the malignant and healthy tissue listed in Table 5.1.	71
5.7	A one-dimensional example with a three-layer slab to illustrate the contrast in the conductivity-heat capacity ratio in the thermoacoustic signals. . . .	73

5.8	Comparison of the simulated result of the one-dimensional example with the SCR defined in (5.24).	73
5.9	(a) A mono-static microwave radar system. There are 36 current sources (marked as “×”) placed 20 mm away from the circular object radiating sequentially. (b) A microwave-induced thermoacoustic system. The object is uniformly excited. There are 80 transducers (marked as “■”) placed 20 mm away from the object simultaneously recording the thermoacoustic signals.	76
5.10	Cross-image SCR of (a) radar images and (b) thermoacoustic images. . . .	77
5.11	Radar images from the DAS algorithm attempting to resolve two closely spaced inclusions in a homogeneous medium with (a) tissue being of Type III and (b) tissue being of Type IV as defined in Table 5.1.	79
5.12	Radar image from the FDB algorithm attempting to resolve two closely spaced inclusions in a homogeneous medium with tissue being of Type III as defined in Table 5.1.	83
5.13	Thermoacoustic images from the DAS algorithm attempting to resolve two closely spaced inclusions in a homogeneous medium with (a) tissue being of Type III and (b) tissue being of Type IV as defined in Table 5.1.	84
5.14	A circularly cropped T1-weighted magnetic resonance image.	85
5.15	Dielectric properties of the breast model constructed from the magnetic resonance image evaluated at 6.85 GHz (a) relative permittivity and (b) effective conductivity.	86
5.16	Normalized space-dependent conductivity-heat capacity ratio, where the effective conductivity is evaluated at 550 MHz.	87
5.17	Thermoacoustic image generated from the DAS algorithm.	87
5.18	Radar images generated from (a) the DAS algorithm and (b) the FDB algorithm.	88
6.1	(a) A non-uniform mesh extracted from a thermoacoustic image, in which the region with the possible presence of tumor is resolved with more elements. There are 120 nodes and 213 elements. (b) A uniform mesh, in which all regions are resolved with elements of approximately the same dimension. There are 118 nodes and 199 elements.	91

6.2	Flow chart to demonstrate the solution to the inverse problem using the gradient-based optimization methods.	92
-----	---	----

List of Tables

2.1	Acoustic properties of the breast tissue, tumor, body adipose, and water (The attenuation coefficient is evaluated at 1 MHz.)	8
3.1	Cole-Cole parameters of the breast tissue, tumor, and skin valid from 0.5 GHz to 20 GHz	34
4.1	Estimated Debye parameters valid from 3.1 GHz to 10.6 GHz	48
5.1	Cole-Cole parameters of the six types of tissue in the order of decreasing adipose content valid from 0.5 GHz to 20 GHz	62
5.2	Acoustic and thermal properties of the breast tissue, tumor, and skin (f is in MHz.)	64
5.3	Distance between the image peak and the centre of the inclusion in the radar images	78
5.4	Distance between the image peak and the centre of the inclusion in the thermoacoustic images	78

List of Abbreviations and Acronyms

When a specialized terminology is introduced in a thesis chapter for the first time, its name is given in its entirety followed by its abbreviation or acronym in brackets. Thereafter, only the abbreviation or acronym describing the concept is used in the rest of the chapter.

Abbreviation or acronym	Meaning
CART	Classification and regression tree
DAS	Delay-and-sum
FDB	Frequency-domain beamforming
FDTD	Finite-difference time-domain
SAR	Specific absorption rate
SCR	Signal-to-clutter ratio

List of Notation

The symbols used throughout this thesis are selected to conform as closely as possible to the *IEEE Standard Letter Symbols for Quantities Used in Electrical Science and Electrical Engineering* [58]. These symbols are defined in the chapters in which they appear. However, it is impossible to have unique symbols defined for all quantities in the thesis. Some different quantities share the same symbol, which is expected to have a clear interpretation based on the context.

Greek-Based Notation

Greek symbol	Meaning
α	Correction factor in the Cole-Cole model, complexity penalty, volume expansion coefficient
α_a	Acoustic conductivity
β	Linear attenuation coefficient of X-ray, microwave, and acoustic wave
$\Delta\epsilon$	Difference between the infinite and static relative permittivity
δ	Dirac delta function
ϵ	Absolute permittivity
ϵ_o	Absolute permittivity in vacuum
ϵ_r^*	Complex relative permittivity
ϵ_r	Real part of the complex relative permittivity
ϵ_∞	Relative permittivity for the infinite value of frequency
η	Intrinsic impedance
η_o	Intrinsic impedance in vacuum
θ	Spherical inclination angle
κ	Thermal conductivity

μ	Absolute permeability
μ_o	Absolute permeability in vacuum
σ_e	Effective electric conductivity
σ_s	Static electric conductivity
ρ	Density
τ	Relaxation time constant in the Cole-Cole and Debye model, time delay
Φ^e, Φ^m	Scalar field quantity
Φ	Scalar field quantity, acoustic velocity potential
ϕ	Spherical azimuth angle
ω	Angular frequency
Ω	Spatial domain of integration

Roman-Based Notation

Roman symbol	Meaning
\vec{A}	Magnetic vector potential
A	Solution to the spherical Bessel equation
A_r	Radial component of the magnetic vector potential
A_θ	Elevation component of the magnetic vector potential
A_ϕ	Azimuth component of the magnetic vector potential
\vec{a}_x	Unit vector in the x direction
\vec{a}_y	Unit vector in the y direction
\vec{a}_z	Unit vector in the z direction
\vec{a}_r	Unit vector in the radial direction
\vec{a}_θ	Unit vector in the elevation direction
\vec{a}_ϕ	Unit vector in the azimuth direction
a_n	Some scalar coefficient
\vec{B}	Magnetic flux density
\hat{B}_n	n^{th} -order Riccati-Bessel function
B	Solution to the associated Legendre equation
b_n	n^{th} -order spherical Bessel function, some scalar coefficient
C	Solution to the Harmonic equation

c_a	Acoustic speed
c_n	Some scalar coefficient
c_{nm}	Some scalar coefficient
c_p	Specific heat capacity
c_o	Light speed in vacuum
d	Diameter of a cylinder, distance of propagation
d_n	Some scalar coefficient
\vec{D}	Electric flux density
\vec{E}	Electric field intensity
E_x	x component of the electric field intensity
E_y	y component of the electric field intensity
E_z	z component of the electric field intensity
E_r	Radial component of the electric field intensity
E_θ	Elevation component of the electric field intensity
E_ϕ	Azimuth component of the electric field intensity
\vec{F}	Electric vector potential
F_r	Radial component of the electric vector potential
F_θ	Elevation component of the electric vector potential
F_ϕ	Azimuth component of the electric vector potential
$\mathcal{F}(\cdot)$	Fourier transform
$\hat{f}(i)$	Average voxel intensity of the leaf node that contains the i^{th} voxel
f	Dummy function
G	Fourier transform of g
g	Scalar function of time, Green's function
\vec{H}	Magnetic field intensity
$\hat{H}_n^{(1)}, \hat{H}_n^{(2)}$	n^{th} -order Riccati-Hankel function of the first and second kind
H_x	x component of the magnetic field intensity
H_y	y component of the magnetic field intensity
H_z	z component of the magnetic field intensity
$h_n^{(1)}, h_n^{(2)}$	n^{th} -order spherical Hankel function of the first and second kind
I	Envelope of the instantaneous power
i	Integer index
\vec{J}	Current density

\vec{J}_p	Polarization current density
\hat{J}_n	n^{th} -order Riccati-Bessel function of the first kind
$J_{i,x}$	x component of the impressed current density
$J_{p,x}$	x component of the polarization current density
$J_{p,y}$	y component of the polarization current density
$J_{p,z}$	z component of the polarization current density
j	$\sqrt{-1}$
j_n	n^{th} -order spherical Bessel function of the first kind
K	Bulk modulus
k	Wave number
\hat{L}	Empirical risk
\mathcal{L}	Linear operator
L	Number of layers of a multi-layer sphere
P_n^m	Associated Legendre polynomial of degree n and order m
P_n	Ordinary Legendre polynomial of degree n
M	Number of measurements
N	Number of elements in an ordered set
N_{\max}	Highest order in the summation of a series
N_{stop}	Some integer quantity
n	Some integer quantity
m	Some integer quantity
p	Partition index of an ordered set, pressure
\vec{r}	A vector in a three-dimensional space
r	Radial distance
S	Time and space-dependent specific absorption rate
\tilde{S}	Space-dependent specific absorption rate
S_o	Spectrum of X-ray radiation
\tilde{s}	Radar signal after calibration
T	Regression tree, temperature
t_d	Temporal delay
Δt	Temporal increment
\vec{u}	Particle velocity in a fluid
u_x	x component of the particle velocity

u_y	y component of the particle velocity
u_z	z component of the particle velocity
w	Weight in an imaging algorithm
x	Some scalar quantity, axis of a Cartesian coordinate system
Δx	Spatial increment in the x direction
y	Axis of a Cartesian coordinate system
Δy	Spatial increment in the y direction
z	Axis of a Cartesian coordinate system
Δz	Spatial increment in the z direction

Miscellaneous Non-Standard Notation

Miscellaneous symbol	Meaning
$(\cdot)^{inc}, (\cdot)^{refl}$	Incident, reflected
$(\cdot)^{meas}, (\cdot)^{calc}$	Measured, calculated
$(\cdot)^{tissue}, (\cdot)^{background}$	Tissue region, background region
$MSE(\cdot)$	Mean-squared error
$\Im(\cdot)$	Imaginary part of a complex number
$\Re(\cdot)$	Real part of a complex number
$(\cdot)^{(l)}$	Quantity associated with the l^{th} layer of a multi-layer sphere

Chapter 1

Introduction

Among Canadian women, breast cancer is the second leading cause of cancer mortality, following lung cancer. It was expected that 22,700 new breast cancer cases would be diagnosed in 2009, and the death rate was estimated to be 23.8%, about 5,400 cases [16].

The glandular tissue in a woman's breast produces milk. The adipose tissue and fibrous connective tissue support the gland. Fig. 1.1 shows the anatomic structure of a woman's breast. Breast cancer commonly starts with some cancer cells residing in the milk ducts or glands. These cells aggregate to form a lump or a mass called a tumor. Some tumors are confined within the milk ducts or glands, while others break through the confinement spreading to surrounding tissues, often with rapid, uncontrolled metastatic growth.

Microwave imaging techniques have been actively studied in the past 15 years. Research has shown that the alteration in vascularity, cellularity, and stromal characteristics in breast malignancy are uniquely related to the changes in the dielectric properties [113]. Microwave imaging techniques exploit the contrast in the dielectric properties between malignant and healthy tissue and generate images of the breast. Microwave equipments can be potentially designed economically affordable and optimized for breast imaging. They hold the promise to become non-ionizing, non-invasive, and cost-effective tools to complement existing imaging techniques, especially at the screening stage of a medical examination for breast cancer.

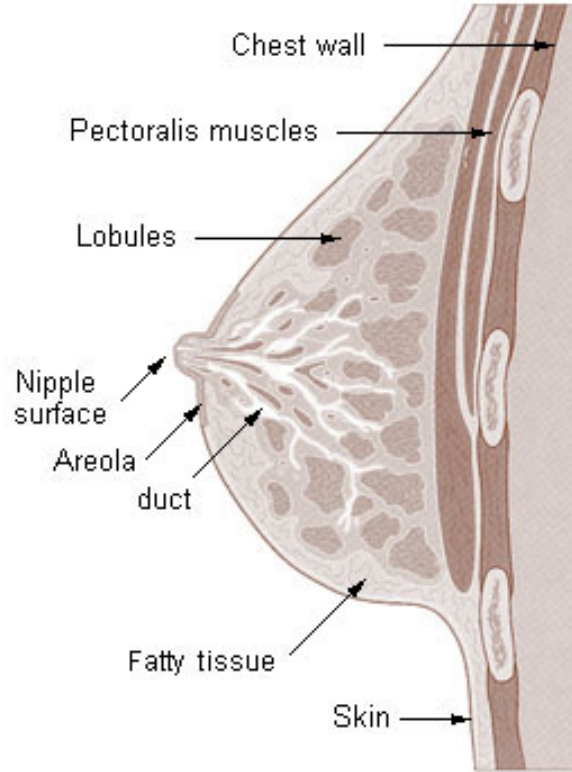


Fig. 1.1 Drawing of the cross section of a human breast. The adipose tissue, glandular tissue (lobules), ducts are labelled. The fibrous connective tissue connects the gland and adipose tissue (not shown). The picture is adopted from [105].

1.1 Research Objectives

The scope of this thesis falls in the research area of microwave imaging techniques. One microwave imaging technique is called microwave radar, which radiates wideband pulses to a breast and identifies the locations of the internal scatterers based on the scattered microwave energy. Due to the wide bandwidth of the pulses, this technique has shown the potential to detect sub-centimetre tumors. The recent characterization of the dielectric properties of breast tissue, categorized based on the adipose content, has shown less possible contrast between malignant and healthy tissue [84, 86], compared to previously published results. The first objective of this thesis is to investigate how the reduced contrast could affect the design space of microwave radar systems.

Because of the continuing growth in the computing power of dedicated hardware, full-

wave electromagnetic simulations of electrically large objects such as human breasts have become plausible. The second objective of the thesis is to build numerical breast models that are realistic in dielectric properties and can be integrated with antennas or antenna arrays for electromagnetic simulations.

When a high-power microwave pulse is radiated to a breast, its electromagnetic energy is selectively absorbed by the tissue associated with higher conductivity and converted to heat. This leads to thermoelastic expansion of the tissue and generation of acoustic waves. This physical phenomenon is known as the microwave-induced thermoacoustics. The acoustic signals, propagating to the breast surface, can be collected and used to identify the regions of microwave absorption. Previous studies have shown sub-centimetre resolutions achieved by the microwave radar and microwave-induced thermoacoustic technique. The third objective of this thesis is to verify their imaging capability with the aim to combine the signals to enhance the probability of detection.

Finally, the microwave-induced thermoacoustic and microwave tomographic systems can operate in the frequency range from 300 MHz to 1200 MHz. The fourth objective of the thesis is to assess the possibility of combining these two systems.

1.2 Thesis Contributions

With the aforementioned objectives, this thesis claims the following original contributions:

- We used the solution of a plane wave scattered by a multi-layered sphere and the recent dielectric measurements of the breast tissue to model the scattering of a tumor embedded in a breast. The analytical solution allowed us to estimate the bandwidth and strength of the reflected signals from the tumor. These results identify the requirements on microwave radar systems.
- The challenge associated with building numerical breast models is to capture the heterogeneity of the tissue and to support a grid setting compatible with antennas. We applied the classification and regression tree analysis to the breast tissue. The approximation averaged out the inherent noise in the magnetic resonance images and provided a way to determine the amount of heterogeneity in the tissue by the use of a complexity penalty. The breast models and antennas can be imported to commercial

finite-difference time-domain based software, which automatically generates the grid compatible for the models and antennas for full-wave electromagnetic simulations.

- We simulated the microwave radar and microwave-induced thermoacoustic process and generated images from the simulated signals. We found that both techniques could image dielectric inclusions in a homogeneous medium. The microwave-induced thermoacoustic technique yielded promising results when imaging a heterogeneous breast model, while the microwave radar technique suffered from the tissue heterogeneity and dispersion. This study is in support of the utility of the microwave-induced thermoacoustic technique and warrants further investigation of the technique.
- We conceived a system that could provide a non-uniform mesh from the thermoacoustic signals. This non-uniform mesh could potentially help solve the inverse-scattering problem in microwave tomography, which recovers the spatial permittivity and conductivity. However, we found that it is not feasible to construct a single system, that simultaneously creates a uniform electromagnetic field in the tissue needed in microwave-induced thermoacoustics, and provides sufficient number of antennas to collect signals for solving the inverse-scattering problem in microwave tomography.

1.3 Thesis Outline

Chapter 2 of this thesis presents a review of the physical principles of common breast imaging techniques. Then, microwave imaging techniques and their variants are discussed in the context of the current literature. Chapters 3, 4, 5, and 6 present the algorithms, simulations, and results associated with each contribution of the thesis. In particular, Chapter 3 determines the power resolution and bandwidth requirement on a viable microwave radar system. Chapter 4 presents the process of building numerical breast models. Chapter 5 presents the comparison of the microwave radar and microwave-induced thermoacoustic technique. Chapter 6 presents the conceived system, the inverse-scattering algorithm, and the engineering considerations on the practicality of the system. Finally, Chapter 7 summarizes the thesis contributions and discusses the direction of further research as an extrapolation of the current state of the art in microwave breast imaging techniques.

Chapter 2

Imaging Techniques for Breast Cancer

A typical medical examination for breast cancer involves three stages: screening, diagnosis, and categorization. Each stage has particular requirements on the capability of imaging techniques. The imaging techniques used at the screening stage must have high sensitivity, which is a measure of how often the imaging result correctly identifies a woman as having breast cancer. The techniques used at the diagnosis stage must have high specificity, which is a measure of how often the imaging result correctly identifies a woman as not having breast cancer. The techniques used at the categorization stage must identify the nature of the malignancy according to its size and spread.

X-ray mammography, magnetic resonance imaging, and ultrasound imaging are popular medical imaging techniques. They find applications in imaging various body parts for different medical purposes. In Section 2.1, 2.2, and 2.3, we restrict our discussion of these techniques to imaging the human breasts primarily for the screening purpose. Their physical principle, contrast due tissue properties, and medical advantages and disadvantages are briefly discussed. In Section 2.4, we review the measurements results of the dielectric properties of breast tissues at microwave frequencies. The contrast in the dielectric properties between malignant and healthy tissue promises the use of microwave imaging for breast cancer. In Section 2.5, we categorize the available microwave imaging techniques, and review the current state of development and research.

2.1 X-ray Mammography

X-ray is a form of electromagnetic radiation associated with a wavelength in the range from 0.01 nm to 10 nm. The diffraction of X-ray, as it propagates through breast tissue is negligible. This nature of X-ray is the reason behind the good spatial resolution in X-ray mammograms.

When a woman is mammogrammed for breast cancer, she is in a standing position placing her breast on a platform. A plate descends from above to gently compress the breast against the platform. The projector hanging above the plate radiates low-dose X-ray towards the breast. The attenuated X-ray exposes the film embedded in the platform, leaving a projected image of the breast. The value of a pixel on a mammogram represents the intensity of X-ray arriving at the film. In a homogeneous medium, the X-ray experience exponential attenuation, described as

$$S_o e^{-\beta x}$$

where S_o denotes the spectrum of the incident X-ray and β is the linear attenuation coefficient, which is an endogenous property of the medium. The difference in the linear attenuation coefficients of malignant and healthy tissue determines the contrast of X-ray mammograms. Fig. 2.1 shows the linear attenuation coefficients of bone, skeletal muscle, average breast tissue, and adipose in the typical range of the photon energy used in X-ray mammography [64, 56]. X-ray is attenuated in the calcium-rich bone more than in breast tissue, muscle and blood. Since micro-calcification is one of the prominent signs to indicate the early development of breast tumors, X-ray mammography can detect breast tumors at an early stage. Another advantage of X-ray mammography is its cost effectiveness that allows widespread deployment as a screening tool. The good spatial resolution, high contrast due to micro-calcification, and cost-effectiveness establish X-ray mammography as the only screening technique for breast cancer approved by the Food and Drug Administration of the United States.

Another structure that could mark the presence of breast cancer is malignant lesion in soft tissue. The lesion leaves a faint spot in the mammogram due to a lack of contrast in the X-ray attenuation in soft tissue. This contributes to the false-negative rate in X-ray mammography. Also, breasts of young women with dense tissue are more difficult

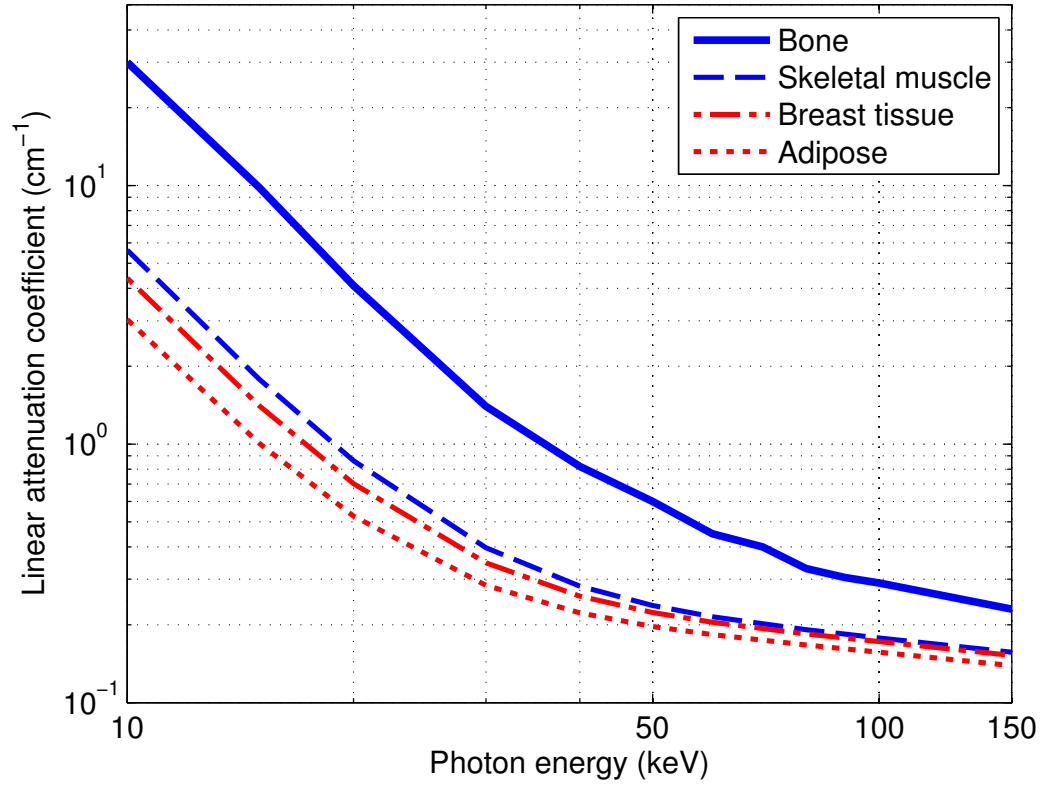


Fig. 2.1 X-ray attenuation as it passes through bone, skeletal muscle, average breast tissue, and adipose.

to compress. This increases the superposition of lesion with dense glandular tissue and results in reduced image contrast and higher false-positive and false-negative rates [62]. And finally, there is a health concern over the exposure to ionized radiation when women are recommended to have regular X-ray checkups.

2.2 Magnetic Resonance Imaging

When nuclei are placed in a strong magnetic field, the axis of self spin of their protons align with the direction of the externally applied field. An electromagnetic wave at a particular frequency in the megahertz range causes the axis of spin to tilt away from the alignment. As the protons try to re-align themselves, electromagnetic signals are emitted, which can be detected by coils and used to generate images. This is the principle of magnetic resonance imaging.

Table 2.1 Acoustic properties of the breast tissue, tumor, body adipose, and water (The attenuation coefficient is evaluated at 1 MHz.)

	Speed m/s	Density kg/m ³	Attenuation dB/cm
Breast tissue	1450-1570	990-1060	0.75
Breast tumor	1437-1547	1182	0.75
Adipose	1450	950	0.29
Water	1480	1000	0.0022

The pixel intensity of a magnetic resonance image is directly related to the proton density and how quickly the protons return to the equilibrium state, which is characterized by the T1 and T2 relaxation time [54, ch. 23]. It is known that factors such as the presence of chemical compounds, paramagnetic ions, and the flow rate of liquids affect the proton density and the relaxation time. Magnetic resonance imaging is not sensitive to micro-calcification, which is occasionally seen in the images as tiny signal voids.¹ Thus, magnetic resonance imaging can be complementary to X-ray mammography as a screening tool [57].

The limiting factor associated with using magnetic resonance imaging as a screening tool is the monetary cost of the hardware and the time elapse of the imaging session, which requires from 30 min to 45 min in contrast to X-ray mammography from 5 min to 10 min. Magnetic resonance imaging equipments are currently limited to hospitals, major clinics, and research facilities.

2.3 Ultrasound Imaging

Ultrasound imaging is a technique based on the propagation of sound wave in the frequency range from 5 MHz to 15 MHz through human breasts. The patient lies in a supine position (facing up) on the examination table. The doctor holds a transducer array in contact with

¹When screening women with high-familial risk for breast cancer, magnetic resonance imaging provides superior sensitivity (about 71-100%) compared with X-ray mammography (about 33-60%) [81, 82]. However, when using magnetic resonance imaging as a screening tool on women at an average risk of breast cancer, no data is available that would ultimately prove that magnetic resonance imaging would perform better.

the breast skin, and translates it across the surface.² The wavelength at the ultrasound frequencies is in the range from 10 μm to 300 μm , which is small compared with the dimension of breast tumors. This contributes to good spatial resolution in ultrasound images. The amount of reflection, sound speed, and attenuation associated with sound propagation are endogenous properties of breast tissue. Table 2.1 lists the values of these properties of average breast tissue, breast tumor, adipose and water compiled from several sources [96, 31, 24]. It should be noted that the variation of these parameters between the average breast tissue and breast tumor is no more than 10%. This reduces the amount of contrast in ultrasound images. Currently, ultrasound imaging finds its application as a complementary technique to X-ray mammography to determine if certain dark spots in a mammogram are cysts³ or solid tumors.

In summary, X-ray mammography is currently the only imaging technique approved by the Food and Drug Administration for the purpose of screening breast cancer because of its sensitivity to micro-calcification and its overall cost-effectiveness. Magnetic resonance imaging with contrast enhancement provides good sensitivity to malignant lesion in soft tissue, which can complement X-ray mammography to reduce false-negative rate.⁴ However, the cost associated with the equipment and imaging time prevent its use as a screening tool. Ultrasound can complement X-ray mammography to determine if some dark spots are cysts or solid tumors.

Continuing effort has been put forward to enhance these existing imaging techniques and seek low-cost complementary techniques that exploit contrast in other tissue-specific properties. Microwave imaging is one of the candidates, which exploits the contrast in the dielectric properties between malignant and healthy tissue of the breast. We review the literature associated with the dielectric properties of the breast in the next section, followed by a discussion of the microwave techniques developed for breast imaging.

²Another ultrasound breast imaging system currently under development assumes the patient lies in the prone position, with the pendent breast submerged in a warm water bath. A circular transducer array is moved in the direction perpendicular to the chest wall [32].

³Fluid-filled sac.

⁴Gadolinium-based contrast agents can shorten the T1 relaxation time, which leads to an increase of the signal intensity.

2.4 Dielectric Properties of the Human Breast

Breast tissue is highly dispersive in the microwave range, i.e. the wave number is not a linear function of frequency. Early measurements of the permittivity and conductivity performed on excised breast samples in the frequency range from 50 MHz to 3.2 GHz have shown a significant contrast between malignant and healthy tissue of the human breast, 4:1 in conductivity and 5:1 in permittivity [17, 129, 15, 66]. The characterization of the dielectric properties of breast tissue was conducted at the University of Calgary and University of Wisconsin in 2007 [84, 86]. Tissue samples were obtained from 93 breast reduction surgeries and 488 measurements were taken consistently, each in the frequency range from 500 MHz to 20 GHz. The samples were mixtures of adipose, gland and connective tissue. Precise measurements of their dielectric properties based on this categorization were not possible. In their work, the samples were categorized into three groups based on the percentage of adipose content in the samples. The measurements were interpolated by the Cole-Cole model to cover the continuous spectrum from 500 MHz to 20 GHz [85]. There are two important findings associated with the measurements: (a) the contrast in permittivity and conductivity between the malignant tissue and the adipose-dominant tissue is high and is consistent with the previously published results; (b) the contrast between the malignant tissue and the gland-dominant tissue is no more than 10%. The authors offered a possible explanation as to why a high contrast between malignant and healthy tissue was reported in previous measurements [84]

... to characterize the dielectric properties of normal tissue in such specimens, it would have been necessary to characterize a region of tissue away from the tumor. Since breast cancer arises in glandular tissues, a site distinct from the tumor would likely have higher adipose content, leading to the lower and more homogeneous dielectric properties values reported in several of the earlier studies.

Given the fact that tumors are likely to grow within glandular tissue, the second finding of this study, if true, would fundamentally limit the capability of microwave imaging techniques.

2.5 Microwave Imaging Techniques for Breast Cancer

Microwave techniques are applicable to image human breasts as there exists a contrast in the dielectric properties between malignant and healthy tissue. Two other factors to support microwave breast imaging are: (a) microwave signals attenuate significantly less (about 4 dB/cm) in healthy tissue due to the presence of adipose than in other organs which contain much water; (b) breasts naturally protrude outside the human body and are easily accessible by antennas. Four major microwave imaging techniques have been identified in the literature. They are microwave radar imaging, microwave tomographic imaging, microwave-induced thermoacoustic imaging, and microwave-elastic imaging. Their operation modes, imaging algorithms, and major advancement in the research are discussed in the following sections.

2.5.1 Microwave Radar Imaging

In microwave radar imaging, antennas radiate low-power microwave pulses towards a breast and receive the reflection to identify the locations of microwave scatterers. Initially, the system was conceived in the following way. A patient lay in the supine position (facing up) and wideband antennas were placed in direct contact with the naturally flattened breast to radiate and receive microwave pulses [47, 48]. This conformal design has a good coverage of the breast and the region between the armpit and the breast, where breast cancer also occurs [110]. However, when antennas are placed directly on the skin, their radiation characteristics are easily affected by the condition of the contact. This degrades the robustness of the system.

A cylindrical design, proposed at a similar time as the conformal design, required a patient to lie in the prone position (facing down) [39]. The pendent breast through the cavity of the bed was surrounded by either a mechanically steered antenna or an antenna array. The breast and the antennas were immersed in some matching liquid. This cylindrical design has a limited coverage of the region between the armpit and the breast.

A third design was recently proposed involving the use of highly directive antennas, such as the balanced antipodal Vivaldi antenna [12] and the transverse electromagnetic horn antenna [4]. Both antennas consist of dielectric parts with a high permittivity to increase the directivity. These antennas are in direct contact with the breast skin and are manually moved on the breast, similar to the use of transducers in ultrasound breast

imaging.

Many microwave radar systems have followed the cylindrical design or the closely related radon design, which uses a solid matching medium and a fixed antenna array [27, 72, 74]. This preference is perhaps due to the robustness of the design and the availability of imaging algorithms for this scanning geometry.

The most important requirement on antennas for microwave radar imaging is that the majority of the energy of the microwave pulse should be radiated towards the breast and little should be reflected. Otherwise, the reflection from antennas may overlap in time with the reflection from tumors and degrade the signal-to-noise ratio. Another requirement on antennas is signal fidelity, which is a measure of how well the shape of the input signal is preserved in the radiated field.⁵ A good fidelity suggests that a radiating field has been established, and the breast should be placed beyond this distance to avoid coupling with the antennas. The third requirement is radiation efficiency, which is defined as the ratio between the radiated energy and the energy loss in antennas.

A bow-tie antenna with resistive loading was introduced, whose time-domain reflection from the tip of the antenna is -106 dB below the exciting pulse [46]. The reflection requirement on antennas can also be described in the frequency domain, which is to have a reflection coefficient less than -10 dB in the approximate range from 1 GHz to 10 GHz.⁶ Several antennas have been proposed for the cylindrical design in the literature. Briefly, the pyramid horn antenna is suitable for a scanning system [90]. The travelling wave antenna [67] and the stacked-patch antenna [72, 43] offer a low profile, less than 3 cm in their maximum dimension. They can be arranged in a cylindrical array for multi-static measurements.

The use of a matching medium reduces the energy reflected from the skin and increases the energy delivered to the tissue. The dielectric properties of an ideal medium are dependent on both the dielectric properties of the skin and the tissue. They are also dependent on the thickness of the skin and have to match in a wide microwave range [1, 117]. Sill did a numerical study on the effect of three immersion media with a relative permittivity of 2.5, 9 and 36. He observed that a higher permittivity decreases the antenna beam width, which limits the effectiveness of the clutter suppression in the imaging algorithms. He suggested

⁵The temporal shape of the radiated field is the time-derivative of the input current [3, 133].

⁶The frequency-domain requirement is commonly adopted in the literature perhaps due to the frequency-domain definition of ultra-wideband systems adopted by the Federal Communications Commission, who authorizes the unlicensed use in the range from 3.1 GHz to 10.6 GHz.

the use of a medium with a low relative permittivity of 2.5, which can be found among oil-like materials.

On the signal processing part, one requirement associated with the cylindrical design is to know the time-delay between the antennas and the breast surface. This can be estimated between the peak of the incident pulse and the peak of the reflected pulse [87, 135, 136]. Another interesting approach to this problem is to use a laser distance measuring device to identify the breast surface with sub-millimetre precision before the microwave imaging of the breast [14, 134]. Another requirement associated with the microwave radar imaging is to remove the early reflection from the medium-skin interface, which is several degrees of order higher than the reflection from a tumor. Several methods were proposed based on the assumption that all antennas see similar reflection at the medium-skin interface [89, 10, 127]. They take the average of the weighted-sum of all received signals and subtract this average from the received signals to remove the medium-skin reflection.

The aim of microwave radar imaging is to generate an image of the scattered energy as a function of the two-dimensional space. The challenge presented to the imaging algorithms is microwave dispersion and tissue heterogeneity. Microwave dispersion causes the temporal widening of the pulse as it propagates through tissue, which reduces the spatial resolution. The tissue heterogeneity may cause multiple reflections and contaminate the signals reflected from tumors.

The earliest imaging algorithm applied to breast imaging is the delay-and-sum algorithm [89]. This is followed by the time-domain and frequency-domain beamforming algorithm, which uses a spatial filter to compensate microwave dispersion experienced by the received signals [10, 26] before summing. The robust capon beamforming algorithm permits additional adjustment of the array steering vector to compensate for delay and dispersion [139]. And the delay-multiply-and-sum algorithm is a version of the delay-and-sum algorithm that artificially increases the number of input signals by performing coupled cross-multiplication of the received signals [91]. The imaging algorithm based on the general-likelihood-ratio test takes a different approach, from which the test statistics representing the matching between the received signals and the expected signal templates are presented as a function of the two-dimensional space [27]. These imaging algorithms are capable of presenting images in which 2- to 10-mm tumors are visible. However, to the best of our knowledge, there has not been any comprehensive study on these imaging algorithms when applied to the numerical breast models based on the new dielectric measurements.

Independent laboratory experiments on breast models have been conducted to demonstrate the validity of microwave radar imaging [38, 88, 127, 121, 83, 74]. More noticeable clinical results on patients, when using a system consisting of 32 antennas, have been reported from the University of Bristol [71, 25, 73, 70], in which millimetre scatterers can be detected. However, the locations of the scatterers did not correlate well with the actual locations of tumors, and the images were contaminated by clutters. These preliminary results suggest that the microwave radar images would not be clutter free due to microwave dispersion and tissue heterogeneity. Trained professionals who understand the advantages and limitations of microwave radar imaging are needed to properly interpret the images.

2.5.2 Microwave Tomographic Imaging

Microwave tomographic systems⁷ operate similarly as the cylindrical design of microwave radar systems. The pendent breast is surrounded by antennas through a hole in the bed, both of which are immersed in some matching medium. The antennas radiate microwave signals towards the breast and receive the scattered signals.

Microwave tomographic systems generate images of permittivity and conductivity in the breast region from the scattered signals. As the permittivity and conductivity are functions of frequencies, several images of these two quantities at discrete frequencies in the operating range of the antennas are usually presented.

Antennas in microwave tomographic systems for breast imaging operate in the range from 300 MHz to 1.2 GHz. Higher frequencies lead to better spatial resolution, but at the price of increasing attenuation. Monopole antennas are sufficient and commonly used [98, 119]. Glycerin and saline water mixture at different percentage provides a good range of permittivity and conductivity for matching the average dielectric properties of the tissue in the aforementioned frequency range [100, 11].

The problem of generating images of permittivity and conductivity of the breast is known as an inverse-scattering problem. One way to solve this problem is by noticing that the field observed at the antennas can be expressed as a volume integral of the total field inside the breast, in which the effect of multiple reflections is neglected [19, 92]. The

⁷The word “tomography” means “something of a slice”. Many microwave imaging systems produce two-dimensional images. However, it is observed in the literature that microwave tomographic systems commonly refer to those that recover the conductivity and permittivity distribution of the breast. We follow this convention in the literature here and differentiate them from other microwave imaging systems.

Born approximation replaces the actual total field by the one calculated from the forward solver. This volume integral equation can be discretized in space and lead to a linear system involving the measured field and the field calculated from the forward solver. Solving this linear system gives a new estimate on the change of the permittivity and conductivity, which can be fed back to the forward solver to calculate a new estimate for the next iteration. The iteration stops when some error between the measured field and the calculated field converges. The Born approximation works well in the scenarios, in which the internal multiple reflection is weak.

An alternative way to solve the inverse-scattering problem is to formulate it as a least-square optimization problem and solve it through some gradient-based method. The cost functional can be defined as

$$\sum_{i=0}^{M-1} \|\vec{E}_i^{meas} - \vec{E}_i^{calc}\|_2, \quad (2.1)$$

where \vec{E}^{meas} and \vec{E}^{calc} are the measured and calculated time-harmonic field. M is the number of measurements, and $\|\cdot\|_2$ denotes the Euclidean norm. This problem can be solved by the family of the gradient-based iterative methods such as the gradient descent method, the Newton-Raphson method, the Gauss-Newton method, and the Levenberg-Marquadt method. Another suggested functional is to use the logarithm of the amplitude and the un-wrapped phase of the relative change in the signal level, which is defined as

$$\sum_{i=0}^{M-1} \left\| \log(|\vec{E}_i^{meas}|) - \log(|\vec{E}_i^{calc}|) \right\|_2 + \left\| \angle(\vec{E}_i^{meas}) - \angle(\vec{E}_i^{calc}) \right\|_2. \quad (2.2)$$

It has been found that minimizing this cost functional improves the imaging results [102, 104, 119].

Another improvement in the imaging algorithm is to use a different mesh to interpolate the dielectric properties from the mesh used in the forward solver. This is based on the assumption that the permittivity and conductivity are smooth functions of space and do not vary rapidly. This reduces the parameter space to search for an optimal solution [36] that satisfies (2.1) or (2.2).

Independent laboratory experiments have been conducted to demonstrate the principle of microwave tomographic imaging [99, 111, 22, 146]. It was shown that a 14-mm inclusion could be resolved with 16 antennas at 1 GHz with a 2:1 contrast in the dielectric properties

between the inclusion and background [22]. Another study showed that two 5-mm dielectric spheres could be resolved with 105 measurements at 1.74 GHz with a 15:1 contrast in permittivity [146].

More noticeable clinical results on patients have been reported by the researchers from the Dartmouth College [111, 99, 37], who built a system with 32 monopole antennas operating in the frequency range from 300 MHz to 900 MHz. The radiated power was below 5 mW. It is shown that the non-linearity caused by microwave diffraction was the key limiting factor in the spatial resolution of breast images. Imaging small breast tumors (<5 mm) at a low contrast became difficult. This suggests that microwave tomographic imaging may not be an effective tool for the screening purpose. However, as conductivity is sensitive with the variation of temperature, it has been considered as a tool to monitor the temperature during a hyperthermia treatment [101, 103].

2.5.3 Microwave-Induced Thermoacoustic Imaging

When a high-power pulse is radiated towards a breast, a portion of the electromagnetic energy is absorbed by the tissue associated with a higher conductivity and converted to heat. This leads to thermoelastic expansion of the tissue, which generates acoustic waves propagating to the breast surface. These acoustic waves can be collected and used to generate an image of microwave absorption.

The key advantage of the microwave-induced thermoacoustic imaging is that the acoustic signals have smaller wavelengths compared to the dimension of tissue. And the signals travel in one direction from the microwave absorbers to the transducers.⁸ This promises a good spatial resolution in the image.

One requirement on the system is to radiate signals with a high instantaneous power to excite the thermoacoustic process. The low duty cycle keeps the elevation of the temperature (around 0.1 mK [140]) below the safety standard [59]. Unfocused ultrasound transducers made of piezoelectric materials are used. De-ionized water serves as the matching medium, which absorbs little microwave energy and provides acoustic matching between the breast and transducers.

Due to wave physics, imaging algorithms such as the delay-and-sum algorithm and the time-reversal algorithm in microwave radar imaging are equally applicable to thermoacous-

⁸This is in contrast to the two-way travel in ultrasound imaging.

tic signals [40, 144, 138]. In addition, the millimetre-size transducers can be arranged to conform to the shape of the imaged body, which leads to the modification of the imaging algorithms to a planar, cylindrical, or spherical scanning geometry [141, 142].

The most noticeable work in microwave-induced thermoacoustic imaging applied to human breasts was done at the Indiana University [78, 78, 80]. The patient lay in a prone position, and the pendent breast, the waveguides, and the acoustic transducer array were immersed in de-ionized water. The eight waveguides sat beneath the pendent breast and radiated 0.7- μ s pulse-modulated sinusoid at 434 MHz with an instantaneous power of 25 kW. The radiation rate was 215 pulses/s, which gave an average power of 7.5 W. An acoustic transducer array with 128 7 mm \times 8 mm elements mechanically moved around the pendent breast to record thermoacoustic signals. Images of microwave absorption of the healthy breasts and breasts with malignant tissue were presented [79, 80].

Recently, a system combining microwave-induced thermoacoustic and laser-induced thermoacoustic imaging⁹ was introduced [115]. The most noticeable difference is that a plate made of the plexiglass was placed between the waveguide and the pendent breast. The plate compressed the breast towards the chest wall, which was flattened and had its axial dimension reduced. As the waveguide radiated a high-power pulse-modulated sinusoid at 3 GHz, a uniform electromagnetic field was created in the tissue, which would not be possible without the compression. This mechanical compression transfers the three-dimensional location information of the breast tissue onto two-dimensional images.¹⁰

2.5.4 Microwave Elastic Imaging

The microwave elastic imaging is a new entry among the imaging techniques, which has been studied through numerical simulations. It exploits the contrast in the elastic properties of malignant and healthy tissue [122, 123].¹¹ It is reviewed here for its kinship with other microwave imaging techniques.

The system is conceived to send a microwave sinusoid through the pendent breast, which is mechanically compressed at a constant rate [149]. Because the malignant tissue is

⁹Also known as the photoacoustic imaging or optoacoustic imaging. It is analogous to of microwave-induced thermoacoustics, as the excitation is shifted to the invisible and visible light frequencies. The system exploits the contrast in optical absorption.

¹⁰A clinical study of a system using the near-infrared frequency band to excite the thermoacoustic process is reported in [93], which also needs some compression of the breast for a uniform field.

¹¹This contrast is also the physical principle of palpation in breast cancer detection.

stiffer than healthy adipose and fibro-glandular tissue, the tissue deformation modulates the microwave sinusoid, which is received by antennas. It is shown that the Doppler component of the modulated microwave sinusoid is an increasing function of the level of strain applied to the tissue. And the amplitude of the Doppler component due to the deformation of the malignant tissue can be 10 dB above the amplitude due to the healthy tissue. The disadvantage associated with this design is that the location of the tumor is shifted under compression, which is expected to incur localization error in the images. An alternative design is to use a focused transducer to spatial-selectively apply strain to the tissue. This would isolate the deformation within the focus of the transducer. The disadvantage of this design is that it needs mechanical steering of the focused transducer to scan the entire tissue region.

2.6 Summary

Three common medical imaging techniques considered for breast cancer screening have been reviewed. X-ray mammography provides good spatial resolution and good sensitivity to micro-calcification. It has been widely accepted as a cost-effective screening tool for breast cancer. Magnetic resonance imaging is sensitive to malignant lesion in soft tissue, which complements X-ray mammography. However, the associated cost prevents it from being widely used. Ultrasound imaging finds its application in identifying solid tumors from cysts.

Four microwave imaging techniques have been reviewed in this chapter. They are microwave radar imaging, microwave tomographic imaging, microwave-induced thermoacoustic imaging, and microwave elastic imaging. Chapter 3 and Chapter 4 extend the work in microwave radar, in which we estimate the requirement on microwave radar systems and present a method to build numerical breast models. Chapter 5 presents a detailed comparison on the imaging capability of microwave radar and microwave-induced thermoacoustics. And finally, Chapter 6 evaluates the idea of using microwave-induced thermoacoustics to assist in solving the inverse-scattering problem in microwave tomography.

Chapter 3

Requirements on Microwave Radar Systems

The principle of the microwave radar imaging technique assumes contrast in the permittivity and conductivity between malignant and healthy tissue. The study in [84, 86] has shown that there is a significant dielectric contrast between the malignant and adipose-dominant tissue. However, little dielectric contrast exists between the malignant and mostly glandular tissue.

The study in [33] presented the resonant spectra of tumors calculated from a plane wave scattered by a three-dimensional homogeneous breast model realistic in shape. The conclusions were drawn based on the previously assumed high dielectric contrast and the mono-static radar cross section of the tumor in the frequency range from 1 GHz to 10 GHz. The author concluded that the resonant spectra vary only with the shape and the dielectric properties of tumors and are invariant with the depth of tumor, incident or scattering direction, and incident polarization.

To quickly assess the effect of reduced contrast, we used a multi-layer dielectric sphere to approximate the breast geometry and solve the problem of a plane wave scattered by the multi-layer sphere to estimate the reflected signal. This model did not take into account the hemi-spherical shape of the breast and the heterogeneity of the tissue. And it assumed that a plane wave impinged upon the breast, which deviated from some microwave systems using dipole antennas. However, the calculation associated with this model gave a qualitative description of the strength of the signals reflected by tumors. These results set the

requirements on the microwave radar systems. In addition, the calculation did not require full-wave electromagnetic simulations, which could be potentially time consuming.

This chapter is structured as follows. Section 3.1, introduces the scattering problem of a multi-layer sphere and presents the procedure to solve this boundary value problem. Section 3.2 discusses issues related to the numerical implementation of the solutions in the series forms. Section 3.3 uses this model to calculate the tumor reflected power in the frequency domain, which identifies the needed system power resolution and bandwidth. Section 3.4 concludes this chapter.

3.1 Scattering of a Multi-layer Sphere

3.1.1 Solution Overview

The problem of a plane wave scattered by an L -layer medium is a boundary value problem in solving partial differential equations [21, Ch. 3.7]. Solving such problems includes the following steps:

1. Selecting a coordinate system so that the boundaries between layers conform to some of the principal axes of the coordinate system.
2. Selecting some potentials, which convert the vector Maxwell equations to the scalar Helmholtz equation.
3. Solving the Helmholtz equation using the method of separation of variables, which decomposes it into three linear ordinary differential equations.
4. Applying the homogeneous boundary condition to solve for the eigen functions of the ordinary differential equations.
5. Expressing the incident plane wave in terms of potentials, which are in series forms of the products of the eigen functions.
6. Expressing the scattered potentials and the potentials inside each layer in the series forms with some unknown coefficients.
7. Applying the conditions at the boundaries between layers, which leads to a system of linear equations.

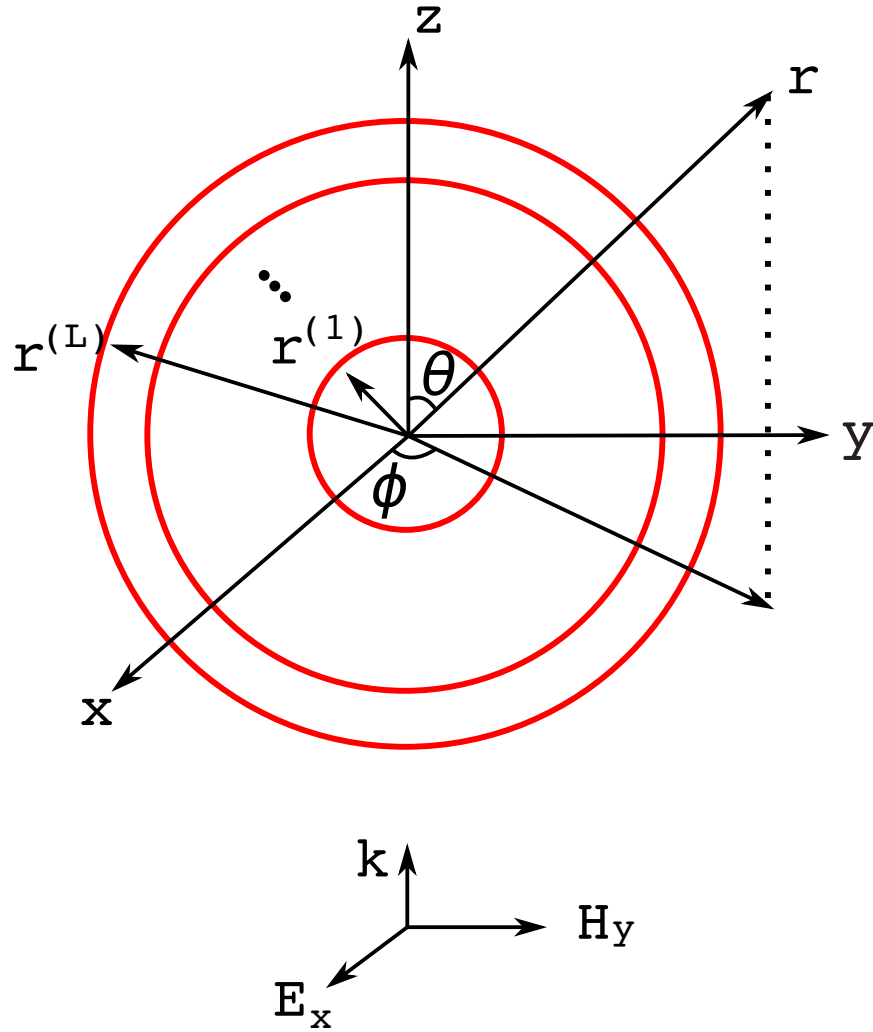


Fig. 3.1 An x -polarized plane wave, propagating in the z direction, impinges upon an L -layer sphere. Starting from the inner core, each layer is characterized by its radius, permittivity, and permeability.

8. Solving this linear system gives the coefficients of the potentials.
9. Expressing the fields in terms of the potentials.

3.1.2 Potentials and Construction of Solutions

Fig. 3.1 shows a plane wave polarized in the $+x$ direction and propagating in the $+z$ direction. The plane wave is scattered by an L -layer sphere. The centre of the sphere coincides with the origin of the spherical coordinate system.

The purpose of using potentials instead of the electric and magnetic field vectors is that the Maxwell equations expressed in terms of potentials become scalar equations. This reduces the number of unknowns to be calculated.¹ Here, we follow the approach in [52, 129] to our problem, in which the magnetic and electric vector potentials are introduced to the scattering problem of a dielectric sphere. The magnetic vector potential \vec{A} and the electric vector potential \vec{F} are defined so that

$$\begin{aligned}\nabla \times \vec{A} &= \mu \vec{H} , \\ \nabla \times \vec{F} &= -\epsilon \vec{E} ,\end{aligned}$$

where ϵ and μ denote the permittivity and permeability. We assume $e^{j\omega t}$ to be the time-harmonic factor.² The Maxwell equations can be equivalently expressed in terms of the vector potentials as

$$\nabla \times \nabla \times \vec{A} - k^2 \vec{A} = j\omega\mu\epsilon \nabla \Phi^e , \quad (3.1a)$$

$$\nabla \times \nabla \times \vec{F} - k^2 \vec{F} = j\omega\mu\epsilon \nabla \Phi^m , \quad (3.1b)$$

where k is the wave number and $k = \omega\sqrt{\mu\epsilon}$, and ω is the angular frequency. Φ^m and Φ^e are some arbitrary scalar field quantities that will be discussed shortly. The electric and magnetic field can be expressed in terms of the potentials as

$$\vec{E} = -\frac{1}{\epsilon} \nabla \times \vec{F} + \frac{1}{j\omega\mu\epsilon} \nabla \times \nabla \times \vec{A} , \quad (3.2a)$$

$$\vec{H} = \frac{1}{\mu} \nabla \times \vec{A} + \frac{1}{j\omega\mu\epsilon} \nabla \times \nabla \times \vec{F} . \quad (3.2b)$$

A convenient choice of the vector potentials in the scattering problems in a spherical coordinate system is to let $\vec{A} = A_r \vec{a}_r$ and $\vec{F} = F_r \vec{a}_r$. Substituting this choice to (3.1a) leads to

¹The choice of the potentials is not unique as their divergence can be freely defined. The Debye potential is used for scattering problems. The Hertzian potential is often for radiation problems [60, 20].

²Some texts [61, 128] use $e^{-j\omega t}$ as the time-harmonic factor due to the preference to represent a wave propagating in the z direction as e^{jkz} . To cross check solutions based on these two conventions, it should be noted that the field is a physical quantity. The same wave propagating in the $+z$ direction can be expressed as $\Re\{Ae^{jkz}e^{-j\omega t}\}$ or $\Re\{\bar{A}e^{-jkz}e^{j\omega t}\}$, where (\cdot) denotes the conjugate. Thus, the phasors expressed in these two different conventions are conjugate pairs.

$$-\frac{1}{r^2 \sin \theta} \frac{\partial}{\partial \theta} \sin \theta \frac{\partial A_r}{\partial \theta} - \frac{1}{r^2 \sin^2 \theta} \frac{\partial^2 A_r}{\partial \phi^2} - k^2 A_r = -j\omega\mu\epsilon \frac{\partial \Phi^e}{\partial r} , \quad (3.3a)$$

$$\frac{\partial^2 A_r}{\partial r \partial \theta} = -j\omega\mu\epsilon \frac{\partial \Phi^e}{\partial \theta} , \quad (3.3b)$$

$$\frac{\partial^2 A_r}{\partial r \partial \phi} = -j\omega\mu\epsilon \frac{\partial \Phi^e}{\partial \phi} . \quad (3.3c)$$

Because the choice of Φ^e is arbitrary, we set

$$\frac{\partial A_r}{\partial r} = -j\omega\mu\epsilon \Phi^e , \quad (3.4)$$

to satisfy both (3.3b) and (3.3c), and (3.3a) becomes the scalar Helmholtz equation of $\frac{A_r}{r}$, which is discussed in the next section. Eq. (3.2) becomes

$$E_r = \frac{1}{j\omega\mu\epsilon} \left[\frac{\partial^2}{\partial r^2} + k^2 \right] A_r , \quad (3.5a)$$

$$E_\theta = \frac{1}{j\omega\mu\epsilon} \frac{1}{r} \frac{\partial^2}{\partial r \partial \theta} A_r - \frac{1}{\epsilon} \frac{1}{r \sin \theta} \frac{\partial}{\partial \phi} F_r , \quad (3.5b)$$

$$E_\phi = \frac{1}{j\omega\mu\epsilon} \frac{1}{r \sin \theta} \frac{\partial^2}{\partial r \partial \phi} A_r + \frac{1}{\epsilon} \frac{1}{r} \frac{\partial}{\partial \theta} F_r , \quad (3.5c)$$

$$H_r = \frac{1}{j\omega\mu\epsilon} \left[\frac{\partial^2}{\partial r^2} + k^2 \right] F_r , \quad (3.5d)$$

$$H_\theta = \frac{1}{\mu} \frac{1}{r \sin \theta} \frac{\partial}{\partial \phi} A_r + \frac{1}{j\omega\mu\epsilon} \frac{1}{r} \frac{\partial^2}{\partial r \partial \theta} F_r , \quad (3.5e)$$

$$H_\phi = -\frac{1}{\mu} \frac{1}{r} \frac{\partial}{\partial \theta} A_r + \frac{1}{j\omega\mu\epsilon} \frac{1}{r \sin \theta} \frac{\partial^2}{\partial r \partial \phi} F_r . \quad (3.5f)$$

3.1.3 Helmholtz's Equation in a Spherical Coordinate System

The Helmholtz equation of a scalar quantity Φ , in the spherical coordinate system, is

$$\frac{1}{r^2} \frac{\partial}{\partial r} \left(r^2 \frac{\partial \Phi}{\partial r} \right) + \frac{1}{r^2 \sin \theta} \frac{\partial}{\partial \theta} \left(\sin \theta \frac{\partial \Phi}{\partial \theta} \right) + \frac{1}{r^2 \sin^2 \theta} \frac{\partial^2 \Phi}{\partial \phi^2} + k^2 \Phi = 0 . \quad (3.6)$$

It is a linear partial differential equation and is solved by the method of separation of variables. Let $\Phi(r, \theta, \phi) = A(r)B(\theta)C(\phi)$. Substituting it to (3.6), we obtain three linear

ordinary differential equations, which are

$$\frac{d}{dr} \left(r^2 \frac{dA}{dr} \right) + [(kr)^2 - n(n+1)]A = 0 , \quad (3.7a)$$

$$\frac{1}{\sin \theta} \frac{d}{d\theta} \left(\sin \theta \frac{dB}{d\theta} \right) + [n(n+1) - \frac{m^2}{\sin^2 \theta}]B = 0 , \quad (3.7b)$$

$$\frac{d^2 C}{d\phi^2} + m^2 C = 0 , \quad (3.7c)$$

where n and m are non-negative integers and $m \leq n$. The operators associated with these differential equations are of the Sturm-Liouville type [45, ch. 5]; they are self-adjoint operators and their eigen functions are orthogonal to each other. The eigen functions form a complete set; any piecewise smooth function can be represented by a linear combination of these eigen functions.³

If we let $x = kr$, eq. (3.7a) becomes the spherical Bessel equation. Its eigen functions are known as the family of the spherical Bessel functions, denoted as $b_n(x)$. Within this family, the ordinary spherical Bessel function is denoted as $j_n(x)$, representing the standing wave. The spherical Hankel function of the first and second kind are denoted as $h_n^{(1)}(x)$ and $h_n^{(2)}(x)$ representing the inward and outward propagating waves. If we let $x = \cos \theta$, eq. (3.7b) is known as the associated Legendre equation and one of its eigen functions is the associated Legendre polynomial denoted as $P_n^m(x)$. When $m = 0$, we have the ordinary Legendre polynomial denoted as $P_n(x)$. Eq. (3.7c) is known as the Harmonic equation and its eigen functions are $e^{\pm jm\phi}$. Any solution to (3.6) can be expressed as the infinite sum of the product of these eigen functions, expressed as

$$\sum_n \sum_m c_{nm} b_n(x)|_{x=kr} P_n^m(x)|_{x=\cos \theta} e^{\pm jm\phi} ,$$

where c_{nm} denotes some coefficient.

³This explains why so many functions are supported by the wave equation to propagate freely in space.

3.1.4 Wave Transformation

A plane wave polarized in the x direction propagating in the z direction is expressed in terms of the eigen functions in the Cartesian coordinate system,⁴

$$\vec{E}^{inc} = E_x^{inc} \vec{a}_x \quad (3.8a)$$

$$= e^{-jkz} \vec{a}_x, \quad (3.8b)$$

which, expressed in the form of the product of the eigen functions, becomes

$$\vec{E}^{inc} = \sum_{n=0}^{\infty} j^{-n} (2n+1) j_n(x)|_{x=kr} P_n(x)|_{x=\cos\theta} \vec{a}_x \quad (3.9a)$$

$$= E_r \vec{a}_r + E_\theta \vec{a}_\theta + E_\phi \vec{a}_\phi \quad (3.9b)$$

$$= \sum_{n=0}^{\infty} j^{-n} (2n+1) j_n(x)|_{x=kr} P_n(x)|_{x=\cos\theta} (\sin\theta \cos\phi \vec{a}_r + \cos\theta \cos\phi \vec{a}_\theta - \sin\phi \vec{a}_\phi). \quad (3.9c)$$

The conversion from (3.8b) to (3.9a) is known as the wave transformation and (3.9c) is the expression in the spherical coordinate system.

Since the component in the direction of \vec{a}_r in (3.9c) solely depends on A_r shown in (3.5a), substituting the component in the direction of \vec{a}_r in (3.9c) to (3.5a) gives

$$A_r^{inc} = \frac{\cos\phi}{\omega} \sum_{n=1}^{\infty} j^{-n} \frac{2n+1}{n(n+1)} \hat{J}_n(x)|_{x=kr} P_n^1(x)|_{x=\cos\theta}, \quad (3.10)$$

where we define $\hat{B}_n(x) = x b_n(x)$.⁵ Thus, $\hat{J}_n(x) = x j_n(x)$, $\hat{H}_n^{(1)}(x) = x h_n^{(1)}(x)$, and $\hat{H}_n^{(2)}(x) =$

⁴It is easy to show that e^{-jkz} is an eigen function of the Helmholtz equation expressed in the Cartesian coordinate system, which is $\frac{\partial^2 \Phi}{\partial z^2} + k^2 \Phi = 0$.

⁵These functions are called Riccati-Bessel's functions in [148, pp. 283]. However, a different definition of Riccati-Bessel's functions exists in the literature [9,]. They are defined as

$$\begin{aligned} S_n(x) &= x j_n(x), \\ C_n(x) &= -x y_n(x), \\ \xi(x) &= x h_n^{(1)}(x), \\ \zeta(x) &= x h_n^{(2)}(x). \end{aligned}$$

There is a sign difference in the relation to $y_n(x)$.

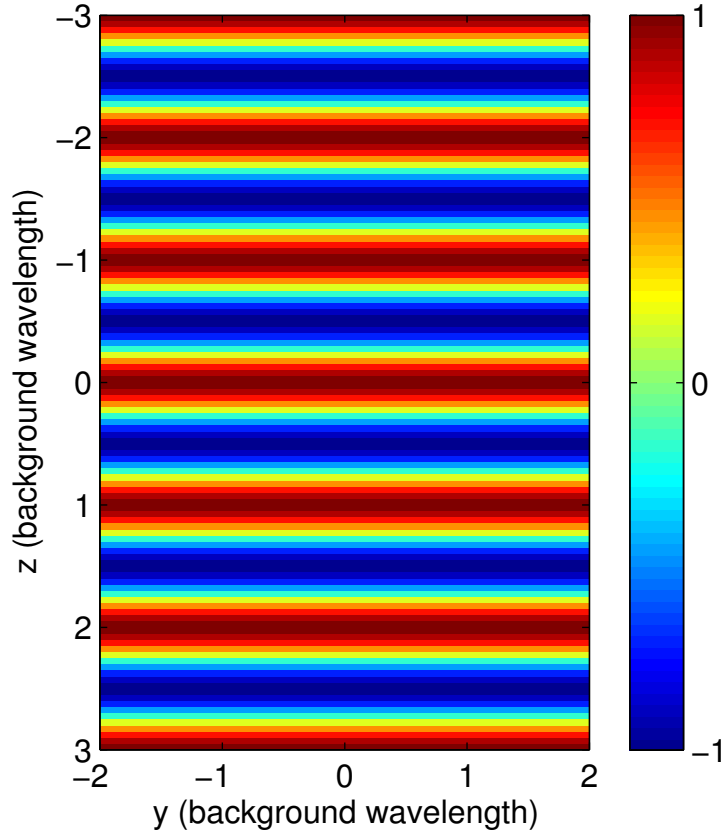


Fig. 3.2 A plane wave propagating in the z direction expressed in terms of the spherical basis functions.

$xh_n^{(2)}(x)$. Similarly, for the magnetic field of the plane wave, we have

$$\vec{H}^{inc} = \frac{1}{\eta} e^{-jkz} \vec{a}_y .$$

Converting it in the form of the product of the eigen functions and substituting the component in the direction of \vec{a}_r to (3.5d) gives

$$F_r^{inc} = \frac{\sin \phi}{\omega \eta} \sum_{n=1}^{\infty} j^{-n} \frac{2n+1}{n(n+1)} \hat{J}_n(x)|_{x=kr} P_n^1(x)|_{x=\cos \theta} . \quad (3.11)$$

3.1.5 Boundary Conditions

We use the superscript $(\cdot)^{(l)}$ to identify the l^{th} layer and its associated quantities. The scattered potentials, $A_r^{(L+1)}$ and $F_r^{(L+1)}$, propagate outward and take the following form

$$A_r^{(L+1)} = \frac{\cos \phi}{\omega} \sum_{n=1}^{\infty} a_n^{(L+1)} \hat{H}_n^{(2)}(x)|_{x=k^{(L+1)}r} P_n^1(x)|_{x=\cos \theta} , \quad (3.12a)$$

$$F_r^{(L+1)} = \frac{\sin \phi}{\omega \eta^{(L+1)}} \sum_{n=1}^{\infty} b_n^{(L+1)} \hat{H}_n^{(2)}(x)|_{x=k^{(L+1)}r} P_n^1(x)|_{x=\cos \theta} . \quad (3.12b)$$

The potentials inside the l^{th} layer ($l \neq 1$), $A_r^{(l)}$ and $F_r^{(l)}$, contain both the outward and inward propagating wave and take the following form

$$A_r^{(l)} = \frac{\cos \phi}{\omega} \sum_{n=1}^{\infty} \left[a_n^{(l)} \hat{H}_n^{(2)}(x)|_{x=k^{(l)}r} + c_n^{(l)} \hat{H}_n^{(1)}(x)|_{x=k^{(l)}r} \right] P_n^1(x)|_{x=\cos \theta} , \quad (3.13a)$$

$$F_r^{(l)} = \frac{\sin \phi}{\omega \eta^{(L+1)}} \sum_{n=1}^{\infty} \left[b_n^{(l)} \hat{H}_n^{(2)}(x)|_{x=k^{(l)}r} + d_n^{(l)} \hat{H}_n^{(1)}(x)|_{x=k^{(l)}r} \right] P_n^1(x)|_{x=\cos \theta} . \quad (3.13b)$$

The potentials inside the inner core ($l = 1$), $A_r^{(1)}$ and $F_r^{(1)}$, contain the standing wave and take the following form

$$A_r^{(1)} = \frac{\cos \phi}{\omega} \sum_{n=1}^{\infty} a_n^{(1)} \hat{J}_n(x)|_{x=k^{(1)}r} P_n^1(x)|_{x=\cos \theta} , \quad (3.14a)$$

$$F_r^{(1)} = \frac{\sin \phi}{\omega \eta^{(1)}} \sum_{n=1}^{\infty} b_n^{(1)} \hat{J}_n(x)|_{x=k^{(1)}r} P_n^1(x)|_{x=\cos \theta} . \quad (3.14b)$$

The boundary conditions at the interface between the $(l-1)^{th}$ layer and the l^{th} layer are the continuity of the tangential components of the electric and magnetic fields, which are⁶

$$E_{\theta}^{(l)}(r^{(l)}) = E_{\theta}^{(l-1)}(r^{(l)}) , \quad (3.15a)$$

$$H_{\theta}^{(l)}(r^{(l)}) = H_{\theta}^{(l-1)}(r^{(l)}) . \quad (3.15b)$$

⁶There is no need to consider $E_{\phi}^{(l)}$ and $H_{\phi}^{(l)}$ as they lead to the same equations.

Applying the boundary condition in (3.15a) to the fields of the inner core in (3.14) and the fields in the 2^{nd} layer in (3.13), we obtain

$$k^{(2)} \left[a_n^{(1)} \hat{J}_n'(x)|_{x=k^{(1)}r^{(1)}} \right] = k^{(1)} \left[a_n^{(2)} \hat{H}_n^{(2)'}(x)|_{x=k^{(2)}r^{(1)}} + c_n^{(2)} \hat{H}_n^{(1)'}(x)|_{x=k^{(2)}r^{(1)}} \right] , \quad (3.16a)$$

$$k^{(2)} \left[b_n^{(1)} \hat{J}_n(x)|_{x=k^{(1)}r^{(1)}} \right] = k^{(1)} \left[b_n^{(2)} \hat{H}_n^{(2)}(x)|_{x=k^{(2)}r^{(1)}} + d_n^{(2)} \hat{H}_n^{(1)}(x)|_{x=k^{(2)}r^{(1)}} \right] . \quad (3.16b)$$

Applying the boundary condition in (3.15b) to the fields of the inner core in (3.14) and the fields in the 2^{nd} layer in (3.13), we obtain

$$\mu^{(2)} \left[a_n^{(1)} \hat{J}(x)|_{x=k^{(1)}r^{(1)}} \right] = \mu^{(1)} \left[a_n^{(2)} \hat{H}_n^{(2)}(x)|_{x=k^{(2)}r^{(1)}} + c_n^{(2)} \hat{H}_n^{(1)}(x)|_{x=k^{(2)}r^{(1)}} \right] , \quad (3.17a)$$

$$\mu^{(2)} \left[b_n^{(1)} \hat{J}_n'(x)|_{x=k^{(1)}r^{(1)}} \right] = \mu^{(1)} \left[b_n^{(2)} \hat{H}_n^{(2)'}(x)|_{x=k^{(2)}r^{(1)}} + d_n^{(2)} \hat{H}_n^{(1)'}(x)|_{x=k^{(2)}r^{(1)}} \right] . \quad (3.17b)$$

Applying the boundary condition in (3.15a) to the fields of the $(l-1)^{th}$ layer and the fields of the l^{th} layer as in (3.13), we obtain

$$\begin{aligned} k^{(l)} \left[a_n^{(l-1)} \hat{H}_n^{(2)'}(x)|_{x=k^{(l-1)}r^{(l-1)}} + c_n^{(l-1)} \hat{H}_n^{(1)'}(x)|_{x=k^{(l-1)}r^{(l-1)}} \right] \\ = k^{(l-1)} \left[a_n^{(l)} \hat{H}_n^{(2)'}(x)|_{x=k^{(l)}r^{(l-1)}} + c_n^{(l)} \hat{H}_n^{(1)'}(x)|_{x=k^{(l)}r^{(l-1)}} \right] , \end{aligned} \quad (3.18a)$$

$$\begin{aligned} k^{(l)} \left[b_n^{(l-1)} \hat{H}_n^{(2)}(x)|_{x=k^{(l-1)}r^{(l-1)}} + d_n^{(l-1)} \hat{H}_n^{(1)}(x)|_{x=k^{(l-1)}r^{(l-1)}} \right] \\ = k^{(l-1)} \left[b_n^{(l)} \hat{H}_n^{(2)}(x)|_{x=k^{(l)}r^{(l-1)}} + d_n^{(l)} \hat{H}_n^{(1)}(x)|_{x=k^{(l)}r^{(l-1)}} \right] . \end{aligned} \quad (3.18b)$$

Applying the boundary condition in (3.15b) to the fields of the $(l-1)^{th}$ layer and the fields of the l^{th} layer as in (3.13), we obtain

$$\begin{aligned} \mu^{(l)} \left[a_n^{(l-1)} \hat{H}_n^{(2)}(x)|_{x=k^{(l-1)}r^{(l-1)}} + c_n^{(l-1)} \hat{H}_n^{(1)}(x)|_{x=k^{(l-1)}r^{(l-1)}} \right] \\ = \mu^{(l-1)} \left[a_n^{(l)} \hat{H}_n^{(2)}(x)|_{x=k^{(l)}r^{(l-1)}} + c_n^{(l)} \hat{H}_n^{(1)}(x)|_{x=k^{(l)}r^{(l-1)}} \right] , \end{aligned} \quad (3.19a)$$

$$\begin{aligned} & \mu^{(l)} \left[b_n^{(l-1)} \hat{H}_n^{(2)'}(x)|_{x=k^{(l-1)}r^{(l-1)}} + d_n^{(l-1)} \hat{H}_n^{(1)'}(x)|_{x=k^{(l-1)}r^{(l-1)}} \right] \\ &= \mu^{(l-1)} \left[b_n^{(l)} \hat{H}_n^{(2)'}(x)|_{x=k^{(l)}r^{(l-1)}} + d_n^{(l)} \hat{H}_n^{(1)'}(x)|_{x=k^{(l)}r^{(l-1)}} \right] . \end{aligned} \quad (3.19b)$$

Applying the boundary condition in (3.15a) to the fields of the L^{th} layer, the incident field in (3.10) and (3.11), and the scattered field in (3.12), we obtain

$$\begin{aligned} & k^{(L+1)} \left[a_n^{(L)} \hat{H}_n^{(2)'}(x)|_{x=k^{(L)}r^{(L)}} + c_n^{(L)} \hat{H}_n^{(1)'}(x)|_{x=k^{(L)}r^{(L)}} \right] \\ &= k^{(L)} \left[a_n^{(L+1)} \hat{H}_n^{(2)'}(x)|_{x=k^{(L+1)}r^{(L)}} + j^{-n} \frac{2n+1}{n(n+1)} \hat{J}_n'(x)|_{x=k^{(L+1)}r^{(L)}} \right] , \end{aligned} \quad (3.20a)$$

$$\begin{aligned} & k^{(L+1)} \left[b_n^{(L)} \hat{H}_n^{(2)}(x)|_{x=k^{(L)}r^{(L)}} + d_n^{(L)} \hat{H}_n^{(1)}(x)|_{x=k^{(L)}r^{(L)}} \right] \\ &= k^{(L)} \left[b_n^{(L+1)} \hat{H}_n^{(2)}(x)|_{x=k^{(L+1)}r^{(L)}} + j^{-n} \frac{2n+1}{n(n+1)} \hat{J}_n(x)|_{x=k^{(L+1)}r^{(L)}} \right] . \end{aligned} \quad (3.20b)$$

Applying the boundary condition in (3.15b) to the fields of the L^{th} layer, the incident field in (3.10) and (3.11), and the scattered field in (3.12), we obtain

$$\begin{aligned} & \mu^{(L+1)} \left[a_n^{(L)} \hat{H}_n^{(2)}(x)|_{x=k^{(L)}r^{(L)}} + c_n^{(L)} \hat{H}_n^{(1)}(x)|_{x=k^{(L)}r^{(L)}} \right] \\ &= \mu^{(L)} \left[a_n^{(L+1)} \hat{H}_n^{(2)}(x)|_{x=k^{(L+1)}r^{(L)}} + j^{-n} \frac{2n+1}{n(n+1)} \hat{J}_n(x)|_{x=k^{(L+1)}r^{(L)}} \right] , \end{aligned} \quad (3.21a)$$

$$\begin{aligned} & \mu^{(L+1)} \left[b_n^{(L)} \hat{H}_n^{(2)'}(x)|_{x=k^{(L)}r^{(L)}} + d_n^{(L)} \hat{H}_n^{(1)'}(x)|_{x=k^{(L)}r^{(L)}} \right] \\ &= \mu^{(L)} \left[b_n^{(L+1)} \hat{H}_n^{(2)'}(x)|_{x=k^{(L+1)}r^{(L)}} + j^{-n} \frac{2n+1}{n(n+1)} \hat{J}_n'(x)|_{x=k^{(L+1)}r^{(L)}} \right] . \end{aligned} \quad (3.21b)$$

3.1.6 System of Equations and its Solution

Associated with A_r are $2L$ unknowns, which include $a_n^{(l)}$ where $l = 1 \dots L+1$ and $c_n^{(l)}$ where $l = 2 \dots L$. There are also $2L$ equations associated with A_r , which include (3.16a) and (3.17a) at the inner most interface, (3.18a) and (3.19a) at the $2 \dots L-1^{th}$ interface, and (3.20a) and (3.21a) at the outer most interface. These unknowns and equations form a $2L \times 2L$ linear system. As we are interested in the scattered field in this study, we need to

solve this system for only one coefficient $a_n^{(L+1)}$. Similarly, there are $2L$ unknowns and $2L$ equations from (3.16b), (3.17b), (3.18b), (3.19b), (3.20b), and (3.21b) for F_r . We need to solve this linear system for the coefficient $b_n^{(L+1)}$.

Solving the linear systems at all n gives the coefficients needed to express $A_r^{(L+1)}$ and $F_r^{(L+1)}$ in (3.12). Substituting them to (3.5) gives the scattered electric field as

$$E_r^{(L+1)} = -j \cos \phi \sum_{n=1}^{\infty} a_n^{(L+1)} \left[\hat{H}_n^{(2)''}(x)|_{x=k^{(L+1)}r} + \hat{H}_n^{(2)}(x)|_{x=k^{(L+1)}r} \right] P_n^1(x)|_{x=\cos \phi} , \quad (3.22a)$$

$$E_\theta^{(L+1)} = \frac{\cos \phi}{k^{(L+1)}r} \sum_{n=1}^{\infty} \left[j a_n^{(L+1)} \hat{H}_n^{(2)'}(x)|_{x=k^{(L+1)}r} \sin \theta P_n^{1'}(x)|_{x=\cos \theta} \right. \\ \left. - b_n^{(L+1)} \hat{H}_n^{(2)}(x)|_{x=k^{(L+1)}r} \frac{P_n^1(x)}{\sin \theta} \Big|_{x=\cos \theta} \right] , \quad (3.22b)$$

$$E_\phi^{(L+1)} = \frac{\sin \phi}{k^{(L+1)}r} \sum_{n=1}^{\infty} \left[j a_n^{(L+1)} \hat{H}_n^{(2)'}(x)|_{x=k^{(L+1)}r} \frac{P_n^1(x)}{\sin \theta} \Big|_{x=\cos \theta} \right. \\ \left. - b_n^{(L+1)} \hat{H}_n^{(2)}(x)|_{x=k^{(L+1)}r} \sin \theta P_n^{1'}(x)|_{x=\cos \theta} \right] . \quad (3.22c)$$

3.2 Implementation and Validation

The infinite sum in (3.22) is approximated by a finite sum. The number of terms, N_{\max} , is empirically determined by $N_{\max} = \max(N_{\text{stop}}, |m^{(l)}x^{(l)}|, |m^{(l)}x^{(l-1)}|) + 15$, $l = 1, 2, \dots, L$, where $m^{(l)}$ is the relative refractive index $m^{(l)} = n^{(l)}/n^{(L+1)}$ and $x^{(l)}$ is related to the size of each layer as $x^{(l)} = k^{(L+1)}r^{(l)}$ [137]. The value of N_{stop} is the integer closest to

$$N_{\text{stop}} = \begin{cases} x^{(L)} + 4(x^{(L)})^{\frac{1}{3}} + 1, & 0.02 \leq x^{(L)} < 8 , \\ x^{(L)} + 4.05(x^{(L)})^{\frac{1}{3}} + 2, & 8 \leq x^{(L)} < 4200 , \\ x^{(L)} + 4(x^{(L)})^{\frac{1}{3}} + 2, & 4200 \leq x^{(L)} < 20000 . \end{cases}$$

The derivatives of $\hat{B}_n(x)$ in (3.22) are computed from their recurrent relations

$$\begin{aligned}\hat{B}_n'(x) &= \frac{1}{2} \left[\hat{B}_{n-1}(x) + \frac{1}{x} \hat{B}_n(x) - \hat{B}_{n+1}(x) \right] , \\ \hat{B}_n''(x) &= \frac{1}{2} \left[\hat{B}_{n-1}'(x) + \frac{1}{x} \hat{B}_n'(x) - \frac{1}{x^2} \hat{B}_n(x) - \hat{B}_{n+1}'(x) \right] ,\end{aligned}$$

which are easily derived from the recurrent relations of spherical Bessel functions. The associated Legendre polynomial is defined as⁷

$$P_n^m(x) = (-1)^m (1-x^2)^{m/2} \frac{d^m}{dx^m} P_n(x) .$$

In this study, we are interested in the scattered field at $\theta = \pi$. Directly substituting $\theta = \pi$ into (3.22b) and (3.22c) incurs numerical difficulty when evaluating $\frac{P_n^1(x)}{\sin \theta}|_{x=\cos \theta}$ and $\sin \theta P_n^{1'}(x)|_{x=\cos \theta}$. This numerical difficulty is resolved by the recurrent relations of the associated Legendre polynomial. It is shown in Appendix A that

$$\frac{P_n^1(x)}{\sin \theta}|_{x=\cos \theta} = (-1)^n \frac{n(n+1)}{2}, \quad \theta = \pi, \quad (3.23a)$$

$$\sin \theta P_n^{1'}(x)|_{x=\cos \theta} = (-1)^n \frac{n(n+1)}{2}, \quad \theta = \pi. \quad (3.23b)$$

Fig. 3.3 shows the normalized mono-static radar cross sections of a dielectric sphere with a relative permittivity of 2.25 and a radius of one background wavelength. The figure is consistent with the result reported in [30]. Fig. 3.4 demonstrates the scenario that an x -polarized plane wave propagating in the z direction is scattered by a three-layer dielectric sphere with the relative permittivity of 2, 8 and 4 and the radii of 1.5, 1 and 0.6 normalized to the background wavelength. The total field of $|H_r|$ and $|H_\theta|$ on the y - z plane passing through the origin are shown in Fig. 3.4. The continuity of these tangential components demonstrates the correctness in the solution to the linear systems and the implementation of (3.22).

⁷This definition of the associated Legendre polynomial contains the term $(-1)^m$, known as the Condon-Shortly phase [5, pp. 772]. The definition including this term is adopted in [7, pp. 951], [61, pp. 108], and [52, pp. 468]. Care must be exercised when comparing results in the books that use different definitions.

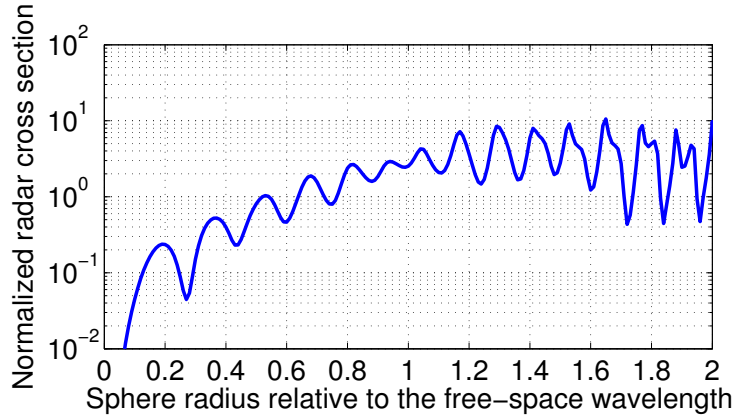


Fig. 3.3 Normalized mono-static radar cross section of a dielectric sphere with a relative permittivity of 2.25 and a radius of one background wavelength [30].

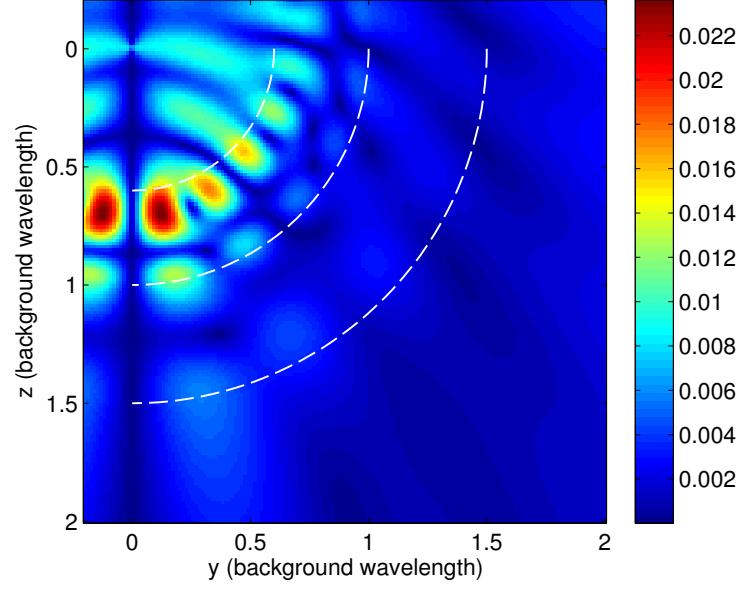
3.3 Results

We use a two-layer sphere to approximate the skin and tissue. The skin has a fixed thickness of 1.5 mm. We use a three-layer sphere to approximate the skin, tissue, and tumor. The mid-layer represents the tissue with a thickness of 40 mm, 50 mm, and 60 mm. The inner core represents the tumor with a diameter of 2 mm, 3 mm, 4 mm and 5 mm.

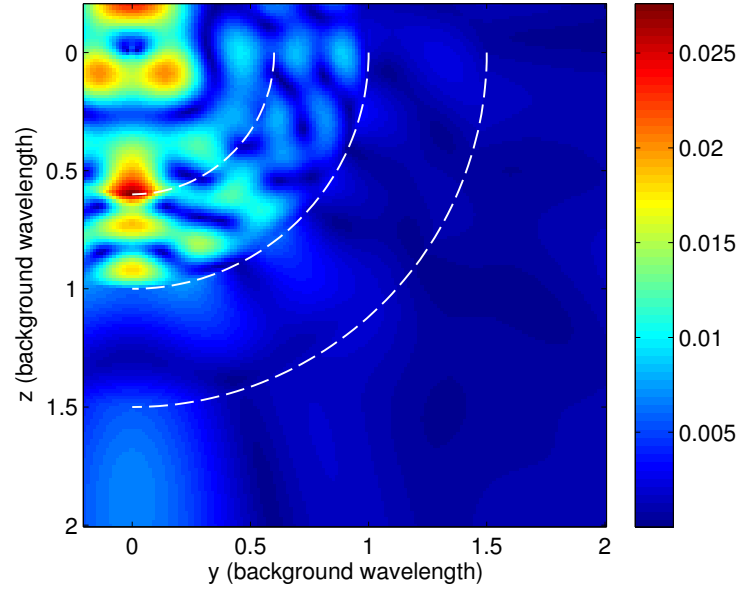
The frequency-dependent dispersion of tissue is described by the Cole-Cole model [23], in which the complex relative permittivity is

$$\epsilon_r^* = \epsilon_\infty + \frac{\Delta\epsilon}{1 + (j\omega\tau)^{1-\alpha}} + \frac{\sigma_s}{j\omega\epsilon_o} ,$$

where ϵ_∞ is the relative permittivity for infinite value of frequency, and $\Delta\epsilon$ is the difference between the infinite and static relative permittivity. τ is the relaxation time constant and σ_s is the static conductivity. The value of the parameter α is determined experimentally as a correction factor. The Cole-Cole parameters associated with the three groups of tissue categorized based on their adipose content and the malignant tissue are listed Table 3.1 [84, 86]. The Cole-Cole parameters associated with skin are also listed [41]. A matching medium with a relative permittivity of 3 is assumed in this calculation. An x -polarized plane wave is radiated towards the breast model as shown in Fig. 3.1. The reflected electric field $\vec{E}^{(L+1)}$ and magnetic field $\vec{H}^{(L+1)}$, i.e. $\theta = \pi$, 30 mm away from the model are recorded.



(a)



(b)

Fig. 3.4 Total field of (a) $|H_r|$ and (b) $|H_\theta|$ as the x -polarized plane wave interacts with a three-layer dielectric sphere with the relative permittivity of 2, 8 and 4 and the radii of 1.5, 1 and 0.6 of a background wavelength.

Table 3.1 Cole-Cole parameters of the breast tissue, tumor, and skin valid from 0.5 GHz to 20 GHz

Tissue Group	ϵ_∞	σ_s S/m	$\Delta\epsilon$	τ ps	α
0-30%	7.821	0.713	41.48	10.66	0.047
31-85%	5.573	0.524	34.57	9.149	0.095
86-100%	3.14	0.036	1.708	14.65	0.061
Tumor	9.058	0.899	51.31	10.85	0.022
skin	4.0	0.0002	32	7.23	0
	-	-	1100	32480	0.2

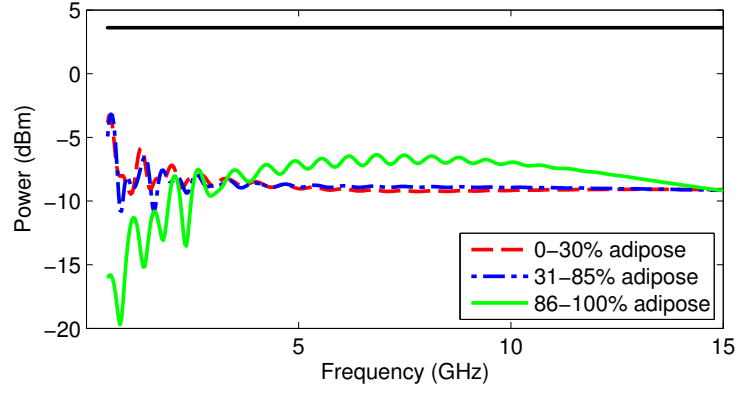
The reflected electric fields in the y and z direction are zero due to the symmetry of the problem. The incident power density is 2.3 mW/m^2 , and we calculate the reflected power density through

$$\frac{1}{2} \Re \{ \vec{E}^{(L+1)} \times \vec{H}^{(L+1)*} \} .$$

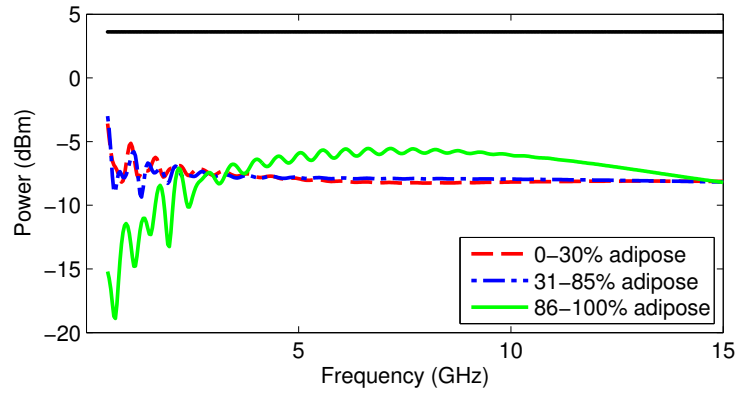
Fig. 3.5 show the reflected power by a three-layer sphere with a tumor when being buried in the tissue specified in Table 3.1 with a thickness of 40-mm, 50-mm, and 60-mm. Given the relative permittivity of the background being 3, the wavelength is from 346 mm to 11.5 mm in the frequency range from 500 MHz to 15 GHz. The wavelength is comparable to the dimension of the multi-layer sphere; thus, Mie scattering occurs. The reflected power is about 20 dB below the incident power for the three tissue types, which is well within the dynamic range of frequency-domain instruments.

For pulse-based microwave imaging, the reflected signal contains the reflection due to the tumor, the distortion due to the tissue, and noise. The distortion modelled in this study is the frequency-dependent dispersion, which extends the temporal width of the pulse and attenuates its amplitude.

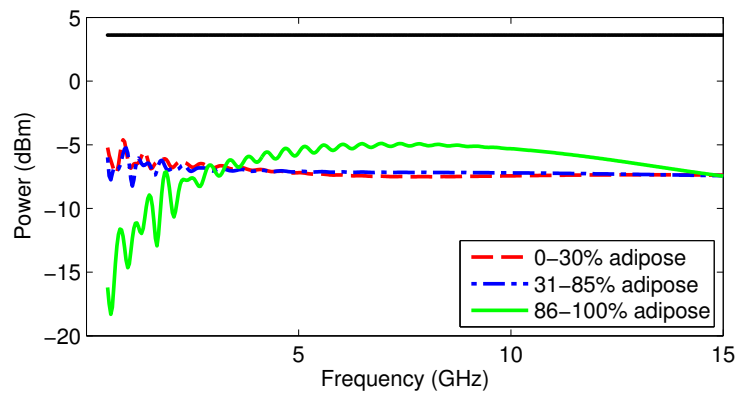
To discern the effect due to the presence of a tumor, we define the differential power to be the difference in the reflected power with and without the tumor presence. Fig. 3.6 shows the differential power due to 2-mm, 3-mm, 4-mm, and 5-mm diameter tumor in the three types of tissue. From Fig. 3.6(a), we observe that the reflected power due to the tumor presence increases as the tumor size increases. Cross comparing Figs. 3.6(a), 3.6(b), 3.6(c), we observe that the differential power increases as the contrast in the dielectric properties



(a)



(b)



(c)

Fig. 3.5 Reflected power as the surrounding tissue being (a) 40 mm, (b) 50 mm, and (c) 60 mm thick.

between the tumor and tissue increases. We also observe that the differential power spans a spectrum from 500 MHz to 5 GHz in the tissue containing 0-30% adipose and 30-85% adipose. It spans a wider spectrum beyond 10 GHz in the tissue containing more than 85% adipose. This is due to the resonance occurring in the adipose-domain tissue. Power Resolution specifies the minimal amount of power variation discernible by an frequency-domain instrument. For instance, the Agilent N5241A Network analyzer has a power resolution of 0.01 dB [2]. From Figs. 3.6(a), 3.6(b), 3.6(c), we observe that the power reflected by a tumor bigger than 3 mm in the adipose-dominant tissue is greater than this resolution, while power reflected by tumors of other sizes in the tissue containing less adipose are smaller than this resolution. This makes the tumor detection problem more challenging.

Figs. 3.7 and 3.8 show the differential power as the tissue being 50-mm and 60-mm thick. We observe an increase in the differential power as the tumor size increases and as the contrast in the dielectric properties increases. Comparing Figs. 3.6, 3.7, and 3.8, we also observe that the differential power decreases due to the increasing attenuation as the tissue thickness increases.

3.4 Conclusions

In this chapter, we studied the problem of a plane wave scattered by a multi-layer sphere. The solution to this problem showed that the reflected wave are about 20 dB below the incident wave. The differential power calculated from the reflected wave increases as the tumor size increase and the contrast in the dielectric properties between tumor and tissue increase. However, at the reduced contrast level identified in [84, 86], the differential power places a stringent requirement on the equipments for the mono-static measurement. And finally, the tumor-reflected power concentrates in the frequency range less than 5 GHz for the tissue containing little adipose and extends beyond 10 GHz for the tissue containing mostly adipose.

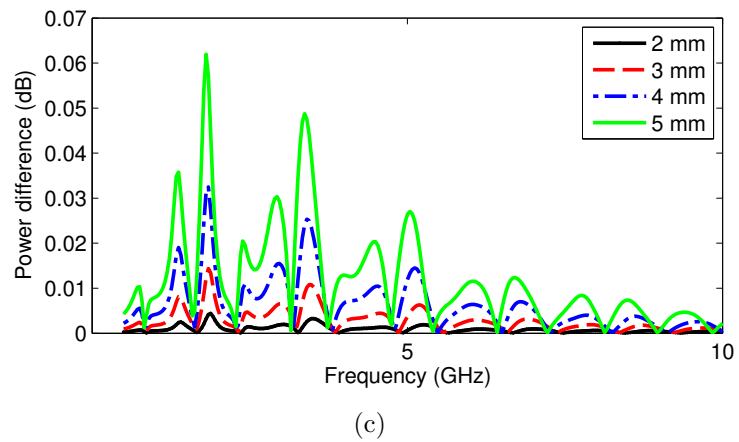
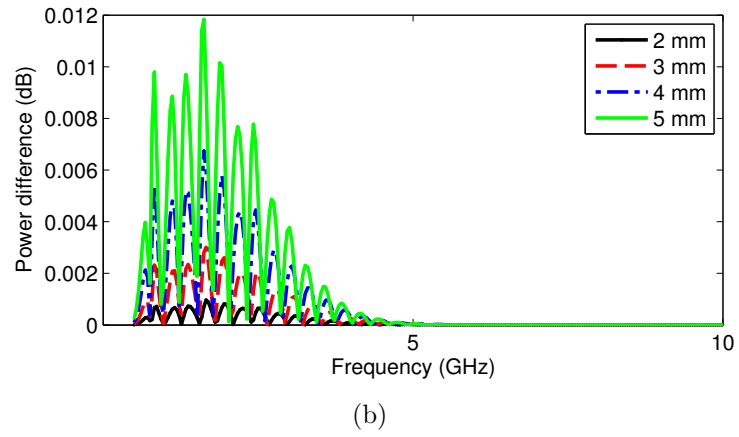
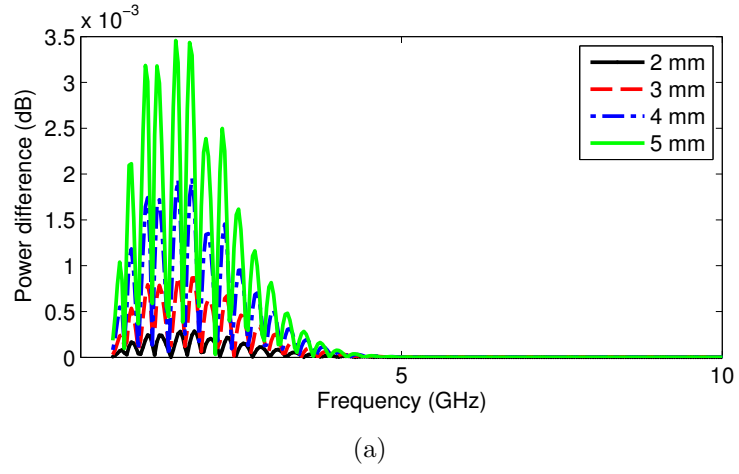
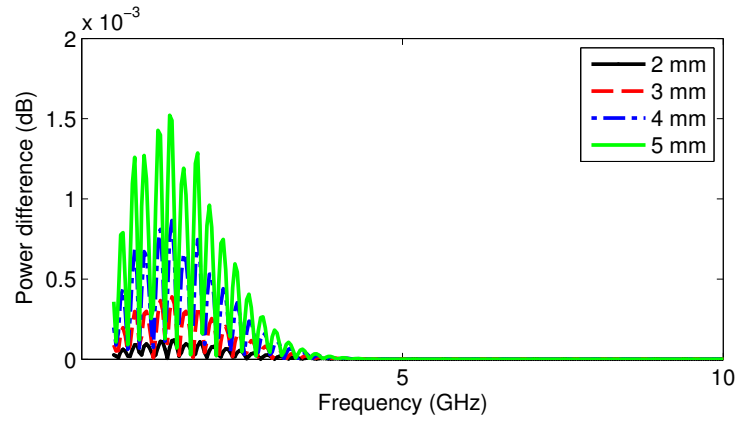
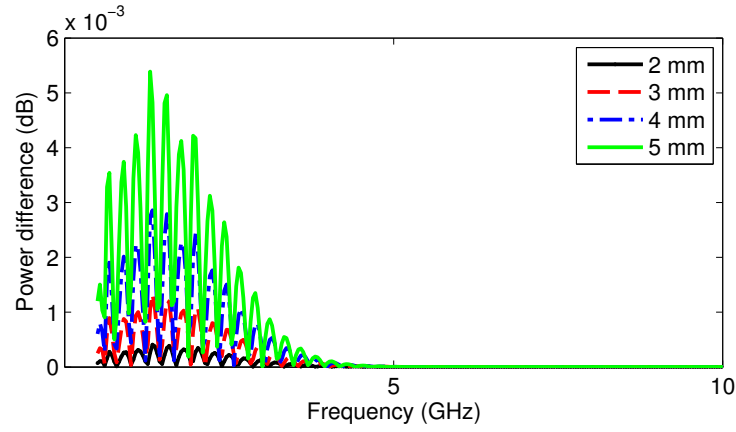


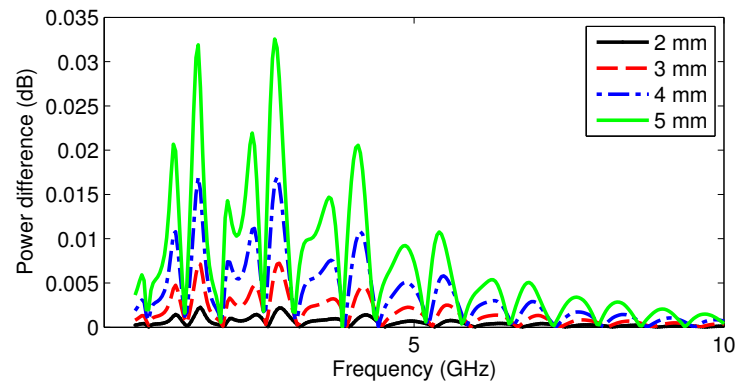
Fig. 3.6 Differential power due to the presence of a tumor with the tissue being 40-mm thick and containing (a) 0-30%, (b) 31-85%, and (c) 86-100% of adipose.



(a)

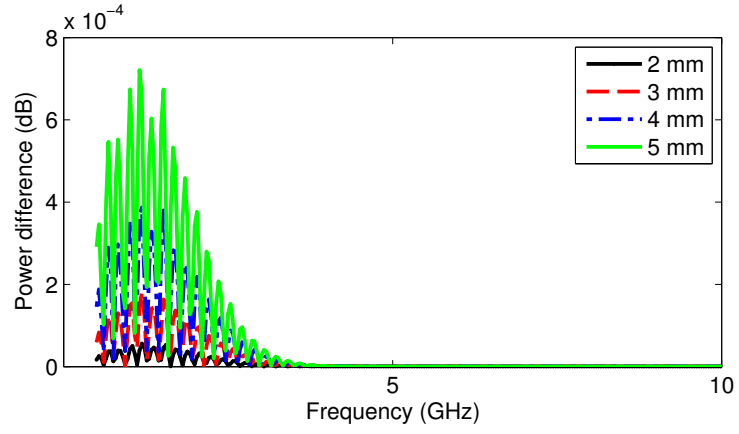


(b)

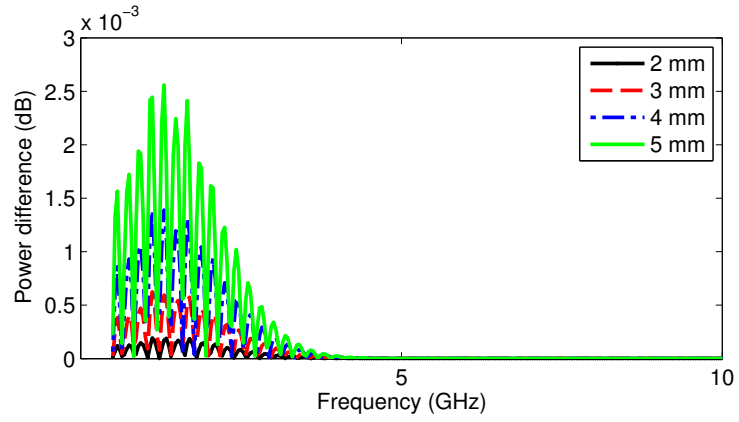


(c)

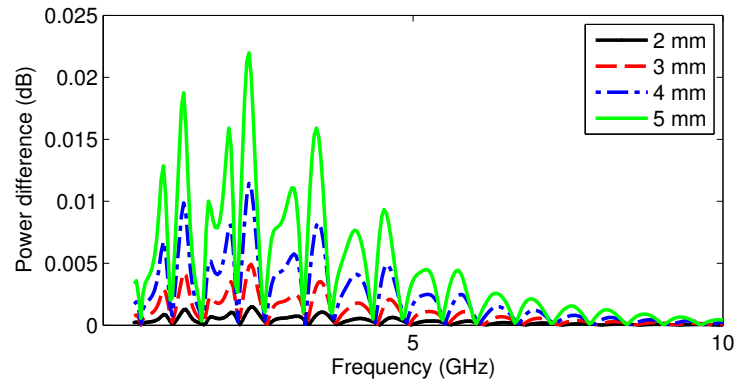
Fig. 3.7 Differential power due to the presence of a tumor with the tissue being 50-mm thick and containing (a) 0-30%, (b) 31-85%, and (c) 86-100% of adipose.



(a)



(b)



(c)

Fig. 3.8 Differential power due to the presence of a tumor with the tissue being 60-mm thick and containing (a) 0-30%, (b) 31-85%, and (c) 86-100% of adipose.

Chapter 4

Building Numerical Breast Models

Simulating the interaction of a microwave pulse and a human breast provides an efficient and safe mean to access the field distributions. Modern electromagnetic software allows to combine breast models and complex antenna structures, and can support the coupling with microwave circuit simulators. These features simplify the design process of microwave radar systems.

Early numerical studies of microwave radar systems rely on data from simulations of two-dimensional breast models, as the research objective was on the imaging and detection algorithms. The breast tissue was assumed homogeneous, or with randomly added heterogeneity, or mapped to a range of possible values of permittivity and conductivity guided by some magnetic resonance images. Three-dimensional simulations were reported for microwave interaction with breast models in the shape of half ellipsoids [27] or in more realistic shapes derived from magnetic resonance images [135, 136]. In those studies, the tissue was assumed homogeneous.

After the characterization of the dielectric properties of breast tissue [84, 86], a set of nine numerical breast models have been made publicly available [147]. Each model consists of a spatial volume filled with small cubes with a dimension of $0.5\text{ mm} \times 0.5\text{ mm} \times 0.5\text{ mm}$. The tissue heterogeneity is captured by mapping the pixels in the magnetic resonance images to the dielectric properties assigned to the cubes. Such models are suitable for simulations that are based on the finite-difference time-domain (FDTD) method, and involve antennas of simple geometric shapes [126]. Each cube of the breast models can denote a Yee cell [145], and the dielectric properties assigned to the cube are used to calculate the

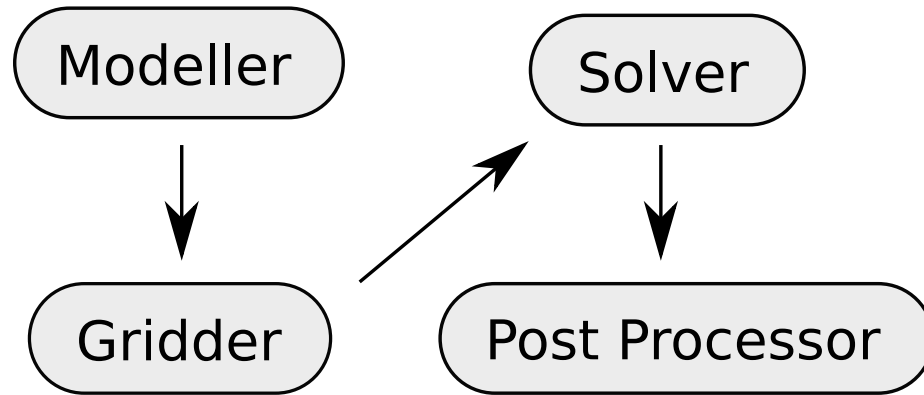


Fig. 4.1 Components commonly involved in an electromagnetic software. The direction of the arrow indicates the work flow.

coefficients in the FDTD update equations. However, if the antennas have complex shapes, it is difficult to conform the FDTD grid setting of the breast models to the grid setting needed to resolve the shapes of the antennas.

Today's computational electromagnetic software based on the FDTD method commonly consists of four components shown in Fig. 4.1: a Modeller that creates the geometric shapes to represent objects, assigns them dielectric properties, and specifies excitations and boundary conditions; a Gridder that analyzes the curvature of objects and generates a graded rectangular mesh; a Solver that implements the FDTD method or its close variants to solve for the electromagnetic fields; a Post Processor that converts the field solutions to macroscopic parameters that are of interest to engineers. The advantage of using commercial software to simulate microwave radar systems is that numerical breast models and antennas are easily imported to the Modeller, and a common grid can be automatically generated by the Gridder based on their shapes. However, commercial software does not provide the low-level control of assigning each Yee cell a different set of dielectric properties. One way to incorporate the breast models introduced in [147] is to create one solid for each cube in the Modeller, which leads to hundreds of thousands of solids. Creating this number of solids practically renders the Modeller unusable.

In this chapter, we present a procedure to build numerical breast models from magnetic resonance images, suitable for commercial electromagnetic software. The idea is to use the classification and regression tree (CART) analysis to identify regions consisting of neighbouring pixels of similar intensities in the images. The level of similarity is determined by a user-selected factor. Each of these regions is presented as a solid in the Modeller, and

the solids fill out the tissue region. This procedure can reduce the hundreds of thousands of solids to a few hundreds depending on the user-selected factor.

The electric field is related to the electric flux density through the constitutive relation, which characterizes the medium under study. Previous studies have used the dielectric model and the Debye model for the constitutive relation to characterize the breast tissue. We discuss the effect of these material models on the signals generated from the breast models. It is shown that the Debye model is needed to represent the lossy nature of the breast tissue.

In this work, SEMCAD from Schmid & Partner Engineering AG, Zurich, Switzerland [124], was used to build the breast models and perform FDTD simulations.

This chapter is structured as follows. Section 4.1, describes the procedure of building the breast models, particularly the CART analysis. Section 4.2 presents an example to illustrate our methodology. Section 4.3 discusses the effect of tissue modelling using the dielectric model and the Debye model. Section 4.4 concludes this chapter.

4.1 Model Construction

The T1-weighted magnetic resonance images were obtained from the Royal Victoria Hospital, Montreal, Canada. The parameters associated with these images are the following: a 1.5 T static magnetic field strength; a gradient-echo pulse sequence with a pulse flip angle of 25°; a repetition time of 8.816 ms; and an echo time of 4.2 ms. There are 68 tomographic images along the upper body of a patient acquired at a spatial increment of 2 mm. Each image contains 512×512 pixels at a resolution of 0.703 mm×0.703 mm per pixel. One set of these images corresponds to a volume of 360 mm×360 mm×136 mm. Building a breast model from this stack of images involves three stages: segmentation that separates the skin from the background and tissue region; tissue approximation that captures the heterogeneity; and assignment of the dielectric properties. These stages are elaborated in the following sub-sections.

4.1.1 Image Segmentation

The image segmentation involves manual identification of the breast and its separation from the background. We then separate the skin from the tissue region. The pixel-by-pixel segmentation result is imported into software called Amira [131] to perform the volume

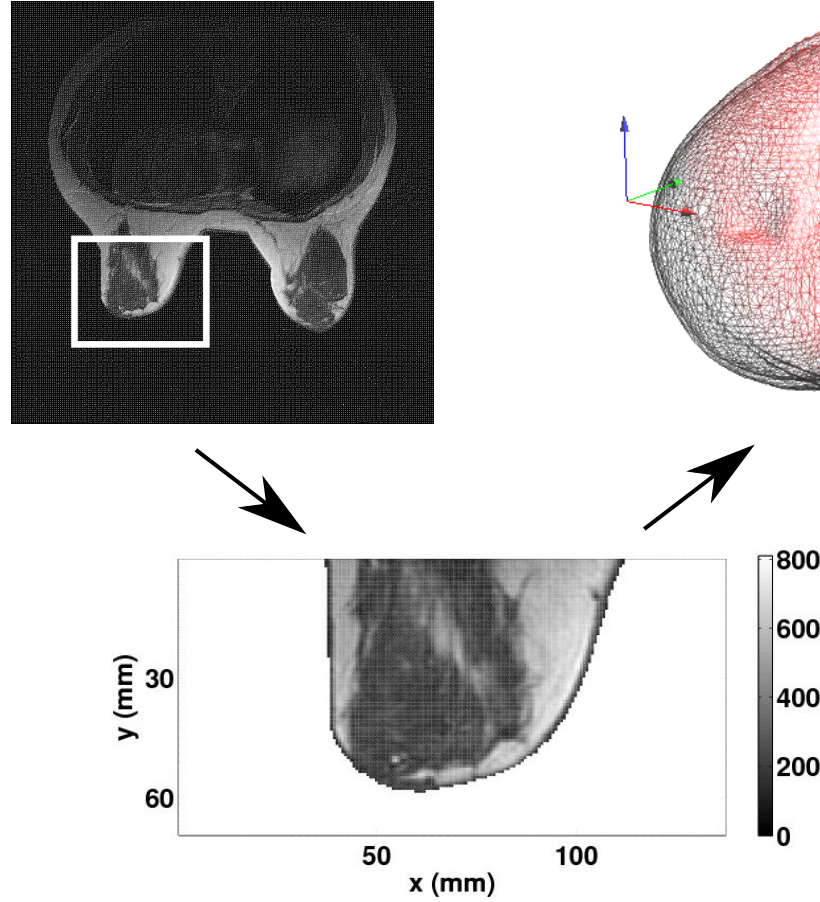


Fig. 4.2 A tomographic image of a patient's upper body, the segmented image (the black stroke traces out the skin), and the skin and tissue wire frames.

reconstruction. The outputs from Amira are two three-dimensional wire frames, one for the skin and the other for the tissue region. The interior of the wire frame of the skin conforms to the exterior of the wire frame of the tissue region. One of the tomographic images of a patient's upper body, the segmented image, and the three-dimensional wire frames constructed in Amira are shown in Fig. 4.2

4.1.2 Tissue Approximation

We use the term “voxel” to refer to the $0.703 \text{ mm} \times 0.703 \text{ mm} \times 2 \text{ mm}$ cubic volume that surrounds a pixel in a magnetic resonance image defined by the image resolution and image separation. We use the term “voxel intensity” to refer to the intensity of the image pixel

enclosed within the cubic volume. Directly creating a solid for each voxel in the tissue region captures the heterogeneity of the tissue, but also leads to hundreds of thousands of solids in the Modeller.

It is desirable to reduce the number of solids by developing a much simpler model that preserves the heterogeneity of tissue to within a small approximation error. Moreover, it is questionable whether the individual voxel intensity measurement accurately reflects the underlying dielectric properties of tissue. There is noise in the measurements, which causes the voxel intensities to deviate from the effect of the T1 relaxation of protons. We can form better estimates of the true intensities by exploiting the local spatial smoothness that should be present in the images — the T1 relaxation time should not change drastically throughout the breast except where there are structural discontinuities, e.g., transitions from glandular to adipose tissue.

We adopt a version of the CART analysis to estimate the underlying true intensities [13]. The CART analysis involves successively partitioning the tissue to the smallest possible regions and merge them with the help of a regression tree. The process of partitioning and merging are pictorially described as the growing and pruning of the regression tree. Such a tree decomposition has been used before in the analysis of magnetic resonance images — both for the identification of activity regions in functional magnetic resonance images [51] and in multi-resolution analysis for image denoising [53, 107].

Let $\{x_1 \dots x_N\}$ be an ordered set, representing the voxel intensities in a tissue region. This set also represents the root node of the regression tree.¹ The partition index, p , is selected according to the criterion²

$$\min_{p \in 1 \dots N} [\text{MSE}(\{x_1 \dots x_p\}) + \text{MSE}(\{x_{p+1} \dots x_N\})] , \quad (4.1)$$

where $\text{MSE}(\cdot)$ denotes the mean-squared error of its argument and N is the number of voxels. An heuristic method can be used to determine the value of p by iteratively partitioning the set at each possible value of p and comparing the sum of the mean-squared errors. The ordered set $\{x_1 \dots x_N\}$ and its subsets $\{x_1 \dots x_p\}$ and $\{x_{p+1} \dots x_N\}$ are also called the “parent node” and “child nodes”. Each subset is further partitioned into two smaller sets according to (4.1). This partitioning continues until the mean-squared error of the smallest sets are

¹It is understood from here on that each node can also be represented as an ordered set.

²The regression tree is a binary tree, i.e. a node has two child nodes, if it is not a leaf node.

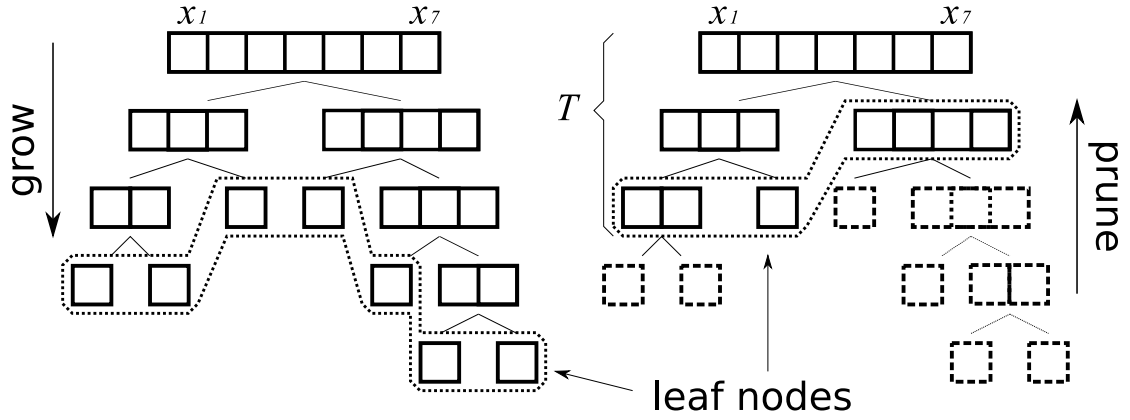


Fig. 4.3 A one-dimensional example to demonstrate the growing and pruning of the regression tree. The growing process (on the left) involves successive partitioning of a parent node by minimizing the mean-squared error of its two child nodes. The pruning process (on the right) involves comparing the mean-squared error of the parent node, the sum of the mean-squared errors of the child nodes, and the complexity penalty. If the mean-squared error of the parent node is smaller, the two child nodes are pruned.

0. These sets are the leaf nodes of the regression tree.

The exact match between the voxels and the leaf nodes may seem desirable; however, it is indicative of over-fitting. We are building a model that fits the noise inherent in the measurements, rather than revealing the true function lurking beneath the noise. For this reason, the second phase of the CART analysis involves pruning, in which leaf nodes are successively merged. The tree, T , as the result of pruning, is selected according to the criterion

$$\min_T \hat{L}(T) + \alpha|T|, \quad (4.2)$$

where $\hat{L}(T)$ is the empirical risk, an error measure between the regression tree and the data, $|T|$ is the number of leaf nodes, and α is a user-selected constant that controls the trade-off between the fidelity to the data and the complexity of the regression tree. α is also known as the complexity penalty.³ When $\alpha = 0$, the tree that satisfies (4.2) is the un-pruned tree. The empirical risk we adopt is the mean-squared error, which is

$$\hat{L}(T) = \frac{1}{N} \sum_{i=1}^N (\hat{f}_T(i) - x_i)^2,$$

³It is the penalty paid for using a more complex model to fit the data.

where $\hat{f}_T(i)$ is the average voxel intensity of the leaf node that contains the i^{th} voxel. The phase of growing and pruning the regression tree is illustrated in Fig. 4.3.

4.1.3 Selection of the Complexity Penalty

Choosing an appropriate complexity penalty α is a challenging task. The intuitive goal is to construct a model that is as simple as possible, but still provides a sufficiently accurate description of the voxel intensities. Usually in regression, the goal is to minimize the true risk, which is the mean squared error between the underlying voxel intensity function and our estimate. This true risk cannot be directly evaluated because the underlying voxel intensity function is unknown. If a good model for the image noise is available, it is possible to identify a complexity penalty that ensures the true risk is upper-bounded [125].

The primary goal in our work is not really to minimize the mean-squared error between the regression tree and the voxel intensities. Our task is to ensure we build the simplest model that sufficiently captures the heterogeneity of the breast tissue. We could have achieved this, if we knew the true voxel intensity function and selected the complexity penalty at which the smallest tumor response under study is greater than the error introduced by the approximation of the intensity function.

4.1.4 Assignment of the Dielectric Properties

The healthy breast tissue is categorized into three groups based on their adipose content: Group I (0-30%), Group II (31-85%), and Group III (86-100%); their dielectric properties are specified at the 25th, 50th, and 75th percentile of the samples belonging to each group [84, 86]. In our work, we use this data and follow the approach in [147], which uses a two-component Gaussian mixture model to approximate the distribution of the voxels. Fig. 4.4 shows the two-component Gaussian mixture model designed to fit the distribution of the voxels in the tissue region using the Expectation Maximization algorithm [28].

The constitutive relation between the electric field \vec{E} and electric flux density \vec{D} in the frequency domain is

$$\vec{D} = \epsilon_o \epsilon_r^* \vec{E}$$

where ϵ_o is the absolute permittivity in vacuum and ϵ_r^* is the complex relative permittivity.

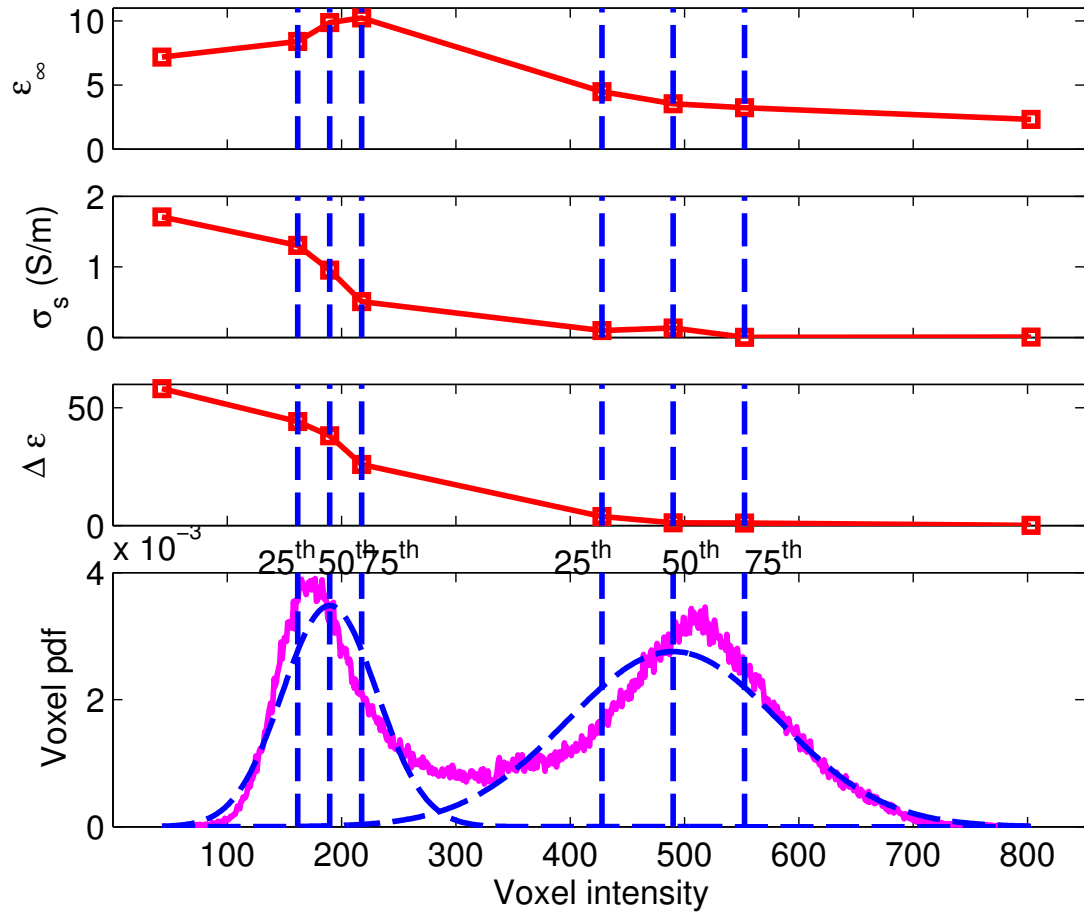


Fig. 4.4 Two-component Gaussian mixture model used to fit the distribution of the voxel intensity of a magnetic resonance image. The 25th, 50th, and 75th percentile of each component are labelled. These critical percentiles determine the boundaries for the piecewise mapping from the voxel intensities to the Debye parameters. Voxel intensities falling within these boundaries are linearly mapped to the Debye parameters. The mapping to ϵ_{∞} , σ_s and $\Delta\epsilon$ are shown in the top three graphs.

The complex relative permittivity can be described by the Debye model, which is

$$\epsilon_r^* = \epsilon_{\infty} + \frac{\Delta\epsilon}{1 + j\omega\tau} + \frac{\sigma_s}{j\omega\epsilon_o} \quad (4.3)$$

where ϵ_{∞} , $\Delta\epsilon$, τ , and σ_s are the tissue-dependent parameters, and ω is the angular frequency. In particular, ϵ_{∞} is the relative permittivity for infinite value of frequency, and $\Delta\epsilon$ is the difference between the infinite and static relative permittivity. τ is the relaxation time

Table 4.1 Estimated Debye parameters valid from 3.1 GHz to 10.6 GHz

		0-30% adipose			85-100% adipose		
		25 th	50 th	75 th	25 th	50 th	75 th
ϵ_∞		8.39	9.87	10.24	4.49	3.52	3.22
σ_s	S/m	1.30	0.95	0.51	0.097	0.133	0.00
$\Delta\epsilon$		44.17	38.1	25.92	3.83	1.19	1.00
τ	ps	10.20	10.94	10.97	16.31	15.67	20

constant and σ_s is the static conductivity. We estimate the Debye parameters of Group I and Group III at the 25th, 50th, and 75th percentile from the data in [84, 86] and allow τ to vary.⁴ The results are listed in Table 4.1. The 25th, 50th, and 75th percentile of the two Gaussian distributions are matched to these parameters. This defines seven intervals to cover the possible values of the voxel intensities. Given the average voxel intensity of a solid $\hat{f}_T(i)$, we identify the interval it belongs to and use a linear function to find its Debye parameters.

4.2 An Example

Fig. 4.5 demonstrates the relation between $\hat{L}(T)$ and the number of solids generated to fill the tissue region, with α being marked on the side. As α gets smaller, \hat{L} decreases and the number of solids increases. When $\alpha = 0$, $\hat{L}(T) = 0$ and the number of solids is at its maximum. This presents the case of a perfect match. Fig. 4.6 shows the three-dimensional breast models, in which the tissue region is filled with 90 solids and 534 solids, when $\alpha = 4 \times 10^6$ and $\alpha = 5 \times 10^5$. We stitch the segmented skin with a 1.5 mm slab, which is backed by a 3-mm slab to represent adipose and a 5-mm slab to represent the muscle. Fig. 4.7 shows the isotropic view of the final breast model. Fig. 4.8 shows the distribution of the relative permittivity and effective conductivity, when the voxel intensities in the tissue region are perfectly matched by a regression tree and approximated by a regression tree with 1177 solids as $\alpha = 2 \times 10^5$.

⁴In the work of [147], τ is assumed to be a constant 10 ps. Our simulations show that keeping τ constant or not yields negligible difference in the calculated electric field.

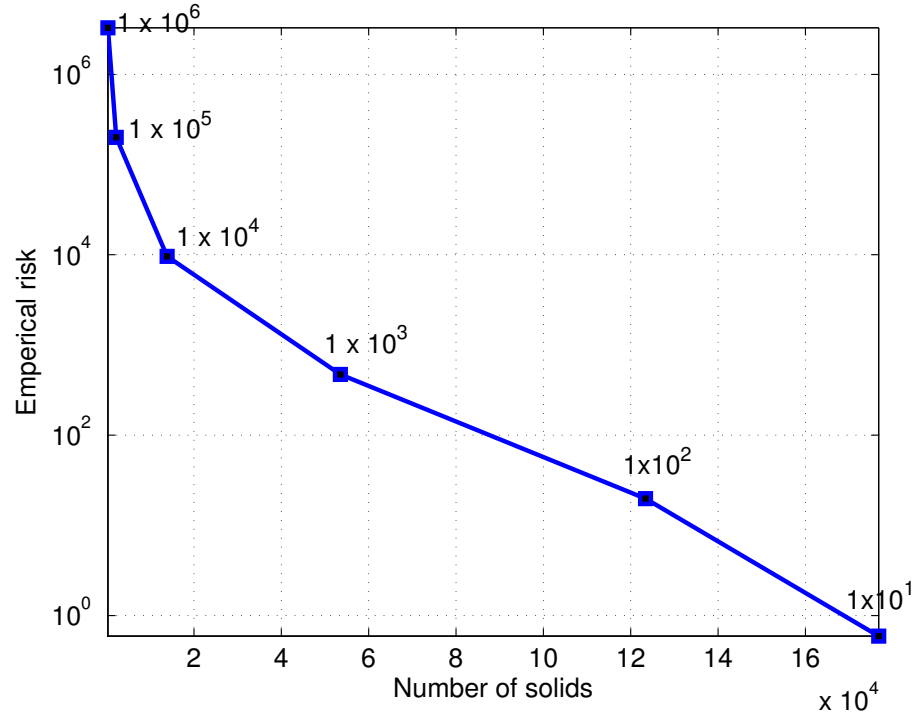


Fig. 4.5 Relation between the empirical risk and the number of leaf nodes in the regression tree. Each point on the trace corresponds to a pruned tree. The label next to each point is the value of the complexity penalty. When the empirical risk is 0 and the complexity penalty is 0, the number of leaf nodes is 205,190 in this example.

4.3 Comparison of the Dielectric and Debye Model

Both the dielectric model and the Debye model have been used to describe the breast tissue in the literature. The dielectric properties of breast tissue can be described by the model, which is

$$\epsilon_r^* = \epsilon_r + \frac{\sigma_e}{j\omega\epsilon_o} ,$$

where ϵ_r is the real part of the complex relative permittivity, and σ_e denotes the effective conductivity. The attenuation per unit length in a dielectric medium is

$$20(\log_{10} e) \left(\frac{\omega \Im\{\sqrt{\epsilon_r^*}\}}{c_o} \right) , \quad (4.4)$$

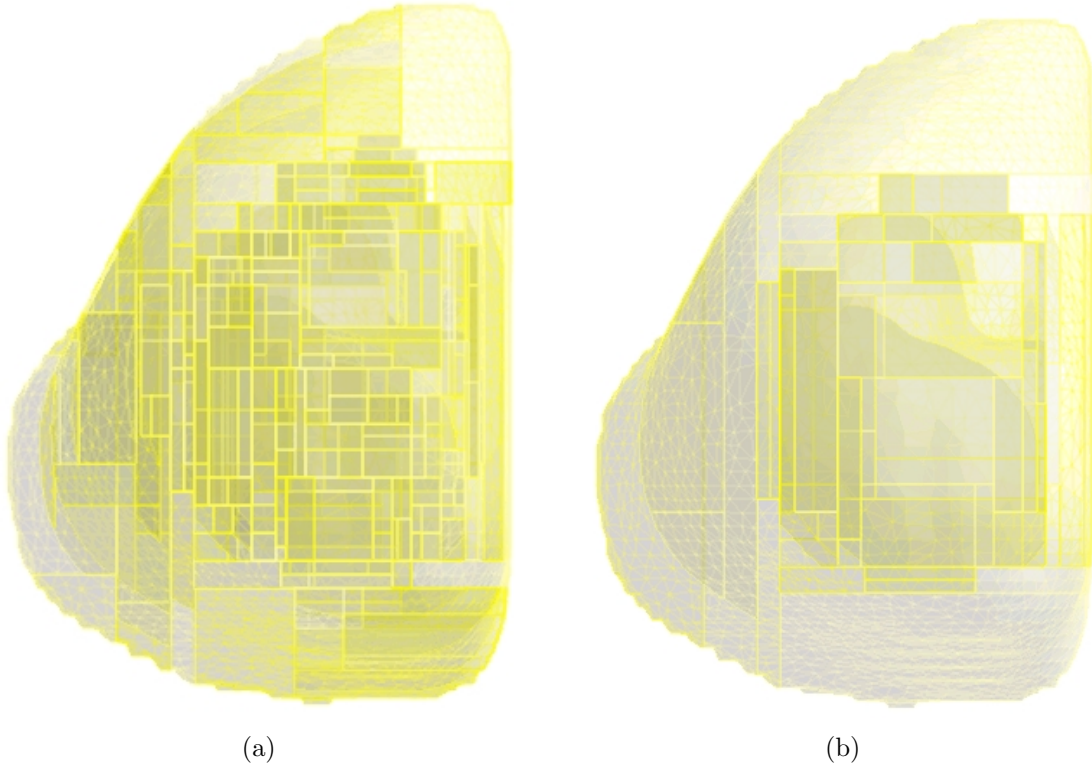


Fig. 4.6 Breast tissue filled with (a) 534 solids when the complexity penalty is 5×10^5 , and (b) 90 solids when the complexity penalty is 4×10^6 .

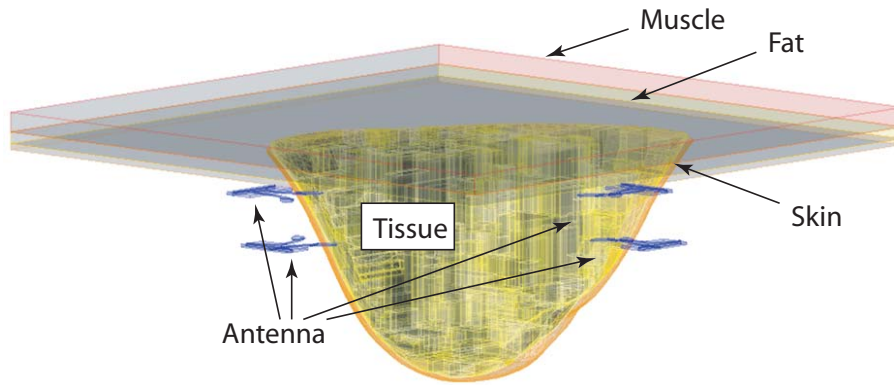


Fig. 4.7 Screen shot of a breast model inside SEMCAD. The top layer is 5-mm thick muscle, followed by 3-mm thick fat. The tissue is filled with a set of solids identified through the regression analysis. The skin layer around the tissue is obtained by manually segmenting the magnetic resonance images. The average skin thickness is 1.5 mm.

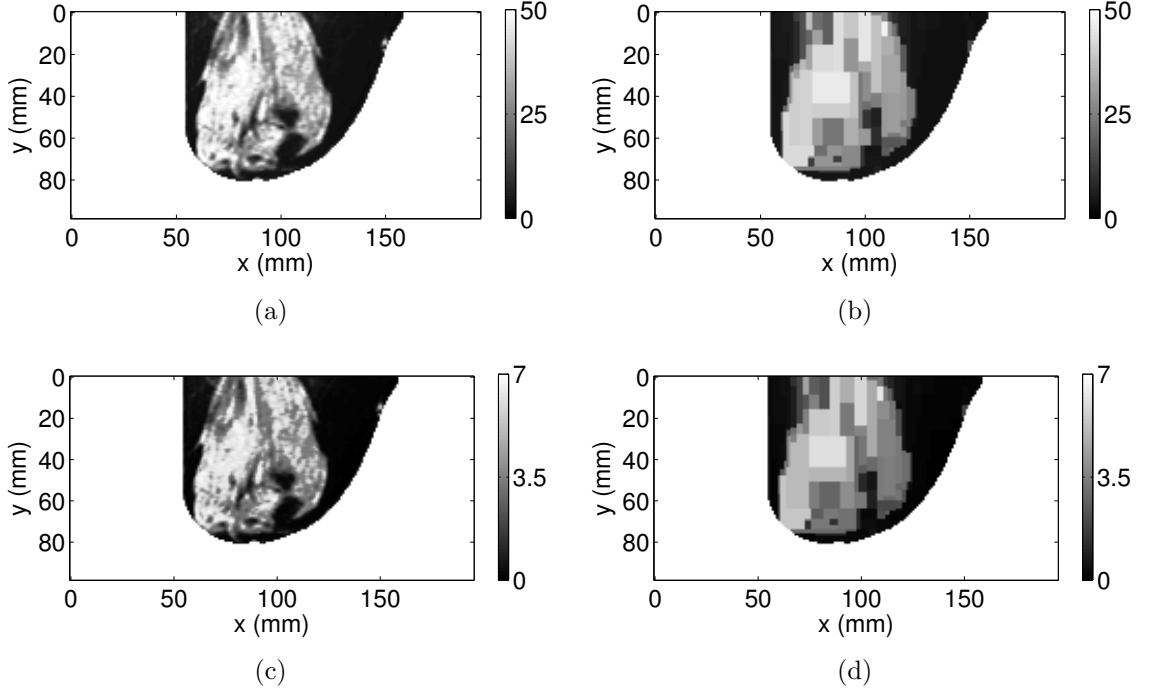


Fig. 4.8 Sagittal cross section showing the dielectric properties obtained by evaluating the Debye model at 6 GHz. (a) and (c) show the relative permittivity and conductivity mapped directly from a magnetic resonance image, voxel-by-voxel. (b) and (d) show the relative permittivity and conductivity when we fill the tissue with 1177 solids.

where $\Im\{\cdot\}$ denotes the imaginary part of the argument. The frequency range of interest in microwave radar is from 1 GHz to 15 GHz. Given the fact that ϵ_r lies in the range from 1 to 60 and σ_e lies in the range from 0 S/m to 25 S/m in this frequency range, and $\epsilon_o = 8.85 \times 10^{-12}$ F/m, we have $\frac{\sigma_e}{\omega \epsilon_o \epsilon_r} > 1$. We derived the lower bound on the attenuation in (4.4) using the Taylor series expansion, which is

$$20(\log_{10} e) \left(-\frac{\mu_o}{2\epsilon_o} \frac{\sigma_e}{\sqrt{\epsilon_r}} \right) . \quad (4.5)$$

Similarly, given τ is on the scale of tens of pico-seconds, we have $1 + \omega^2 \tau^2 \approx 1$. We derived The lower bound on the attenuation associated with the Debye model in (4.3), which is

$$20(\log_{10} e) \left(\frac{-1}{2c_o} \frac{\omega^2 \tau \Delta \epsilon + \sigma_s / \epsilon_o}{\sqrt{\epsilon_\infty + \Delta \epsilon}} \right) . \quad (4.6)$$

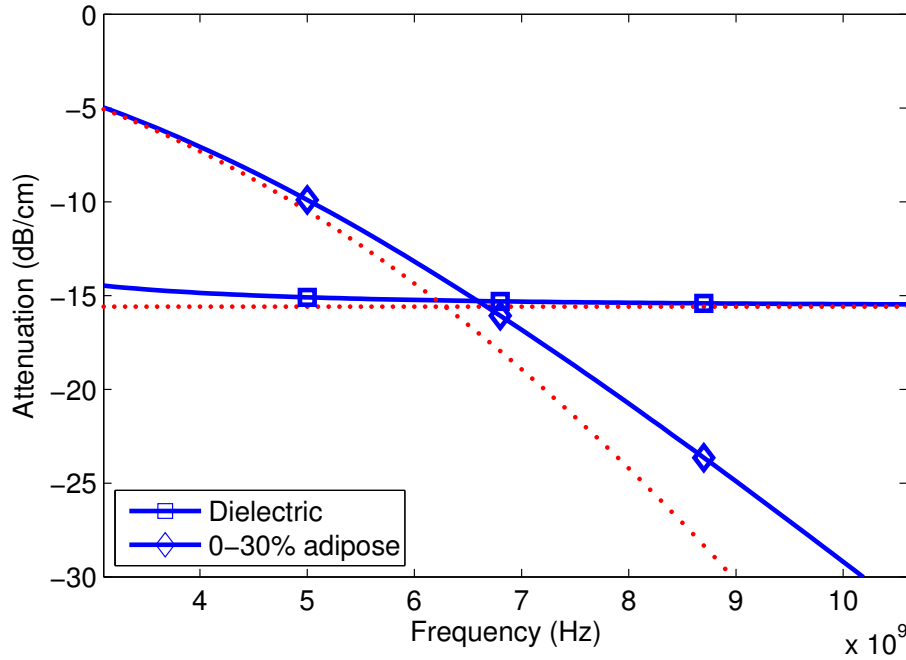


Fig. 4.9 Attenuation of the tissue containing 0-30% adipose and the lower bound. The dielectric material is specified at a relative permittivity of 41 and a conductivity of 6.5 S/m.

Comparing (4.5) and (4.6), we notice that the attenuation in the medium is frequency-independent, while the attenuation in the Debye medium varies quadratically as the frequency increases. Fig. 4.9 shows the attenuation inside the tissue containing 0-30% adipose described by the Debye model and inside the medium with a relative permittivity of 41 and an effective conductivity of 6.5 S/m. Their respective bounds are also shown. There is more attenuation in the higher frequency range associated with the Debye model.

We have performed a simulation on a breast model surrounded by four antennas proposed in [67], which offer wideband performance between 3 and 30 GHz. This is shown in Fig. 4.10. A Gaussian-modulated sinusoid with a bandwidth of 7.5 GHz centred at 6.85 GHz is fed to Antenna A and Antenna C receives the signal. Fig. 4.11 demonstrates the disparity in the received signals, when the breast tissue is modelled as a Debye medium and as a dielectric medium, whose parameters are obtained by evaluating the Debye model at the centre frequency to represent an average. As shown in Fig. 4.11(a), the Debye model offers more attenuation in the high frequency range than the dielectric model. Since the high-frequency components are those responsible for resolving small tumors, this compar-

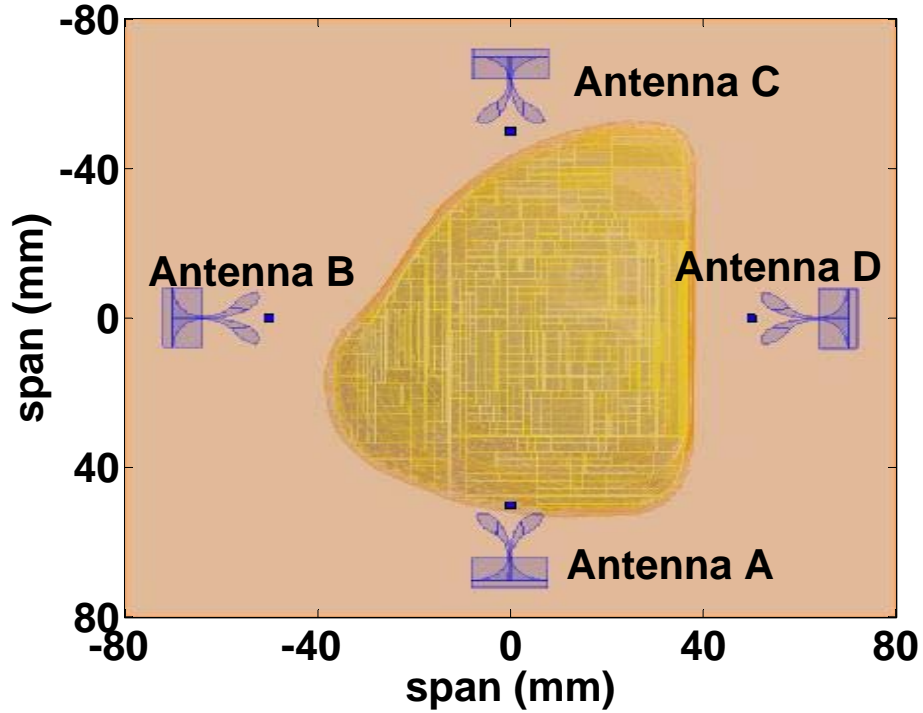
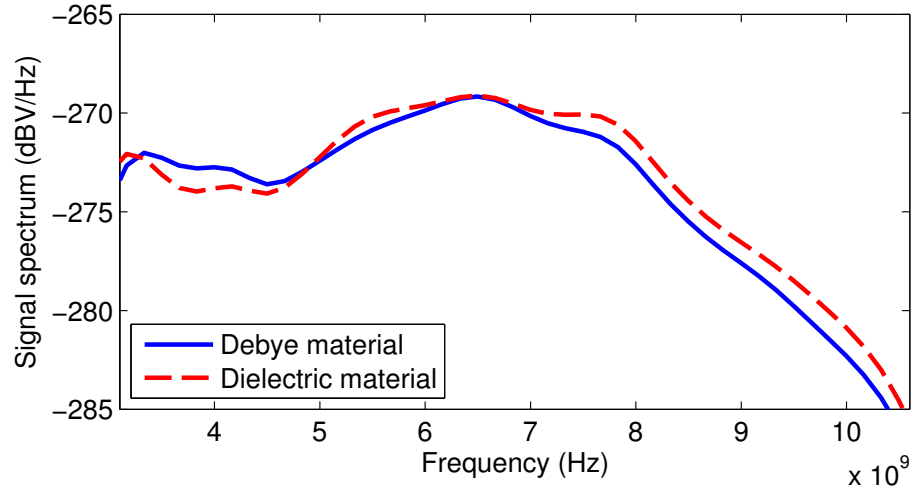


Fig. 4.10 Top view of the simulation scenario. The breast is surrounded by four antennas positioned 20 mm below the skin layer and at $(0, -70 \text{ mm})$, $(-70 \text{ mm}, 0)$, $(0, 70 \text{ mm})$ and $(70 \text{ mm}, 0)$.

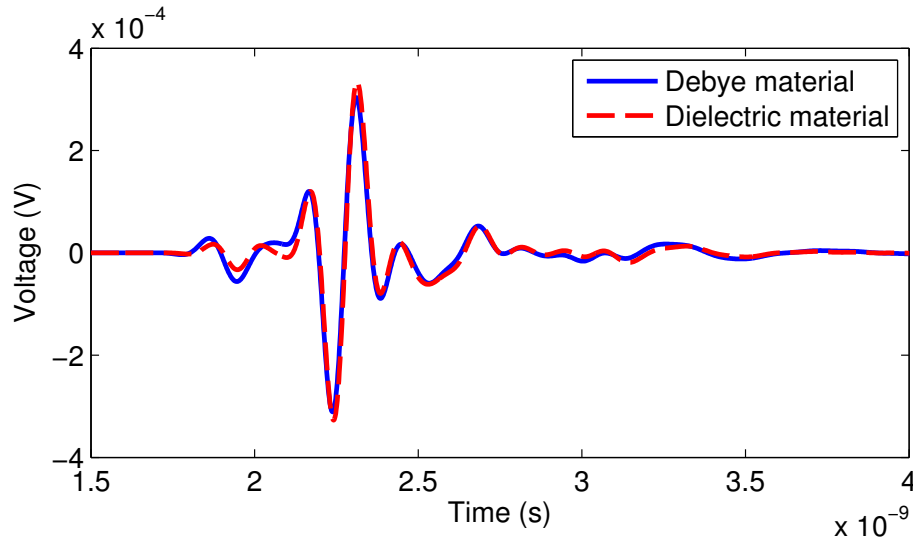
ison confirms the need to use the Debye model to describe the dielectric properties of the breast tissue. Fig. 4.11(b) shows the time-domain signals.

4.4 Conclusions

In this this chapter, we have presented a method to build numerical breast models from magnetic resonance images. The models retain the heterogeneous features of the tissue structure, but minimize the structural complexity by clustering larger lumps of similar tissue. This is controlled by a user-selected factor. Such models can be created in commercial software and integrated with complex antennas to perform full-wave electromagnetic simulations. In addition, we studied the effect of using the dielectric model and the Debye model to characterize the breast tissue. Through the lower bound on the attenuation and numerical simulations, we confirm that using the Debye model is critical to adequately represent the lossy nature of breast tissue in the high frequency range.



(a)



(b)

Fig. 4.11 Received signals at Antenna C with dielectric and Debye materials in the tissue region (a) frequency-domain signals and (b) time-domain signals.

Chapter 5

Comparison of Image Quality of Microwave Radar and Microwave-Induced Thermoacoustics

Research has shown that the alterations in vascularity, cellularity, and stromal characteristics in breast malignancy are uniquely correlated with the changes in water content and ionic molecules [113]. This leads to localized changes in permittivity and conductivity at microwave frequencies, which signify higher reflection and absorption of microwave energy. Microwave radar techniques exploiting the scattered energy and microwave-induced thermoacoustic techniques exploiting the absorbed energy, can produce images carrying diagnostic information about breast malignancy. They are referred to as the radar and thermoacoustic techniques respectively in the following text.

Images from the radar techniques are the scattered energy as a function of the two-dimensional space. Several algorithms have been proposed for breast imaging using these techniques. Most noticeable algorithms include: the delay-and-sum (DAS) algorithm [89]; the time-reversal algorithm [75, 76]; the space-time beamforming algorithms formulated in the time domain [10] and frequency domain [26]; the robust capon beamforming algorithm [139]; the delay-multiply-and-sum algorithm [91].

The pixel intensity in a thermoacoustic image represents the heat absorption at the point. The DAS algorithm [55, 40], the time-reversal algorithm [144], the filtered back projection algorithm [77], and the robust adaptive method [138], have been proposed for

these techniques being applied in breast imaging.

The breast tissue is considered frequency dispersive, spatially heterogeneous, and acoustically homogeneous. The quality of images produced by the radar and thermoacoustic techniques, particularly in the presence of tissue heterogeneity deserves more research. The objective of this chapter is to estimate and compare the image quality promised by the radar and thermoacoustic techniques in the context of breast imaging.

The finite-difference time-domain (FDTD) method was implemented to numerically solve the Maxwell equations and the linear acoustic equations involving homogeneous and heterogeneous breast models. It generated the radar and thermoacoustic signals. The DAS algorithm was chosen as a common scheme for its simplicity and robustness, and implemented for both signals to generate breast images.

We found that both the radar and thermoacoustic techniques are capable of imaging a dielectric inclusion in a homogeneous medium and they suffer from the decrease in the inclusion size and the dielectric contrast, which are qualified through the localization error and the cross-image signal-to-clutter ratio (SCR). Then, two inclusions were placed closely in a homogeneous medium at two levels of dielectric contrast. They were not resolved in the radar image when the dielectric contrast was high, but resolved in the radar image when the dielectric contrast was low. This was attributed to the reduced wavelength in the high-permittivity medium, potentially increasing the spatial resolution of the images. The two inclusions were resolved in the thermoacoustic images at both levels of dielectric contrast. Finally, we tested the image algorithm on the signals generated from a heterogeneous breast model built from a magnetic resonance image. Thermoacoustic images were able to reveal the spatial details correlated with the heterogeneity of tissue. Due to the strong frequency dispersion and tissue inhomogeneity, the radar image could not provide any useful information on the structure of the tissue.

The result of this chapter supports the utility of the thermoacoustic techniques for imaging the breast, especially in the presence of heterogeneity. Further investigation of the hardware requirement of these techniques is warranted.

This chapter is structured as follows. Section 5.1 describes the physics associated with the radar and thermoacoustic phenomenon. Section 5.2 summarizes the dielectric, thermal, and acoustic properties of malignant and healthy tissue pertinent to this study. Section 5.3 presents the FDTD method to solve the Maxwell equations and linear acoustic equations. Section 5.4 shows that the amplitude of thermoacoustic signals is proportional

to the conductivity-heat capacity ratio. Section 5.5 presents the DAS algorithm adapted for radar and thermoacoustic signals, which is followed by Section 5.6 that discusses the imaging results. Section 5.7 concludes this chapter.

5.1 Physics of Microwave Radar and Microwave-Induced Thermoacoustics

The radar techniques use a pico-second pulse to probe the breast. The wideband nature of this pulse permits to resolve small scatterers in space, such as breast tumors embedded in healthy tissue. This is illustrated in Fig. 5.1(a) and a typical wideband pulse is shown in Fig. 5.1(b). The propagation of this pulsed field is governed by the Maxwell equations, which are

$$\frac{\partial \vec{H}}{\partial t} = -\frac{1}{\mu} \nabla \times \vec{E} , \quad (5.1a)$$

$$\frac{\partial \vec{E}}{\partial t} = \frac{1}{\epsilon} (\nabla \times \vec{H} - \vec{J}) , \quad (5.1b)$$

where \vec{E} and \vec{H} denote the electric and magnetic field vectors. ϵ and μ denote the electric permittivity and magnetic permeability. \vec{J} denotes the current density, and t denotes time. Eq. (5.1) can be collapsed into the wave equation in a homogeneous medium, which is

$$\nabla^2 \vec{E} - \mu\epsilon \frac{\partial^2}{\partial t^2} \vec{E} = \mu \frac{\partial}{\partial t} \vec{J} . \quad (5.2)$$

To excite the thermoacoustic process in the breast, a pulse-modulated continuous microwave is radiated towards the chest wall as shown in Fig. 5.2(a).¹ The envelope of the modulating signal is 1- μ s wide, which is shown in Fig. 5.2(b). The carrier microwave is responsible for creating a uniform electromagnetic field in the tissue. The envelope determines the bandwidth of the thermoacoustic signal.

The amount of the microwave energy deposited in the tissue is quantified by the specific

¹Continuous-wave modulated thermoacoustic system is discussed in [144], which is more commonly discussed in photoacoustics [6].

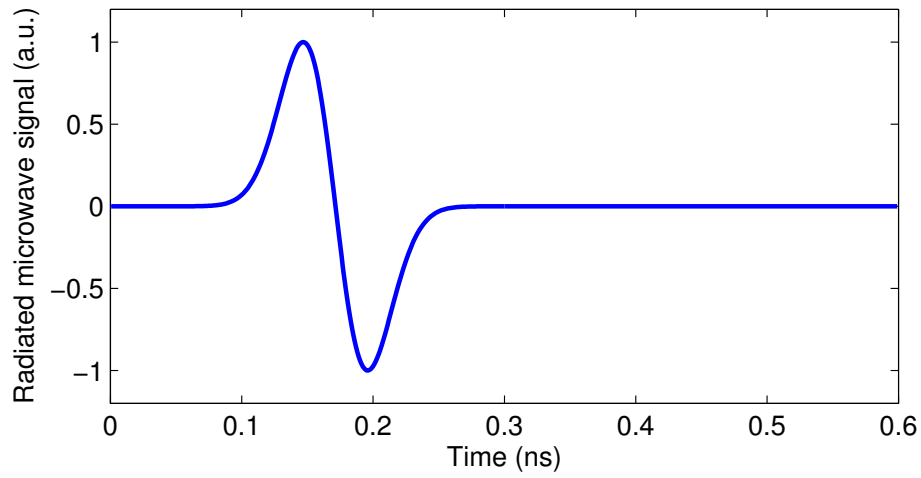
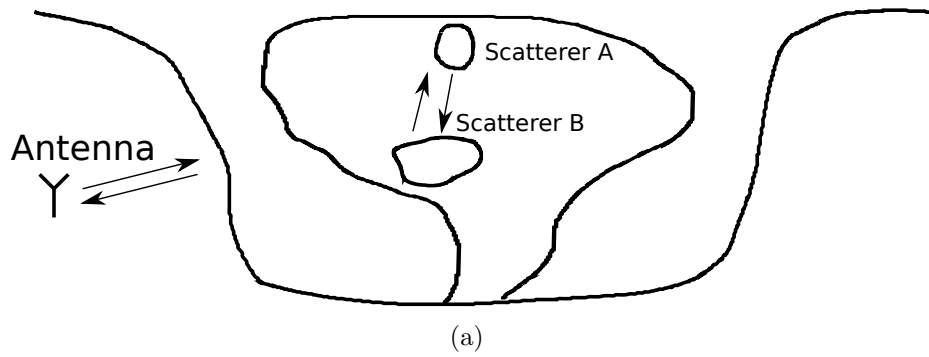


Fig. 5.1 (a) Illustration of the microwave radar technique. An antenna radiates a wideband pulse towards the breast. After scattering, the pulse is received by the antenna. The locations of the scatterers are identified from the received signal. (b) A typical microwave pulse with a bandwidth from 3.1 GHz to 10.6 GHz. The half-magnitude width is 0.1 ns.

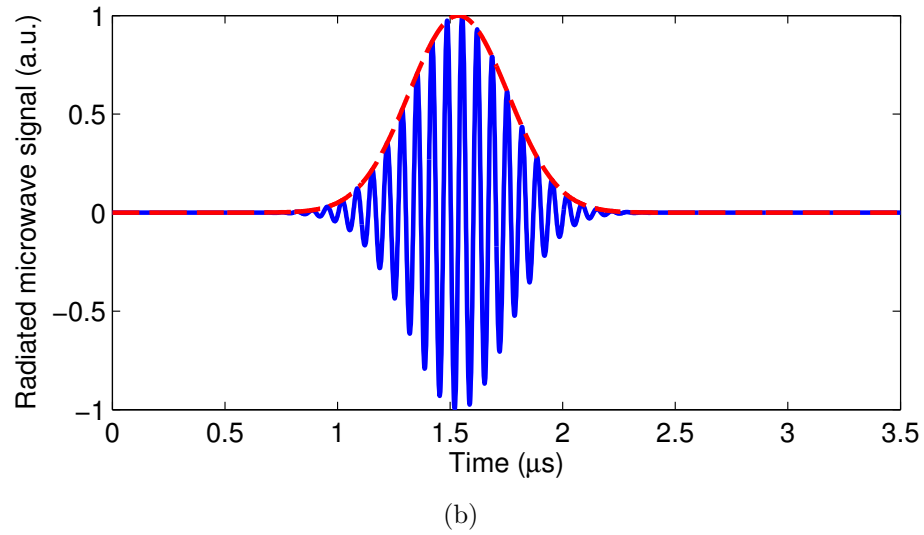
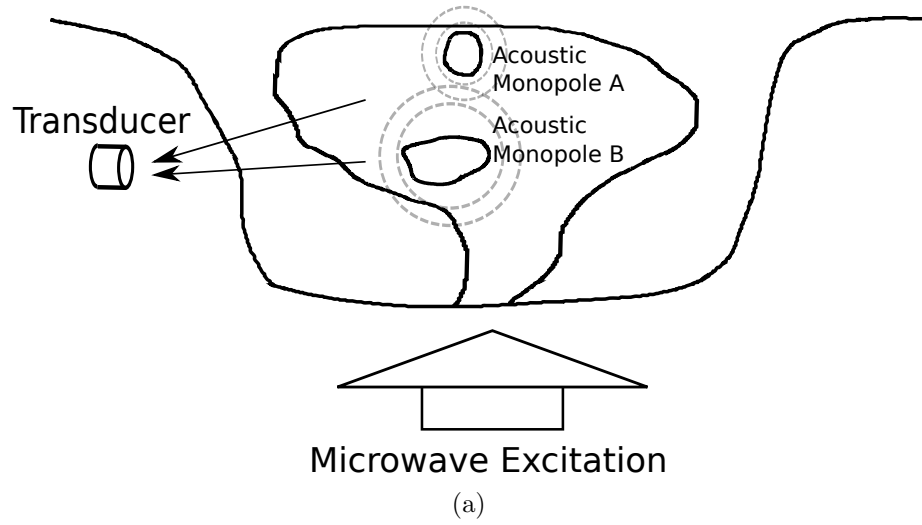


Fig. 5.2 (a) Illustration of the microwave-induced thermoacoustic technique. A uniform field is created inside the breast, and each point becomes a source emitting acoustic signals, which are detected by the transducer. (b) Shape of the Gaussian-modulated continuous wave used to excite the thermoacoustic process. The envelope has a half-magnitude width of 0.5 μs .

absorption rate (SAR) S , which is defined as

$$S = \frac{\sigma_e}{2\rho} |\vec{E}|^2 , \quad (5.3)$$

where ρ is the mass density and σ_e is the effective conductivity. This energy deposition is related to the variation of tissue temperature through the Penne bio-heat equation [112], which is

$$\rho c_p \frac{\partial T}{\partial t} = \nabla \cdot (\kappa \nabla T) + \rho S , \quad (5.4)$$

where c_p and κ denote the heat capacity and thermal conductivity of tissue, respectively, and T is the tissue temperature. To generate the thermoacoustic signal, the sub-microsecond deposition of the microwave energy in the tissue should be brief compared with the diffusion process of temperature. This is known as the condition of *thermal confinement*. Under this condition, the diffusion term $\nabla \cdot (\kappa \nabla T)$ in (5.4) is dropped, and the SAR in (5.3) is decoupled into the product of a space-dependent term $\tilde{S}(\vec{r})$ and a unitless time-dependent term $I(t)$, which represents the envelope of the modulated continuous wave. The Penne bio-heat equation in (5.4) then reduces to

$$c_p \frac{\partial T}{\partial t} = \tilde{S} I . \quad (5.5)$$

When I is positive, energy is transferred from the environment to the system. When I is negative, energy is transferred from the system to the environment. In the thermoacoustic process, I stays as a positive function, corresponding to the tissue absorption of microwave energy from the environment.

In the linear acoustic theory [68],² the mass continuity equation is

$$\frac{\partial p}{\partial t} = -K \nabla \cdot \vec{u} , \quad (5.6)$$

where p and \vec{u} denote the pressure and particle velocity of a fluid, and K is its bulk modulus. The temperature variation in (5.5) contributes to the local increase of mass through the

²An elastic signal can propagate in the form of a transverse wave and/or a longitudinal wave. The propagation of the transverse wave is at a smaller speed and experiences larger attenuation compared with the longitudinal wave in a microwave-heated breast. There is little energy carried away by the transverse wave. Therefore, the breast is assumed to be an ideal fluid in this application, and only the longitudinal wave is analyzed.

volume expansion coefficient α . This adds an excitation term to (5.6), which then becomes

$$\frac{\partial p}{\partial t} = -K \nabla \cdot \vec{u} + \alpha K \frac{\partial T}{\partial t} . \quad (5.7)$$

Another relation between the pressure and particle velocity in the fluid is

$$\frac{\partial \vec{u}}{\partial t} = -\frac{1}{\rho} \nabla p , \quad (5.8)$$

which is known as the simple force equation derived from Newton's second law of motion. The negative sign in (5.8) denotes the fact that the particles flow in the negative direction of the pressure gradient. Combining (5.5), (5.7) and (5.8) leads to the thermoacoustic wave equation in a homogeneous medium

$$\nabla^2 p - \frac{\rho}{K} \frac{\partial^2 p}{\partial t^2} = -\frac{\rho \alpha}{c_p} \frac{\partial}{\partial t} \tilde{S} I . \quad (5.9)$$

Comparing (5.2) and (5.9) reveals that the radiated and scattered microwave radar signals are solutions to the inhomogeneous electromagnetic wave equation and the excitation is the current density. The microwave-induced thermoacoustic signal is a solution to the inhomogeneous wave equation. The temperature variation due to the SAR converts every point in space to a pulsating sphere, which becomes the excitation.

5.2 Endogenous Properties of the Human Breast

The human breast is an intricate mixture of gland, adipose, and blood vessels. The heterogeneity of tissue can be characterized based on the histological content of the samples, i.e. the percentage of adipose [84, 86]. The dispersiveness of tissue is commonly described by the Cole-Cole model, in which the complex relative permittivity is

$$\epsilon_r^* = \epsilon_\infty + \frac{\Delta\epsilon}{1 + (j\omega\tau)^{1-\alpha}} + \frac{\sigma_s}{j\omega\epsilon_o} ,$$

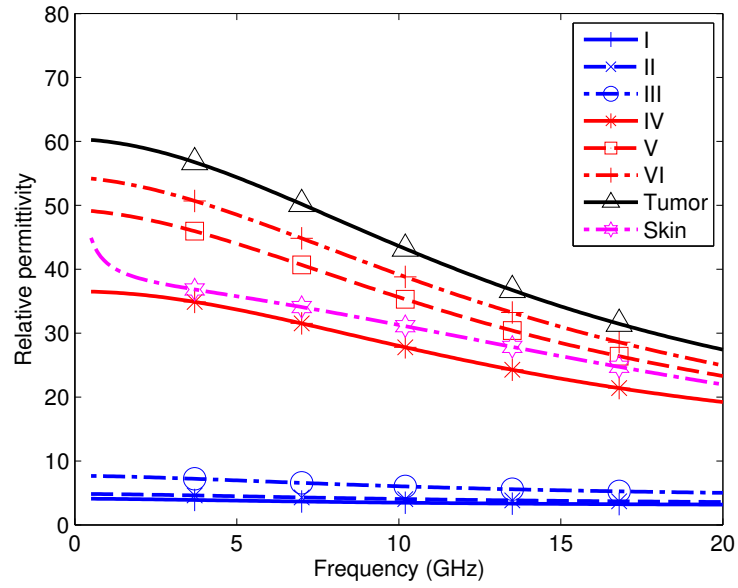
where ϵ_∞ is the relative permittivity for infinite value of frequency, and $\Delta\epsilon$ is the difference between the infinite and static relative permittivity. τ is the relaxation time constant and σ_s is the static conductivity. The value of the parameter α is determined experimentally

Table 5.1 Cole-Cole parameters of the six types of tissue in the order of decreasing adipose content valid from 0.5 GHz to 20 GHz

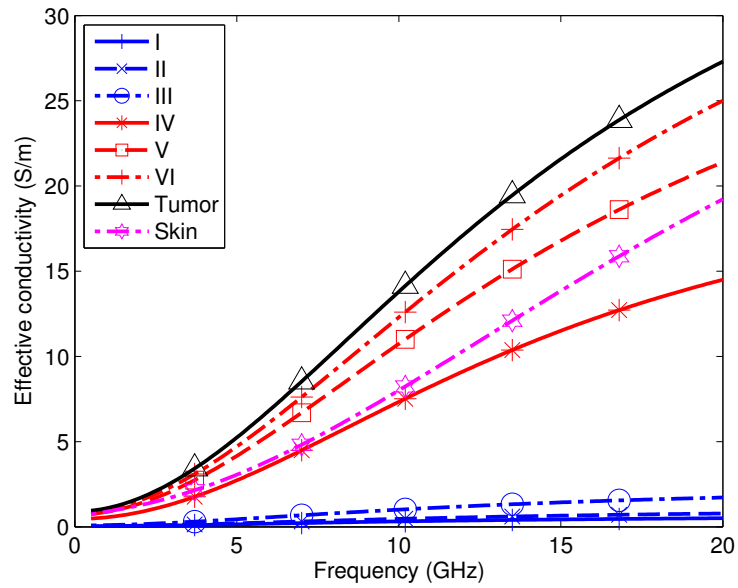
Tissue Type	ϵ_∞	σ_s S/m	$\Delta\epsilon$	τ ps	α
I	2.908	0.020	1.200	16.88	0.069
II	3.140	0.036	1.708	14.65	0.061
III	4.031	0.083	3.654	14.12	0.055
IV	9.941	0.462	26.60	10.90	0.003
V	7.821	0.713	41.48	10.66	0.047
VI	6.151	0.809	48.26	10.26	0.049
Tumor	9.058	0.899	51.31	10.84	0.022
skin	4.0	0.0002	32	7.23	0
	-	-	1100	32480	0.2

as a correction factor. Six typical values of the dielectric properties of tissue are extracted from [147] for this study, which is based on the data in [84, 86]. Their Cole-Cole parameters are listed in Table 5.1 in the order of decreasing adipose content. Their relative permittivity and effective conductivity as a function of frequency are plotted in Fig. 5.3.

The absorption of the microwave energy and conversion to heat in breast tissue are characterized by the volume expansion coefficient α and the heat capacity c_p . The volume expansion coefficient is considered a constant in this study [24]. The heat capacity of the breast tissue varies from 2220 J/(kg K) to 3500 J/(kg K) as the content of adipose decreases [118, 34]. The tissue density, ρ , acoustic speed, c_a , and acoustic attenuation, β , also affect the thermoacoustic signals as they propagate through the tissue. The breast mass density has been reported in the range from 990 kg/m³ to 1060 kg/m³ [31, 118, 96]. The acoustic speed varies from 1478 m/s in adipose tissue to 1613 m/s in glandular tissue [96, 97]. The attenuation of acoustic waves is nonlinear in the frequency range above 20 kHz and has been empirically characterized as a function of frequency in several discrete frequency ranges [31]. Thermoacoustic signals typically occupy the frequency range from 0.5 MHz to 1.5 MHz, lower than the one occupied by medical ultrasound imaging. The acoustic and thermal properties of the breast tissue and skin are compiled from [31, 118, 24, 96, 116, 132, 34] and listed in Table 5.2.



(a)



(b)

Fig. 5.3 Dielectric properties of the six types of tissue, tumor, and skin listed Table 5.1 (a) relative permittivity and (b) effective conductivity.

Table 5.2 Acoustic and thermal properties of the breast tissue, tumor, and skin (f is in MHz.)

	Speed	Density	Attenuation	Heat Capacity	Vol. Expansion Coeff.
	c_a	ρ	β	c_p	α
	m/s	kg/m ³	dB/cm	J/(kg K)	K ⁻¹
Tissue	1478-1613	990-1060	$0.75f^{1.5}$	2220-3500	3×10^{-4}
tumor	1550	1182	$0.57f$	3500	3×10^{-4}
skin	1615	1093-1190	0.35	3680	3×10^{-4}

These laboratory measurements and the mathematical characterization are of fundamental importance in numerical studies of physical systems, as they provide the physical justification on the significance of numerical results. The effect of the dielectric, thermal, and acoustic properties on the radar and thermoacoustics signals is discussed in Section 5.4.

5.3 Numerical Modelling

We use the FDTD method to solve the Maxwell equations in (5.1a) and (5.1b), and the acoustic equations in (5.7) and (5.8). This choice of a numerical method is driven by two factors: (a) the rectangular grid easily incorporates the heterogeneity of breast tissue; (b) we are interested in the time-domain signals generated in the systems.³ This section summarizes the key elements of the FDTD method needed to simulate the two processes.

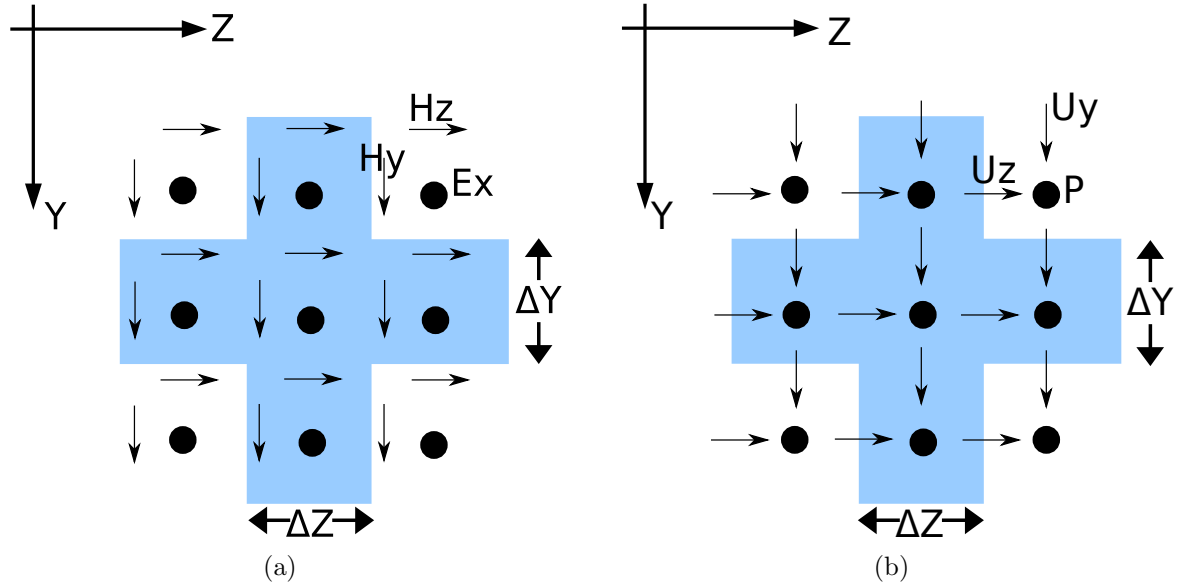


Fig. 5.4 Yee cell for the (a) electromagnetic and (b) acoustic FDTD simulations.

5.3.1 Duality in Electromagnetic and Acoustic Wave Equations

The Maxwell equations (5.1a) and (5.1b) can be written in the two-dimensional form for the transverse magnetic mode polarized in the x direction as

$$\frac{\partial}{\partial t} \begin{bmatrix} 0 \\ H_y \\ H_z \end{bmatrix} = -\frac{1}{\mu} \begin{bmatrix} 0 & -\frac{\partial}{\partial z} & \frac{\partial}{\partial y} \\ \frac{\partial}{\partial z} & 0 & -\frac{\partial}{\partial x} \\ -\frac{\partial}{\partial y} & \frac{\partial}{\partial x} & 0 \end{bmatrix} \begin{bmatrix} E_x \\ 0 \\ 0 \end{bmatrix}, \quad (5.10a)$$

$$\frac{\partial}{\partial t} \begin{bmatrix} E_x \\ 0 \\ 0 \end{bmatrix} = \frac{1}{\epsilon} \begin{bmatrix} 0 & -\frac{\partial}{\partial z} & \frac{\partial}{\partial y} \\ \frac{\partial}{\partial z} & 0 & -\frac{\partial}{\partial x} \\ -\frac{\partial}{\partial y} & \frac{\partial}{\partial x} & 0 \end{bmatrix} \begin{bmatrix} 0 \\ H_y \\ H_z \end{bmatrix}. \quad (5.10b)$$

³The Green's function method [69] and the pseudo-spectrum time-domain method [18] have also been applied to simulate the thermoacoustic process. It should be noted that the Green's function method assumes an acoustically homogeneous medium. The pseudo-spectrum time-domain method has the advantage to reduce the spatial discretization to two points per wavelength. However, fast spatial variation of the acoustic properties may incur Gibb's phenomenon [144].

After applying the central finite-difference discretization in space and time, we obtain the following equations

$$H_y|_{j,k-\frac{1}{2}}^{n+\frac{1}{2}} = -\frac{\Delta t}{\mu\Delta z} (E_x|_{j,k}^n - E_x|_{j,k-1}^n) + H_y|_{j,k-\frac{1}{2}}^{n-\frac{1}{2}}, \quad (5.11a)$$

$$H_z|_{j-\frac{1}{2},k}^{n+\frac{1}{2}} = -\frac{\Delta t}{\mu\Delta y} (E_x|_{j,k}^n - E_x|_{j-1,k}^n) + H_z|_{j-\frac{1}{2},k}^{n-\frac{1}{2}}, \quad (5.11b)$$

$$E_x|_{j,k}^n = -\frac{\Delta t}{\epsilon\Delta z} (H_y|_{j,k+\frac{1}{2}}^{n-\frac{1}{2}} - H_y|_{j,k-\frac{1}{2}}^{n-\frac{1}{2}}) + \frac{\Delta t}{\epsilon\Delta y} (H_z|_{j+\frac{1}{2},k}^{n-\frac{1}{2}} - H_z|_{j-\frac{1}{2},k}^{n-\frac{1}{2}}) + E_x|_{j,k}^{n-1}. \quad (5.11c)$$

In the above three equations, the superscript $(\cdot)^n$ means “at the time $t = n(\Delta t)$ ” and the subscript $(\cdot)_{j,k}$ means “at the position $y = j(\Delta y)$ and $z = k(\Delta z)$ ”. The $\frac{1}{2}$ offset in both space and time is to indicate the staggering nature of the Yee cells [145]. The naming convention of a Yee cell containing the electromagnetic field quantities is shown in Fig. 5.4(a)

The acoustic equations (5.7) and (5.8) are intentionally written in the form to reveal duality with the Maxwell equations (5.1a) and (5.1b). The dual quantities can be identified by comparing these equations term by term. It should be noted that u_y and u_z are swapped in space as opposed to H_y and H_z . Equivalently, this swapping introduces a permutation matrix to the acoustic equations⁴, which now become

$$\frac{\partial}{\partial t} \begin{bmatrix} 0 & 0 & 0 \\ 0 & 0 & 1 \\ 0 & -1 & 0 \end{bmatrix} \begin{bmatrix} 0 \\ u_y \\ u_z \end{bmatrix} = -\frac{1}{\rho} \nabla \times \begin{bmatrix} p \\ 0 \\ 0 \end{bmatrix}, \quad (5.12a)$$

$$\frac{\partial}{\partial t} \begin{bmatrix} p \\ 0 \\ 0 \end{bmatrix} = -K \nabla \times \begin{bmatrix} 0 & 0 & 0 \\ 0 & 0 & 1 \\ 0 & -1 & 0 \end{bmatrix} \begin{bmatrix} 0 \\ u_y \\ u_z \end{bmatrix}. \quad (5.12b)$$

We conclude that the equations in (5.11) for the electromagnetic simulation can be equally applied to the acoustic simulation with a change of variables and signs by the duality principle.

⁴Electromagnetic waves are transverse waves and acoustic waves are longitudinal waves.

5.3.2 Material Modelling

The approximation of the Cole-Cole model by a Debye model valid in the frequency range from 3.1 GHz to 10.6 GHz is made in [147]. The Debye model is implemented using the auxiliary differential equation method [130, ch. 9], which introduces an intermediate variable, the polarization current density, J_p , defined as

$$J_p = \frac{j\omega\Delta\epsilon}{1 + j\omega\tau}\epsilon_o E , \quad (5.13)$$

where the bold-face letters denote the time-harmonic quantities. The time-harmonic form of (5.13) can be converted to the time domain. After applying the central finite-difference discretization in space and time, $J_{p,x}$ becomes

$$J_{p,x}|_{j,k}^{n+\frac{1}{2}} = \epsilon_o \frac{2\Delta\epsilon}{\Delta t + 2\tau} \left(E_x|_{j,k}^{n+\frac{1}{2}} - E_x|_{j,k}^{n-\frac{1}{2}} \right) - \frac{\Delta t - 2\tau}{\Delta t + 2\tau} J_{p,x}|_{j,k}^{n-\frac{1}{2}} . \quad (5.14)$$

The Ampere law in a Debye material is

$$-\frac{\partial H_y}{\partial z} + \frac{\partial H_z}{\partial y} = \epsilon_o \epsilon_\infty \frac{\partial E_x}{\partial t} + \sigma \frac{\partial E_x}{\partial t} + J_{p,x} ,$$

which, after the discretization, becomes

$$\begin{aligned} & -\frac{1}{\Delta y} \left(H_z|_{j+\frac{1}{2},k}^n - H_z|_{j-\frac{1}{2},k}^n \right) + \frac{1}{\Delta z} \left(H_y|_{j,k+\frac{1}{2}}^n - H_y|_{j,k-\frac{1}{2}}^n \right) = \\ & \frac{\epsilon_o \epsilon_\infty}{\Delta t} \left(E_x|_{j,k}^{n+\frac{1}{2}} - E_x|_{j,k}^{n-\frac{1}{2}} \right) + \frac{\sigma_s}{2} \left(E_x|_{j,k}^{n+\frac{1}{2}} + E_x|_{j,k}^{n-\frac{1}{2}} \right) + \frac{4\tau}{2\tau + \Delta t} J_{p,x}|_{j,k}^{n-\frac{1}{2}} \\ & + \frac{\epsilon_o \Delta\epsilon}{2\tau + \Delta t} \left(E_x|_{j,k}^{n+\frac{1}{2}} - E_x|_{j,k}^{n-\frac{1}{2}} \right) . \end{aligned} \quad (5.15)$$

The FDTD method calculates $E_x|_{j,k}^{n+\frac{1}{2}}$ from (5.15), then $J_p|_{j,k}^{n+\frac{1}{2}}$ from (5.14).

The linear acoustic attenuation is applicable in the frequency range of the thermoacoustic signals [44]. Thus, the quantity ‘‘acoustic conductivity’’ σ_a is introduced to form a dual with the electric conductivity and is related to the acoustic attenuation through

$$\beta = 20 \log_{10} \left| e^{j\omega\sqrt{\rho/K}\sqrt{1+\sigma_a K/j\omega}} \right| . \quad (5.16)$$

To determine the frequency at which we evaluate (5.16) for the acoustic conductivity, we

assume a point source with the envelope I is excited at some location \vec{r}_0 . The Green's function to (5.9) in the infinite space is

$$\int_0^t \int_{\Omega} \frac{\rho\alpha}{4\pi c_p} \tilde{S}(\vec{r}') \frac{d}{dt'} I(t') g(\vec{r}, t | \vec{r}', t') d\vec{r}' dt' , \quad (5.17)$$

where $g(\vec{r}, t | \vec{r}', t')$ denotes the Green's function, and Ω denotes the spatial domain of integration. The pressure due to a point source at \vec{r}_0 is

$$\int_0^t \int_{\Omega} \frac{\rho\alpha}{4\pi c_p} \delta(\vec{r}' - \vec{r}_0) \frac{d}{dt'} I(t') g(\vec{r}, t | \vec{r}', t') d\vec{r}' dt' , \quad (5.18)$$

where δ denotes the Dirac delta function. Given the Green's function to the two-dimensional wave equation, which is

$$g(\vec{r}, t | \vec{r}', t') = \frac{2c_a}{\sqrt{c_a^2(t - t')^2 - |\vec{r} - \vec{r}'|^2}} , \quad (5.19)$$

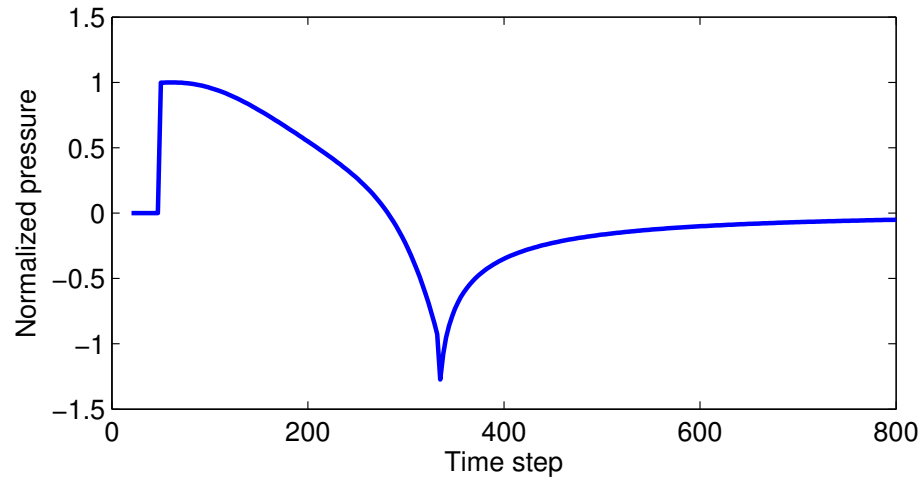
Eq. (5.18) becomes

$$\frac{\rho\alpha}{4\pi c_p} \frac{d}{dt} I \otimes \frac{2}{t} , \quad (5.20)$$

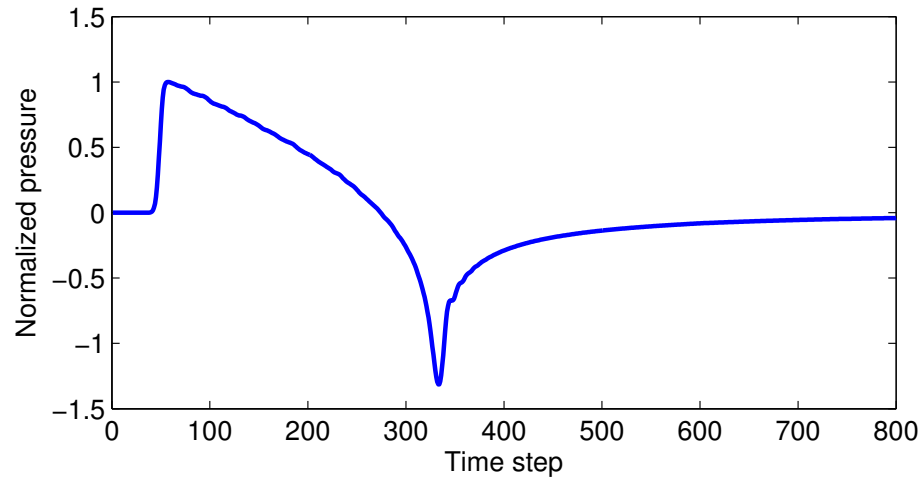
where \otimes denotes the temporal convolution. The Fourier transform of (5.20) gives the spectral content of the signal generated by the point source. We take its peak frequency and use Table 5.2 to calculate the attenuation, which is then substituted to (5.16) for the acoustic conductivity via the Secant method.

5.3.3 Thermoacoustic Wave of a Uniformly-Heated Cylinder

To verify the implementation of (5.12), we compare the FDTD result with the Green's function of a uniformly-excited cylinder. The uniformly-excited cylinder is assumed acoustically homogeneous and heated by an impulse, i.e. $I = \delta(t)$. The thermoacoustic wave radially propagates away from the cylinder. The direct substitution in (5.9) involves a time derivative of the envelope, which causes difficulty in the numerical implementation. The acoustic velocity potential, Φ , is related to the particle velocity through $\nabla\Phi = \vec{u}$ [29].



(a)



(b)

Fig. 5.5 Thermoacoustic signal generated from a uniformly heated cylinder, (a) numerical evaluation of the Green function solution and (b) the FDTD result.

Substituting Φ to (5.8) leads to

$$\nabla^2 \Phi - \frac{\rho}{K} \frac{\partial^2 \Phi}{\partial t^2} = \frac{\alpha}{c_p} \tilde{S} I . \quad (5.21)$$

This change of variable from p in (5.9) to Φ removes the time derivative. The Green's function solution to (5.21) is

$$\int_0^t \int_{\Omega} \frac{\alpha}{4\pi c_p} S(\vec{r}') I(t') g(\vec{r}, t | \vec{r}', t') d\vec{r}' dt' , \quad (5.22)$$

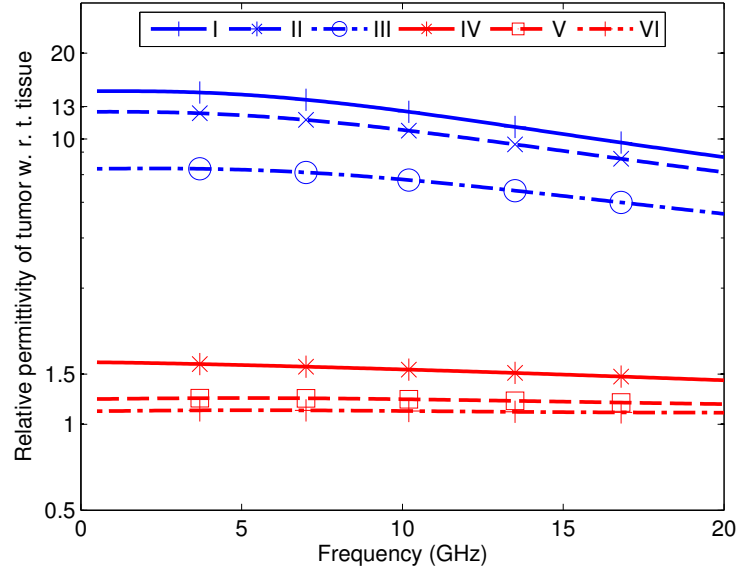
and the pressure is related to the velocity potential through

$$p = -\rho \frac{\partial \Phi}{\partial t} . \quad (5.23)$$

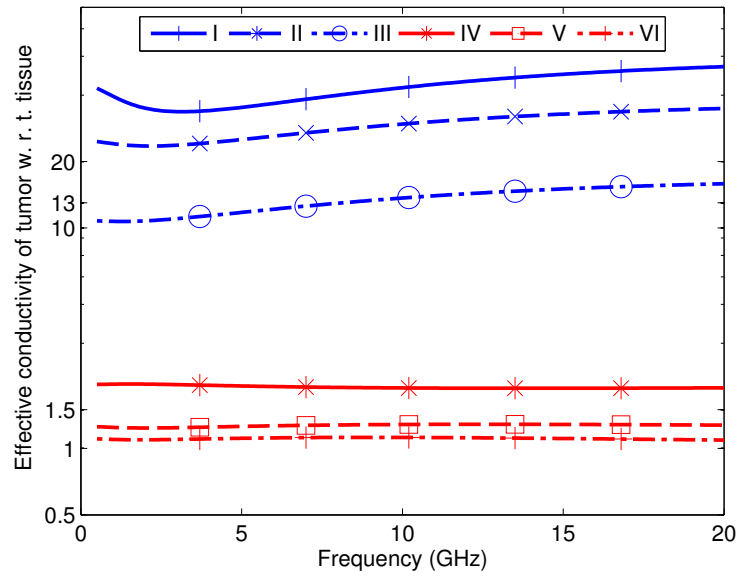
Fig. 5.5(a) shows the result of the numerical evaluation of the integral in (5.22) followed by (5.23), and Fig. 5.5(b) shows the result obtained from the FDTD method. The N-shape thermoacoustic signal is due to the simultaneous heating in the cylindrical region that generates an inward propagating wave and an outward propagating wave [109]. Since the envelope I cannot be an exact Dirac delta function in the FDTD method, a Gaussian pulse is used as the envelope to mimic the pulse. This approximation causes the slight deviation in the result obtained from the FDTD method.

5.4 Comparison of Signals

There are six factors identified that affect the quality of a medical image. They are resolution, contrast, noise, artifacts, distortion, and accuracy [116, ch. 3]. Among them, resolution and contrast are of the most importance. One way to estimate the achievable image resolution in pulse-based imaging techniques is one half of the wavelength evaluated at the central frequency. The central frequency should be high for a good resolution, but limited by the increasing attenuation. The choice of the excitation signal presented in Fig. 5.2(b) is a reflection of this compromise. The central frequency of the derivative of the signal envelope shown in Fig. 5.2(b) is 0.714 MHz. Given an average acoustic speed of 1500 m/s, the acoustic half wavelength is 1.05 mm. The relative permittivity of tissue varies from 4 to 55 at 6.85 GHz, and the half wavelength varies from 3.1 mm to 10.9 mm re-



(a)



(b)

Fig. 5.6 Contrast in (a) permittivity and (b) conductivity between the malignant and healthy tissue listed in Table 5.1.

spectively. This calculation of wave physics implies the fundamentally achievable resolution of these imaging techniques.

The contrast of a microwave radar image is a result of the reflection at the tumor-tissue interface. The higher the dielectric contrast between the tumor and tissue, the stronger the reflection is, which leads to a better image contrast. Fig. 5.6 shows the contrast between the malignant and healthy tissue, which exhibits a wide range from 15 to 1.1 in permittivity and from 30 to 1.1 in conductivity.

We use a one-dimensional example shown in Fig. 5.7 to discuss the contrast in the thermoacoustic signals. The central slab represents the tumor and the two adjacent slabs represent the tissue. Skin is neglected in this example. We assume that the simulation domain is acoustically homogeneous and the slabs are uniformly excited by the pulse shown in Fig. 5.2(b) at a carrier frequency of 550 MHz. Let p_2 and p_1 denote the back-propagating thermoacoustic signals when the tumor slab is and is not present respectively. We define the time-domain SCR as

$$\frac{\max(p_2)}{\max(p_1)} . \quad (5.24)$$

From the Green's function solution in (5.22) and (5.23) and the definition of SAR in (5.3), the amplitude of the pressure due to a point source is directly proportional to the conductivity-heat capacity ratio. Therefore, (5.24) can be re-written as

$$\frac{\max(p_2)}{\max(p_1)} \approx \frac{\frac{\sigma_2}{c_{p,2}}}{\frac{\sigma_1}{c_{p,1}}} = \frac{c_{p,1}\sigma_2}{c_{p,2}\sigma_1} . \quad (5.25)$$

Fig. 5.8 shows the SCR as the tissue contains a decreasing amount of adipose content as in Table 5.2 evaluated at 550 MHz. The estimation in (5.25) using conductivity and heat capacity is also shown, which agrees with the simulated result. We conclude that the SCR is directly related to the ratio of conductivity and heat capacity.

5.5 Delay-And-Sum Algorithm

The wave equation remains invariant under the transform $t \rightarrow -t$ in a lossless medium. This is due to the second-order derivative with respect to time in the equation, which contrasts to the first-order derivative in the diffusion equation. The propagating field at one time instance can be translated to an earlier time to identify its source. This is the

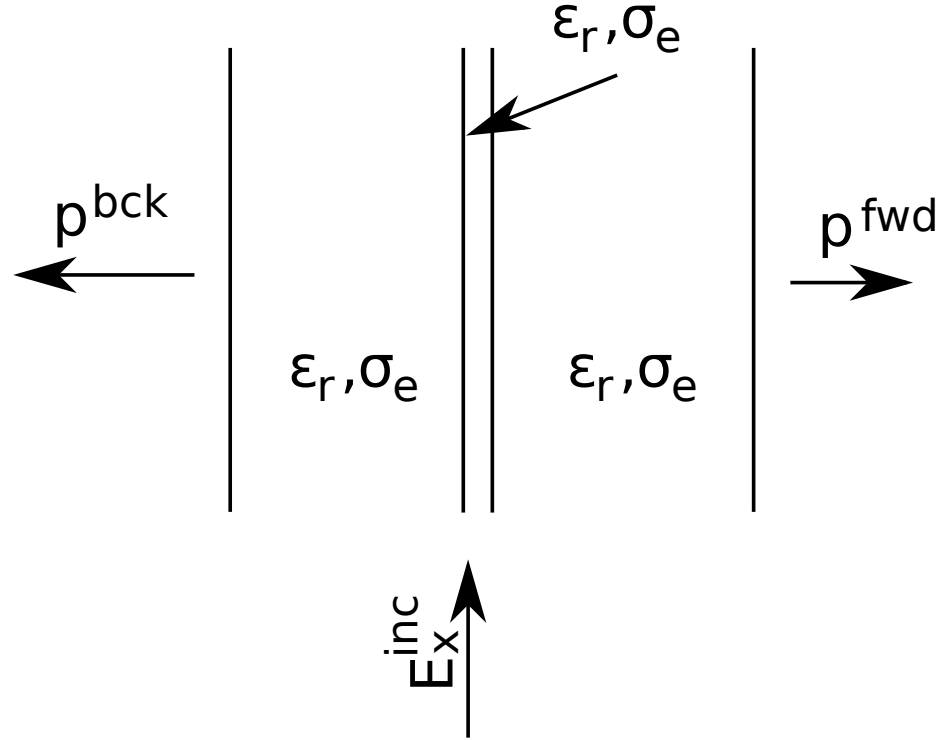


Fig. 5.7 A one-dimensional example with a three-layer slab to illustrate the contrast in the conductivity-heat capacity ratio in the thermoacoustic signals.

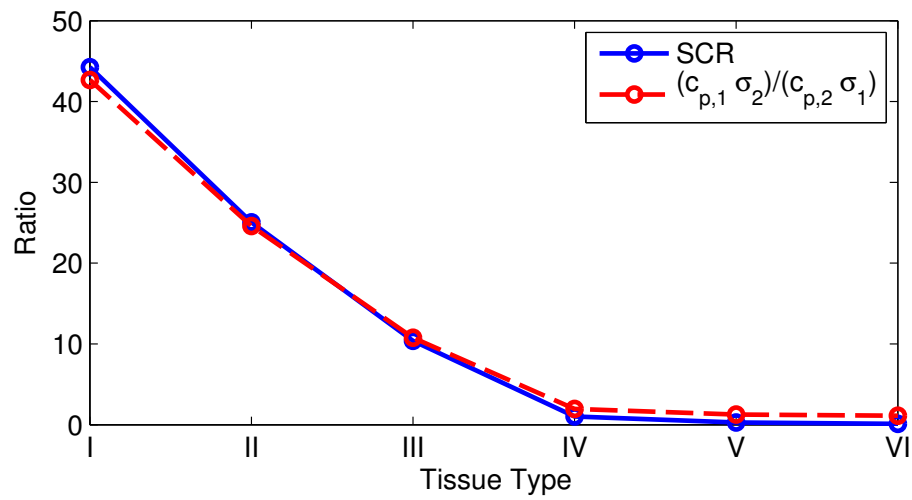


Fig. 5.8 Comparison of the simulated result of the one-dimensional example with the SCR defined in (5.24).

basic idea of the DAS algorithm [65, pp. 112], which is applicable to generate images from radar and thermoacoustic signals. The DAS algorithm to generate radar images includes four steps, which are described below:

1. *Calibration* - The received radar signals contain the early reflection of the skin, which is several orders of magnitude greater than the reflection due to the tissue. The methods proposed to reduce this initial reflection include the average-subtract method [89] and the filtering method [10, 127]. These methods operate on the assumption that the skin reflection is similarly seen at all antennas; thus, they can be removed by subtracting the weighted average.
2. *Time shift* - The purpose of the time shift is to coarsely align the received signals so that they are as if being produced at the same time instance at the scan point, \vec{r} . Let $\tau_i^{tissue}(\vec{r})$ and $\tau_i^{background}(\vec{r})$ denote the travelling time in the tissue and background medium along the straight path connecting the scan point and the i^{th} antenna. Then, the time-shifted signal is $\tilde{s}_i(t + 2(\tau_i^{tissue} + \tau_i^{background}))$, where \tilde{s}_i denotes the i^{th} calibrated radar signal.
3. *Amplitude compensation* - Two secondary cylindrically-spreading waves are generated by Huygen's principle, one at the scan point and the other at the intersection of the straight path and the background-skin interface. Diffraction inside skin is omitted due to it being electrically thin. Let $d_i^{tissue}(\vec{r})$ and $d_i^{background}(\vec{r})$ denote the propagation distance in the tissue and medium. The amplitude decreases linearly proportional to $\frac{e^{\beta^{tissue} d_i^{tissue}}}{\sqrt{d_i^{tissue}}}$ and $\frac{e^{\beta^{background} d_i^{background}}}{\sqrt{d_i^{background}}}$,⁵ where β^{tissue} and $\beta^{background}$ denote the frequency-dependent attenuation factor. The weight factor is calculated to compensate the amplitude decrease along the round trip, which is

$$w_i = \left(\frac{e^{\beta^{tissue} d_i^{tissue}}}{\sqrt{d_i^{tissue}}} \frac{e^{\beta^{background} d_i^{background}}}{\sqrt{d_i^{background}}} \right)^{-2}.$$

⁵The form of these factors comes from the far-field approximation of the Hankel function of the second kind, which describes the outward propagating field due to an infinitely-long line source.

4. *Pixel calculation* - The pixel intensity of a radar image is the energy of the time-shifted, compensated, summed signal, which is expressed as

$$\int_0^\infty \left(\sum_{i=1}^M w_i \tilde{s}_i(t + 2(\tau_i^{tissue} + \tau_i^{background})) \right)^2 dt ,$$

where M denotes the number of antennas.

The DAS algorithm is equally applicable to thermoacoustic signals with two modifications. First, a only one-way time shift and compensation are needed as the scan point is considered an isotropic acoustic excitation. Second, thermoacoustic images represent the heat absorption. As the absorption is linearly related to the amplitude of the thermoacoustic signals, the pixel intensity in a thermoacoustic image is the maximum amplitude of the summed signal. Thermoacoustic images are amplitude images, which contrasts to the radar energy images.

5.6 Imaging Results

In this section, we discuss the quality of images generated by the DAS algorithm from the simulated radar and thermoacoustic signals.

5.6.1 Homogeneous Medium with One Inclusion

A circular object mimicking the human breast with a radius of 45 mm and a skin thickness of 1.6 mm is placed in oil-like lossless matching medium characterized by the relative permittivity of 4.5. The scenario is shown in Fig. 5.9(a). In the radar simulation, there are 36 equally-spaced current sources placed around the object 20 mm away from the surface. Each emits a microwave pulse sequentially. This gives 36 mono-static measurements of the scattered field. The minimum wavelength, determined by the largest permittivity in the configuration at 6.85 GHz, is 5.64 mm. We set the spatial increment to 0.4 mm, less than one tenth of the wavelength. The maximum possible wavelength at 3.1 GHz is 50.3 mm. The simulation domain is truncated by 12 uniaxial perfectly-matched layers placed at half of this wavelength away from the source [120]. The parameters of the perfectly-matched layers are selected by sweeping the possible values of the parameters and monitoring the error of reflection. The computation domain contains 475×455 Yee cells. In the thermoacoustic

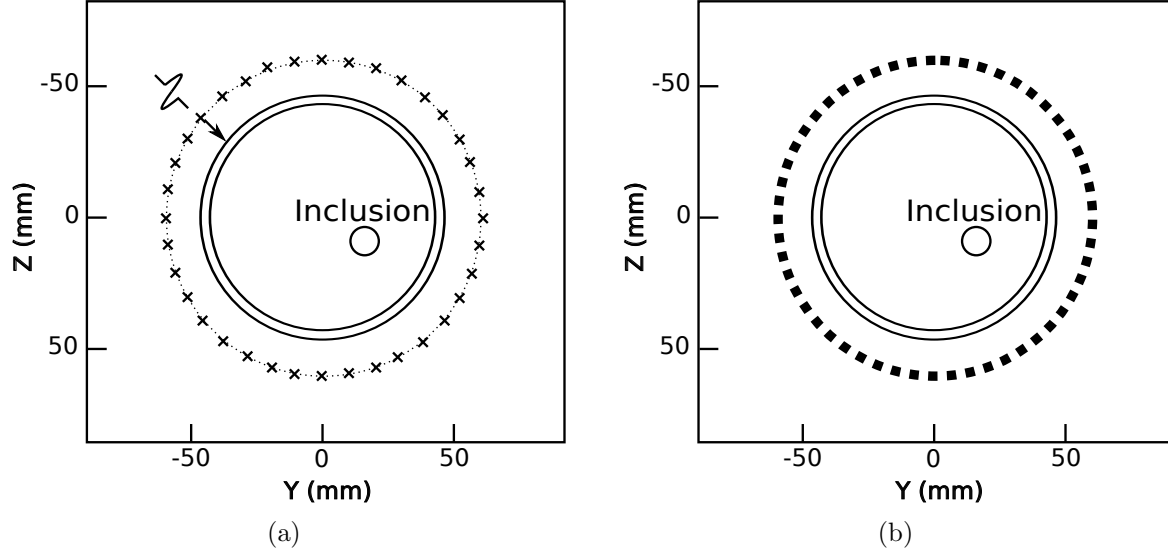
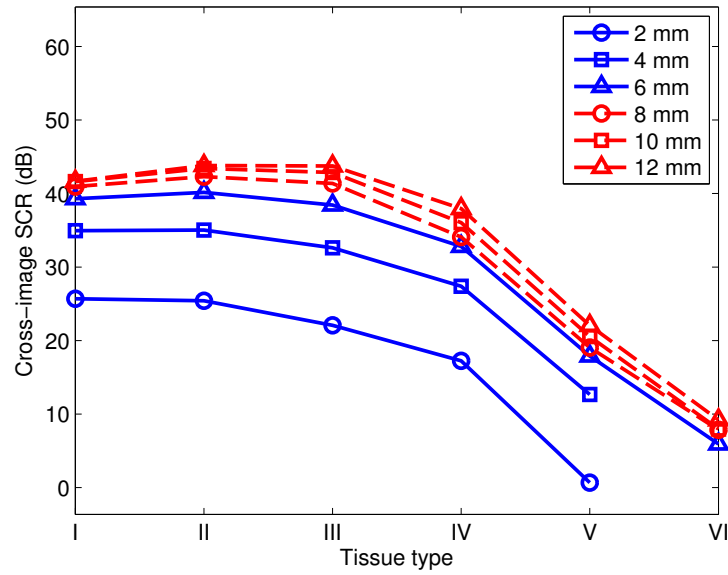


Fig. 5.9 (a) A mono-static microwave radar system. There are 36 current sources (marked as “x”) placed 20 mm away from the circular object radiating sequentially. (b) A microwave-induced thermoacoustic system. The object is uniformly excited. There are 80 transducers (marked as “■”) placed 20 mm away from the object simultaneously recording the thermoacoustic signals.

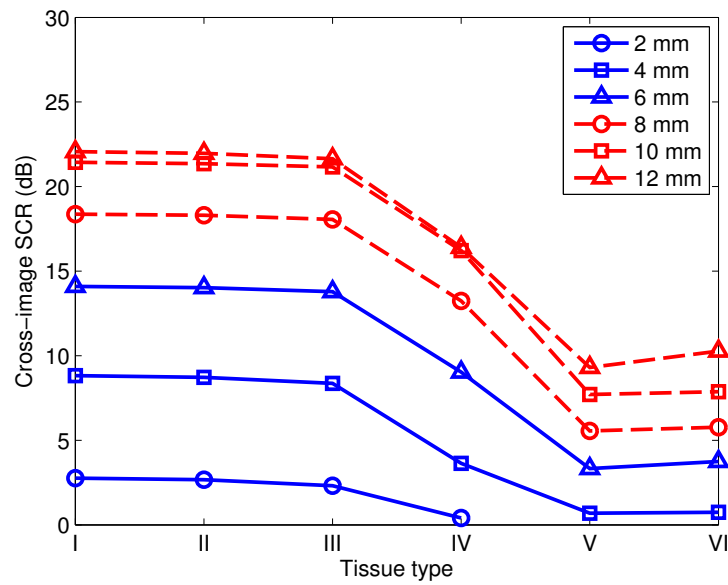
simulation, we assume the breast is uniformly excited at 550 MHz. There are 80 acoustic transducers placed around the breast as shown in Fig. 5.9(b). At 0.714 MHz, the acoustic wavelength is 2.1 mm. We set the spatial increment to 0.1 mm. The computation domain has 1500×1420 Yee cells.

A circular inclusion is placed at the location (10 mm, 16 mm). We vary its size and the dielectric properties of the tissue as listed in Table 5.1. The Debye model that approximates the Cole-Cole model of the tissue in the frequency range from 3.1 GHz to 10.6 GHz is implemented in the FDTD simulation.

We assume to have the knowledge of the average propagation speed of the electromagnetic wave and acoustic wave inside the tissue. For the electromagnetic wave, it is the speed evaluated at the central frequency and for the acoustic wave, it is 1510 m/s. We define the localization error to be the distance between the image peak and the centre of the inclusion. It is a metric to evaluate the ability of imaging algorithms to spatially correlate the image and the imaged object. Table 5.3 and Table 5.4 summarize the localization errors as the DAS algorithm is applied to the radar and thermoacoustic signals. The localization errors,



(a)



(b)

Fig. 5.10 Cross-image SCR of (a) radar images and (b) thermoacoustic images.

Table 5.3 Distance between the image peak and the centre of the inclusion in the radar images

Tissue Types	Inclusion diameter					
	2 mm	4 mm	6 mm	8 mm	10 mm	12 mm
I	0.3536	0.3536	0.3536	2.3717	0.3536	0.3536
II	0.3536	0.3536	0.3536	0.7906	0.3536	0.3536
III	0.3536	0.7906	0.7906	0.7906	0.3536	0.3536
IV	0.3536	0.3536	0.3536	0.7906	0.7906	1.0607
V	-	0.3536	0.3536	0.3536	0.3536	0.7906
VI	-	-	0.3536	0.3536	0.3536	1.0607

Table 5.4 Distance between the image peak and the centre of the inclusion in the thermoacoustic images

Tissue Types	Inclusion diameter					
	2 mm	4 mm	6 mm	8 mm	10 mm	12 mm
I	0.3536	0.3536	0.3536	1.0607	1.9039	2.8504
II	0.3536	0.3536	0.3536	1.0607	1.9039	2.8504
III	0.3536	0.3536	0.3536	1.0607	1.9039	2.8504
IV	0.3536	0.3536	0.3536	1.0607	1.7678	2.8504
V	-	0.3536	0.3536	2.5739	3.2596	4.3732
VI	-	0.3536	1.0607	2.1506	3.1820	4.1382

which are two-times larger than the diameter of the inclusion, are excluded from the tables. The DAS algorithm performs equally well on the two signals with the peak deviating a few millimetres from the centre of the inclusion. The cross-image SCR is defined as the mean energy within the area of 3 dB below the main lobe in the images containing the inclusion and the mean energy within the same area in the images free of the inclusion. Fig. 5.10(a) and Fig. 5.10(b) show the cross-image SCR as a function of the tissue types, when the inclusion varies its size. Both the radar and thermoacoustic techniques demonstrate a diminishing SCR as the adipose content decreases or the inclusion size decreases.

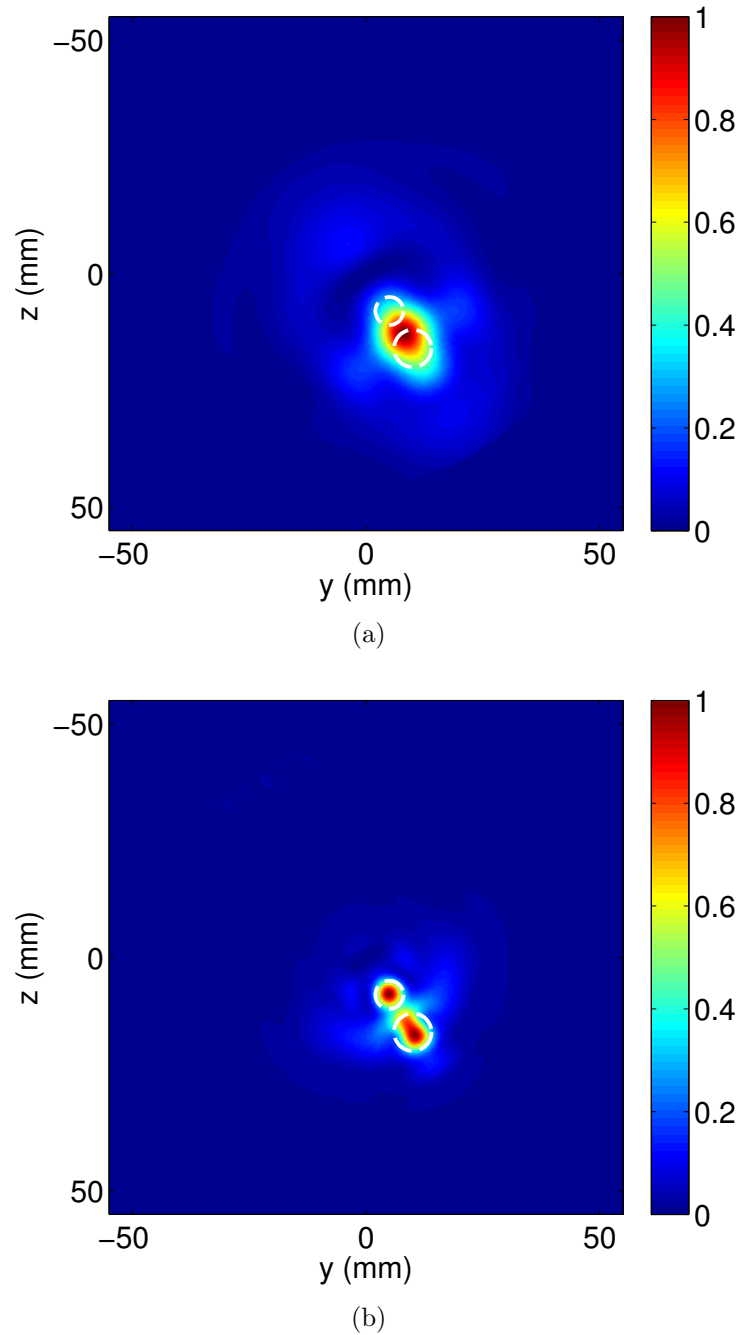


Fig. 5.11 Radar images from the DAS algorithm attempting to resolve two closely spaced inclusions in a homogeneous medium with (a) tissue being of Type III and (b) tissue being of Type IV as defined in Table 5.1.

5.6.2 Homogeneous Medium with Two Inclusions

In this scenario, two inclusions are placed at (5 mm, 8 mm) and (10 mm, 16 mm) with diameters of 6 mm and 8 mm respectively. Fig. 5.11(a) shows the radar image when the tissue is of Type III. The resolution of the images is 0.5 mm×0.5 mm per pixel. The two inclusions cannot be resolved. This is because, even though there is a dielectric contrast between the inclusions and tissue, multiple reflections occur between the inclusions. These reflections contaminate the dominant reflection from the inclusion, affecting the image quality. Fig. 5.11(b) shows the radar image when the tissue is of Type IV. In this case, the two inclusions are spatially resolved despite a smaller dielectric contrast between the inclusions and tissue. This is because as the dielectric properties of the tissue increase, the physical size of a wavelength decreases, which effectively increases the electric size of the inclusions and the image resolution. This example illustrates that the image quality is related to both contrast and resolution. Even though the contrast is low, good spatial resolution improves the overall quality of an image.

For the comparison purpose, we have also implemented the frequency-domain beamforming (FDB) algorithm introduced in [26]. It is expected to offer superior performance to identify point scatterers than the DAS algorithm, as the beamformer spatially selects the scan point while suppressing the interference from its neighbouring scatterers. This is achieved by solving a penalized least-square problem for the beamformer weights for each scan point. Fig. 5.12 shows the radar image generated by the FDB algorithm from the signals, with which the DAS algorithm has previously failed. It is shown that two energy peaks appear corresponding to the two inclusions, even though one peak is 4.23 dB, which is lower than the other. The locations of the peaks are shifted more towards the centre. This is due to the fact that the FDB algorithm makes the far-field assumption in optimizing the weights. Deeper locations, more consistent with this assumption, are favoured over shallower locations. Thus, the FDB algorithm offers improvement over the DAS algorithm when imaging point scatterers at the price of possible localization errors. Fig. 5.13 shows the thermoacoustic images. As the tissue is almost acoustically homogeneous, little acoustic reflection occurs between the inclusions. The DAS algorithm is sufficient to identify their presence in two types of tissue.

5.6.3 A Heterogeneous Breast Model

Finally, to compare the imaging capability of the radar and thermoacoustic techniques, we test them with a heterogeneous breast model derived from a T1-weighted magnetic resonance image, shown in Fig. 5.14. In the radar simulation, the pixel intensities are mapped to the Debye parameters by the rule specified in [147]. The relative permittivity and effective conductivity evaluated at 6.85 GHz are shown in Fig. 5.15(a) and Fig. 5.15(b). In the thermoacoustic simulation, the pixel intensities are mapped to the dielectric properties at 550 MHz by the rule specified in [147]. The acoustic heterogeneity is also modelled by linearly mapping the pixel intensities to the acoustic speed and heat capacity: the largest pixel intensity denoting adipose-dominant tissue is mapped to the smallest acoustic speed and heat capacity. The space dependent conductivity-heat capacity ratio, which serves as the source of the thermoacoustic signals is shown in Fig. 5.16.

Fig. 5.17 shows the thermoacoustic image generated. The image does not directly resembles the space-dependent parameter shown in Fig. 5.16 due to the introduced acoustic heterogeneity. However, it reasonably reflects that the glandular tissue is concentrated to the right half of the model and the several spots correspond to thermoacoustic sources. Fig. 5.18 shows the radar images generated by the DAS and FDB algorithm. Neither of them are capable of generating a image that correlates with the tissue properties. The dispersion and heterogeneity of the numerical model pose a challenging task to the radar techniques.

5.7 Conclusions

In this chapter, we used the DAS algorithm to generate images from the radar and thermoacoustic signals and compared the qualities of the images. We found that both radar and thermoacoustic techniques were capable of imaging a dielectric inclusion in a homogeneous medium. The radar techniques failed to resolve inclusions being placed in a close proximity. This could be improved by the space-time beamforming algorithm, which suppresses the reflection from neighbouring scatterers at the price of possible localization errors. When being applied to image a heterogeneous breast model, the radar techniques suffered from microwave dispersion. The image from the thermoacoustic techniques was able to reveal some spatial details correlated with the heterogeneity of the tissue. This suggests that the

thermoacoustic techniques may offer superior performance than the radar techniques when being applied to image breasts.

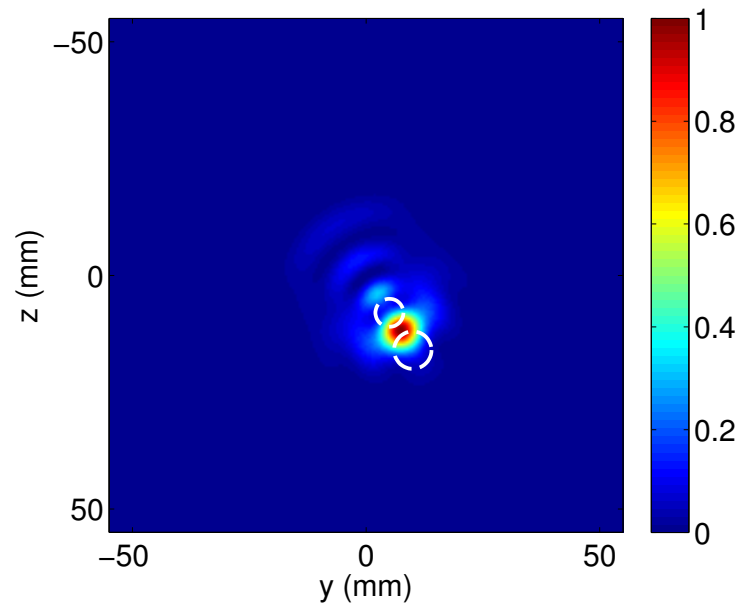
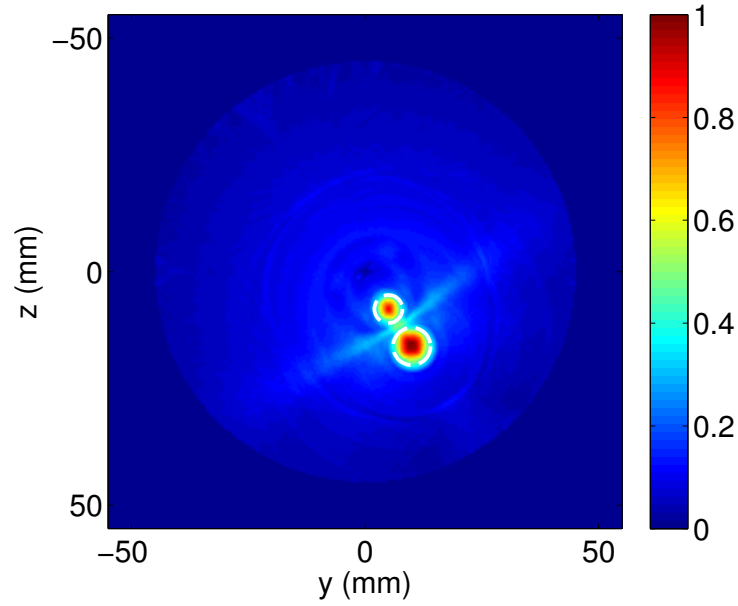
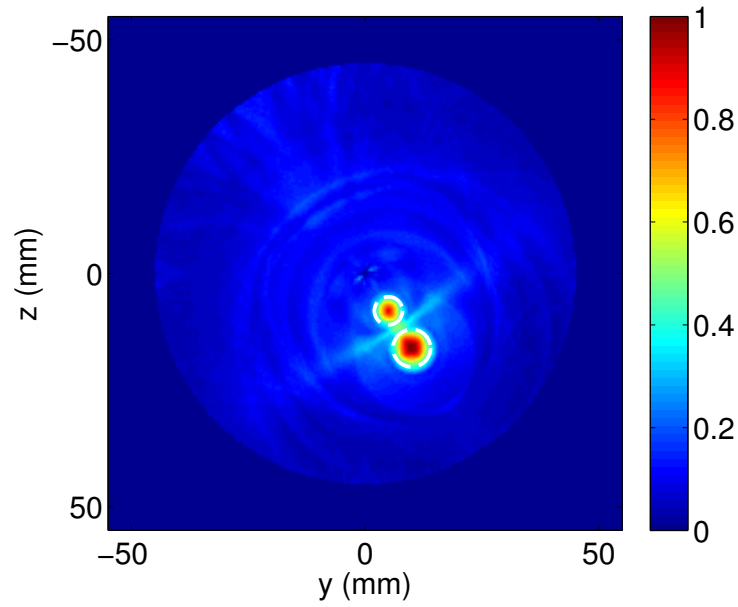


Fig. 5.12 Radar image from the FDB algorithm attempting to resolve two closely spaced inclusions in a homogeneous medium with tissue being of Type III as defined in Table 5.1.



(a)



(b)

Fig. 5.13 Thermoacoustic images from the DAS algorithm attempting to resolve two closely spaced inclusions in a homogeneous medium with (a) tissue being of Type III and (b) tissue being of Type IV as defined in Table 5.1.

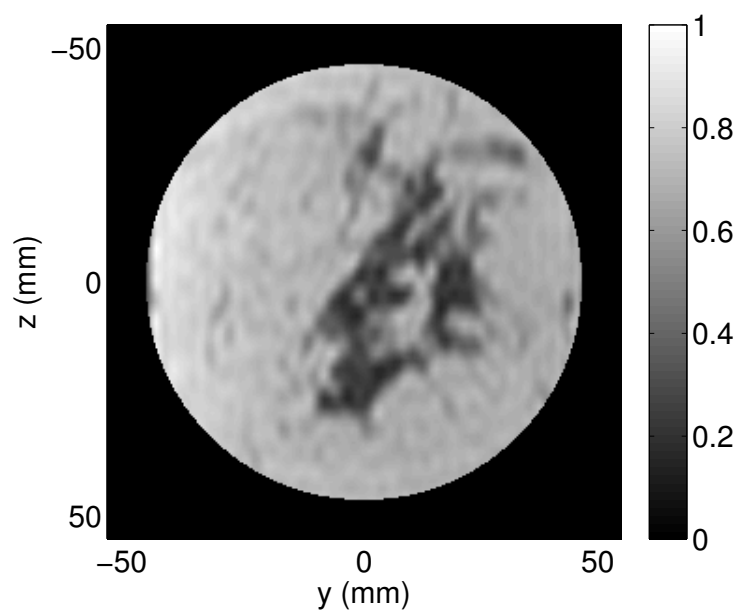
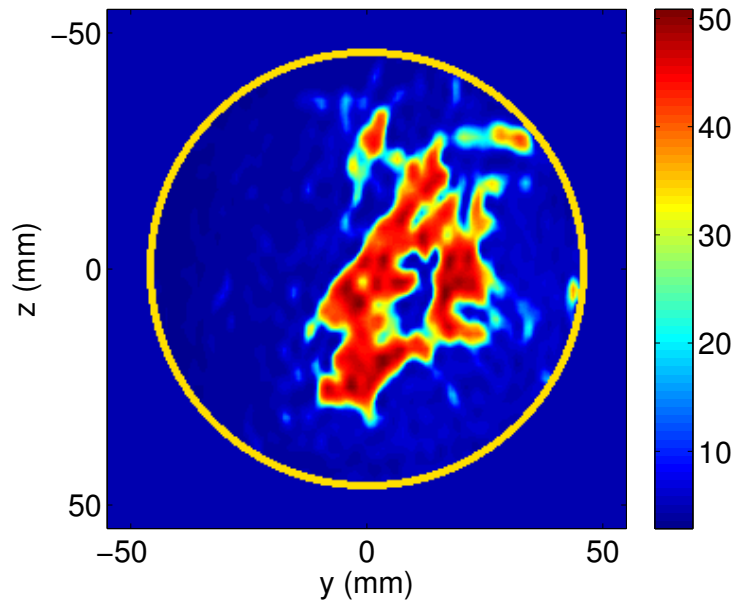
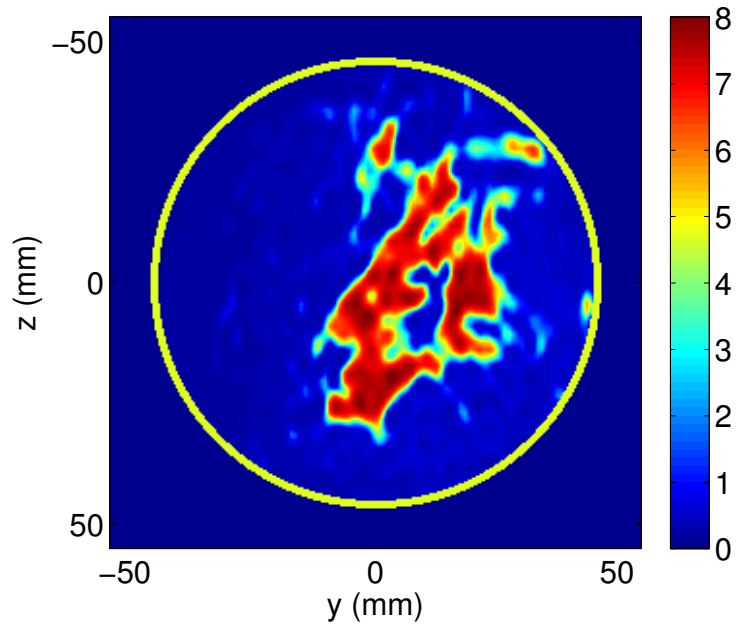


Fig. 5.14 A circularly cropped T1-weighted magnetic resonance image.



(a)



(b)

Fig. 5.15 Dielectric properties of the breast model constructed from the magnetic resonance image evaluated at 6.85 GHz (a) relative permittivity and (b) effective conductivity.

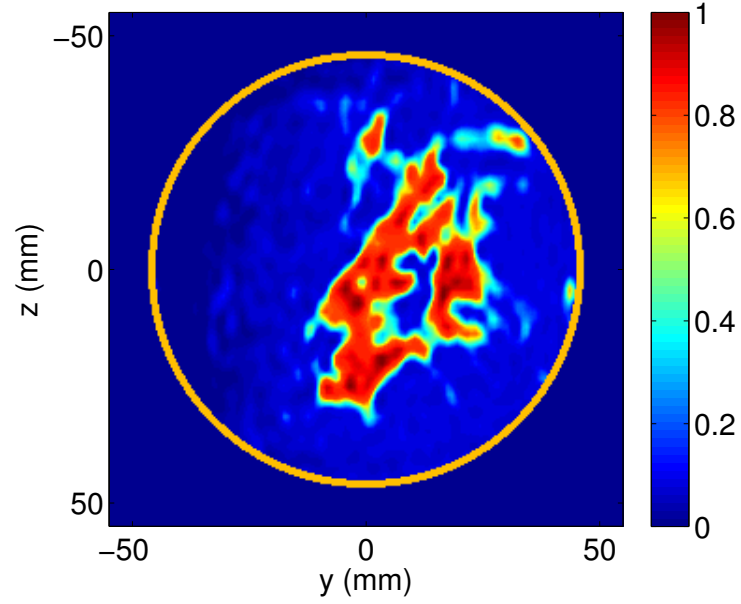


Fig. 5.16 Normalized space-dependent conductivity-heat capacity ratio, where the effective conductivity is evaluated at 550 MHz.

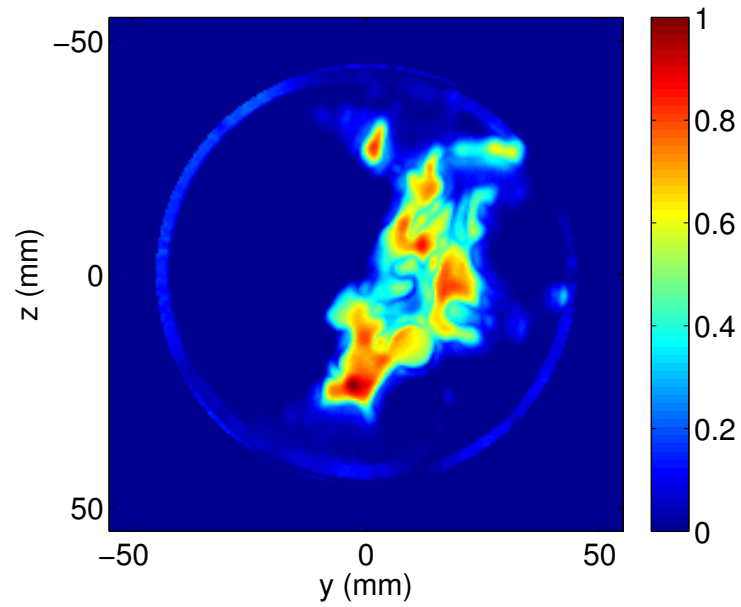
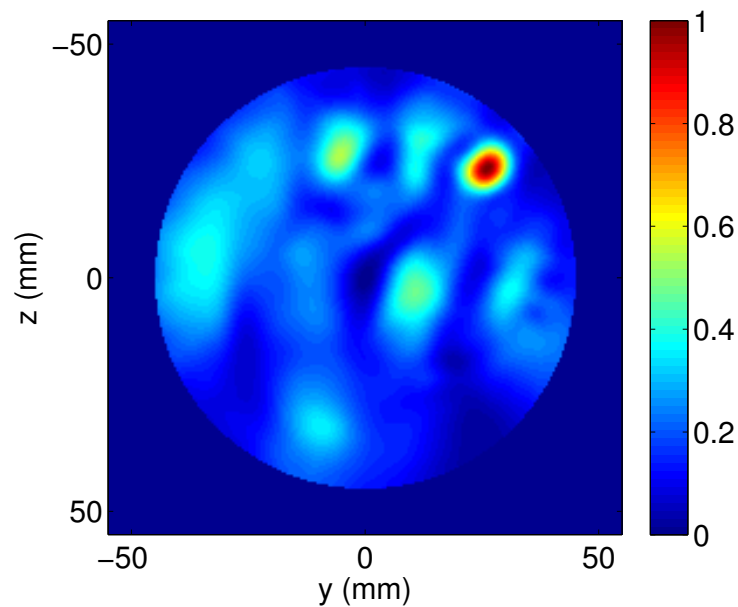
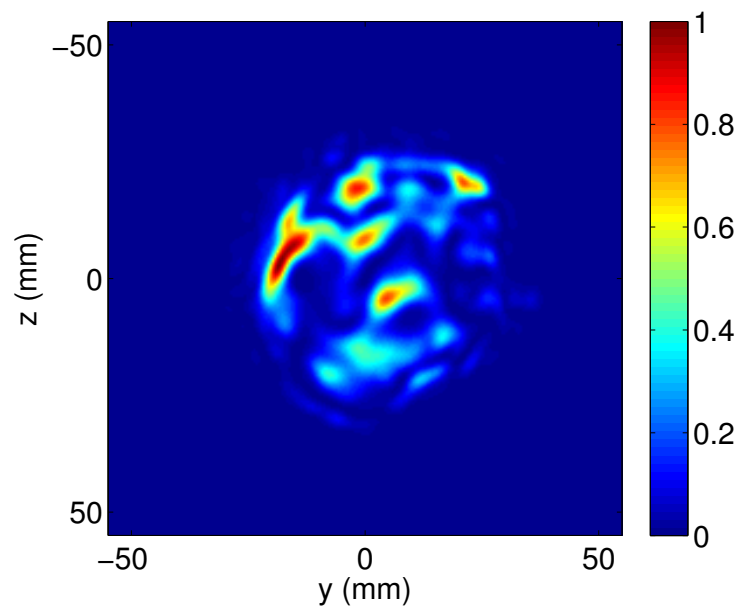


Fig. 5.17 Thermoacoustic image generated from the DAS algorithm.



(a)



(b)

Fig. 5.18 Radar images generated from (a) the DAS algorithm and (b) the FDB algorithm.

Chapter 6

Microwave-Induced Thermoacoustics Assisting Microwave Tomography

In microwave tomography, antennas radiate sinusoidal signals towards a pendent breast and receive the scattered signals. The problem of recovering the permittivity and conductivity of the breast tissue from the scattered signals is known as the inverse-scattering problem [19]. There exist algorithms to solve this problem and generate images of permittivity and conductivity distribution of the breast tissue in the two-dimensional space. We notice that the previously built tomographic systems operated in the frequency range from 300 MHz to 1200 MHz [99, 111, 63], and the previously built thermoacoustic systems used 434 MHz as the carrier frequency for the deposition of microwave energy [80]. Combining these two systems into one may enhance image quality of each one of them.

Previously, the researchers at the University of Florida proposed to generate a low-contrast ultrasound image of a pendent breast [63]. They extracted a non-uniform mesh from the ultrasound image of the tissue region, in which the region that indicated the possible presence of malignant tissue was resolved with more triangular elements than other regions. Then, they deployed a microwave tomographic system to image the same breast and calculated the permittivity and conductivity on this non-uniform mesh. They showed that the malignant tissue was only marked on the images generated from this non-uniform mesh.

We hypothesized a system that would use antennas to excite the thermoacoustic process and provide an image. And we would use the non-uniform mesh extracted from this image

and the same antennas to image the breast as in microwave tomography. Such a system would not need a separate rotating ultrasound system as in [63], and avoid any error associated with the displacement of the breast due to the switch from the ultrasound system to the tomographic system.

We noticed that the microwave excitation of a thermoacoustic process needs to have a large instantaneous power, greater than 10 kW, and needs to create a uniform field in the tissue, while the excitation in a tomographic system can be on the scale of a few milliwatts. This led to a conflict between the number of antennas to meet the requirement of both excitations and the space available around the pendent breast. We concluded that it is not feasible to reconcile this conflict within a single system design.

This chapter is structured as follows. Section 6.1 presents the hypothesized system and the algorithm to solve the inverse-scattering problem. Section 6.2 discusses the engineering issue regarding the requirements on the antennas. Section 6.3 concludes the chapter.

6.1 System Design and Imaging Algorithm

The system involved interleaving antennas and acoustic transducers arranged around a pendent breast. They were immersed in a high permittivity liquid for microwave and acoustic coupling. The antennas were responsible for radiating micro-second pulses to the breast to create a uniform field and excite the thermoacoustic process. These antennas were also responsible for sequentially radiating a microwave sinusoid while the non-radiating antennas received the scattered field.

From the thermoacoustic signals, we could use the delay-and-sum algorithm to generate an image of the breast. The local pixel intensities affected the edge length of the local triangular elements. The large values of the intensities corresponded to small edge lengths and small elements, while small values of the intensities corresponded to large elements. We used the software GMSH [42] to generate a non-uniform mesh and the software DistMesh [108] to generate a uniform mesh with the similar number of elements, both of which are shown in Fig. 6.1

The inverse-scattering problem could be formulated as an un-constrained minimization

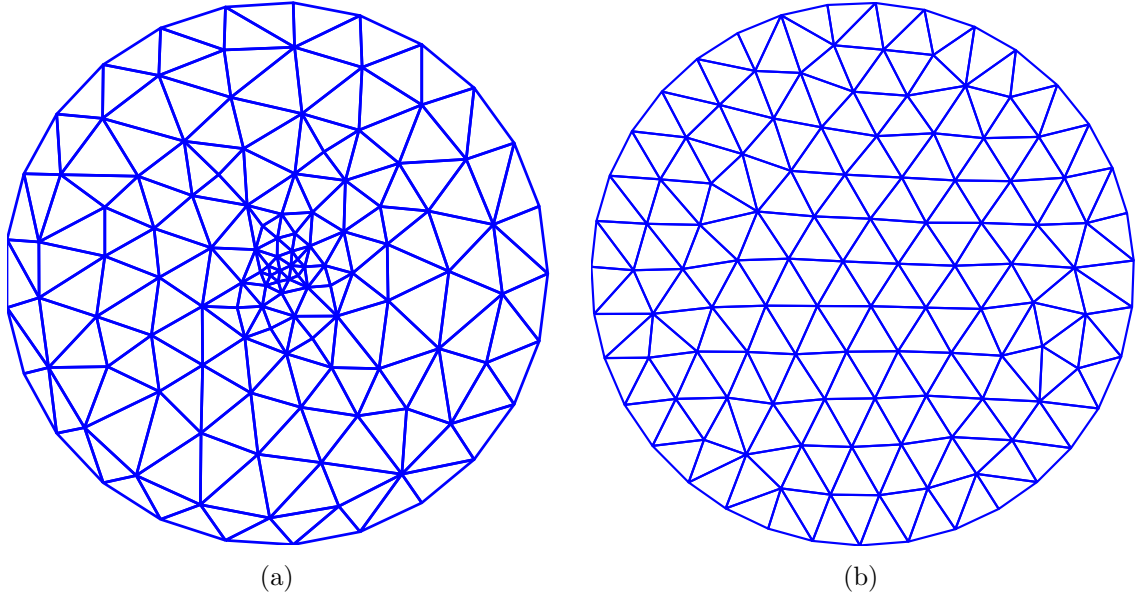


Fig. 6.1 (a) A non-uniform mesh extracted from a thermoacoustic image, in which the region with the possible presence of tumor is resolved with more elements. There are 120 nodes and 213 elements. (b) A uniform mesh, in which all regions are resolved with elements of approximately the same dimension. There are 118 nodes and 199 elements.

of a least-square cost functional (2.1), which, repeated here for convenience, is

$$\xi = \sum_{i=0}^{M-1} \left\| \vec{E}_i^{meas} - \vec{E}_i^{calc} \right\|_2 . \quad (6.1)$$

The minimization of this functional is well solved by the gradient-based iterative algorithms [106].

The iterative process to solve the inverse problem is summarized in Fig. 6.2. Briefly, we obtained the error between the measured fields and the calculated fields from a forward solver. If the error was larger than some pre-determined threshold, we calculated the gradient of \vec{E}^{calc} with respect to the variation of the wave numbers, which were related to the permittivity and conductivity of tissue. The gradient could be used directly in the gradient-descent method, or used to assemble the Jacobian matrix to form the normal equations as in the Gauss-Newton method and the Levenberg-Marquardt method. All of these methods provided updates on the wave numbers, from which we got an new

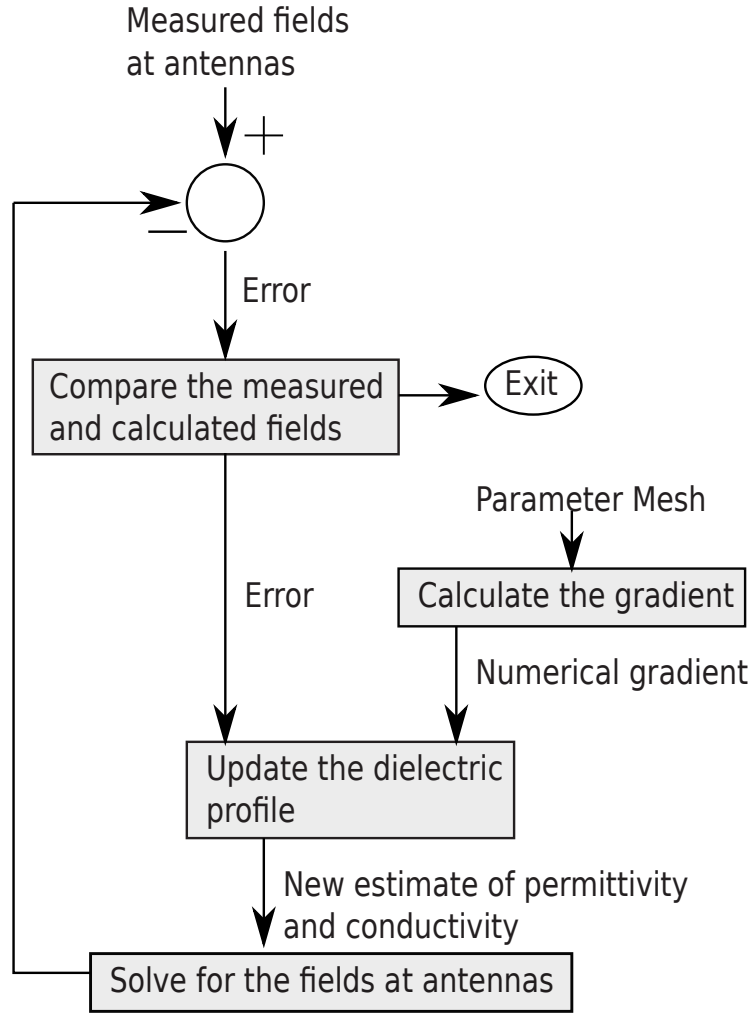


Fig. 6.2 Flow chart to demonstrate the solution to the inverse problem using the gradient-based optimization methods.

permittivity and conductivity in the tissue. Then we used the forward solver with the new permittivity and conductivity to calculate the fields for the next comparison with the measured field.

The challenge associated with the gradient-based optimization algorithms is the need to calculate the gradient, which reflects how the calculated fields vary with respect to the changes of the wave numbers in the tissue. We use a two-dimensional example to illustrate this calculation using the nodal adjoint method in microwave tomography [35]. Assuming

we have a transverse magnetic wave polarized in the x direction, we can show that

$$\nabla^2 E_x + k^2 E_x = j\omega\mu_o J_{x,i} , \quad (6.2)$$

where E_x and $J_{x,i}$ are the time-harmonic electric field intensity and the impressed current density representing a microwave excitation from antennas, both of which are polarized in the x direction. k is the complex wave number related to permittivity and conductivity. ω and μ_o are the angular frequency and the absolute permeability in vacuum. Eq. (6.2) can be succinctly written as

$$\mathcal{L}E_x = f , \quad (6.3)$$

where \mathcal{L} denotes the linear operator $\nabla^2 + k^2$, and f denotes $j\omega\mu_o J_{x,i}$. It can be shown that \mathcal{L} is a self-adjoint linear operator [50, 154] under the symmetric product defined as $\langle E_x, f \rangle = \int E_x f d\Omega$ and the homogeneous Dirichlet and Neumann boundary conditions.¹ The self-adjointness of \mathcal{L} lies in the heart of the proof of the Lorentz reciprocity theorem, which states that if $E_{x,1}$ is the field due to the excitation f_1 under \mathcal{L} , and $E_{x,2}$ is the field due to the excitation f_2 then

$$\langle E_{x,1}, f_2 \rangle = \langle f_1, E_{x,2} \rangle . \quad (6.4)$$

Performing an implicit differentiation on the relation $\mathcal{L}E_{x,2} = f_2$ with respect to k^2 in the region without any excitation, we obtain

$$\mathcal{L} \frac{\partial E_{x,2}}{\partial k^2} = - \frac{\partial \mathcal{L}}{\partial k^2} E_{x,2} . \quad (6.5)$$

Applying the reciprocity theorem stated in (6.4) to (6.5) and the relation $\mathcal{L}E_{x,1} = f_1$, we obtain

$$\left\langle \frac{\partial E_{x,2}}{\partial k^2}, f_1 \right\rangle = \left\langle E_{x,1}, - \frac{\partial \mathcal{L}}{\partial k^2} E_{x,2} \right\rangle . \quad (6.6)$$

If we let f_1 denote a Dirac delta current source located at \vec{r}_1 , then (6.6) becomes

$$\int \frac{\partial E_{x,2}}{\partial k^2} j\omega\mu_o \delta(\vec{r} - \vec{r}_1) d\Omega = - \int E_{x,1} \frac{\partial \mathcal{L}}{\partial k^2} E_{x,2} d\Omega ,$$

¹There is no conjugation involved in the definition of the symmetric product. The value of this product is known as the reaction in the literature [52, pp. 118]. This definition opposes to the definition of the conjugated inner product in the Euclidean space, which represents energy.

which leads to

$$\frac{\partial E_{x,2}(\vec{r}_1)}{\partial k^2} = -\frac{1}{j\omega\mu_o} \int E_{x,1} \frac{\partial \mathcal{L}}{\partial k^2} E_{x,2} d\Omega . \quad (6.7)$$

The left hand side of (6.7) represents the sensitivity of the electric field evaluated at the location \vec{r}_1 due to a current source at the location \vec{r}_2 with respect to the wave number. This is an element of the gradient vector. The values of k in the tissue region are interpolated over the non-uniform mesh, also known as the parameter mesh. They are needed to numerically evaluate the integration on the right hand side of (6.7).

6.2 Engineering Consideration

Microwave tomographic systems can use monopole antennas to radiate and receive low-power sinusoid. Microwave-induced thermoacoustic systems have more stringent requirements. The antennas are intended for microwave heating; thus, they need to be able to handle large power. Another requirement on the antennas is that they need to create a uniform field in the breast tissue. This is an important requirement. If the field inside the tissue is uniform, the microwave absorption is directly proportional to the conductivity-heat capacity ratio. The images generated from the thermoacoustic signals are direct reflection of the microwave absorption; thus, they are also direct reflection of the conductivity-heat capacity ratio, which is an endogenous property of the tissue. If the field inside is not uniform, certain regions that have lower conductivity-heat capacity ratio can be heated more than the high-ratio regions. The thermoacoustic images lose their correlation to the tissue property.

The requirement on a uniform field translates to the requirement on the microwave carrier frequency. The study in [44] used a semicircular dielectric waveguide backed by a perfect magnetic conductor to mimic the breast and the chest wall. It is shown that field distribution was near uniform at the dominant mode of this waveguide, and the cut-off frequency of the higher modes was 817 MHz assuming a breast radius of 5 cm and a relative permittivity of 9. As the field distribution was not uniform at higher modes [143], it is suggested that one needs to use the frequencies below 817 MHz. In addition, the choice of 434 MHz in [80] is due to the fact that water has high microwave absorption at this frequency.

The studies in [84, 86] have shown that the relative permittivity of healthy breast

tissue in the frequency range of 500 MHz to 1 GHz varies from 5 to 55 as shown in Fig. 5.3. Following the calculation in [44] and assuming a breast radius of 5 cm, the cut-off frequency is from 312 MHz to 1.15 GHz for the noted possible range of relative permittivity. The matching liquid recommended for microwave tomographic systems provides a good microwave matching with a relative permittivity around 20 [100], and it provides a good acoustic matching. The wavelengths of the frequencies in the range from 312 MHz to 1.15 GHz vary from 21.5 cm to 5.8 cm. To have rectangular horn antennas effectively radiate at these frequencies, the dimension of the antennas is about half of the wavelength. Given a 2-cm distance from the antennas to the breast surface, it would be difficult to fit 32 horn antennas that not only create a uniform field, but also meet the number of antennas needed in the previously built microwave tomographic systems.² In addition, such calculation has not included the space for acoustic transducers. Thus, we conclude that it is not feasible to reconcile the antenna requirements of microwave tomographic systems and microwave-induced thermoacoustic systems, and combine them into one system.

6.3 Conclusions

In conclusion, we discussed a system that could combine a microwave tomographic system and a microwave-induced thermoacoustic system with the aim to increase the image quality of microwave tomography via non-uniform parameter meshes. However, as the microwave tomographic system requires many number of measurements and the microwave-induced thermoacoustic system requires a low frequency to create a uniform field in the breast, we conclude that it is not feasible to construct a single system with antennas that simultaneously meet the requirements of a microwave-induced thermoacoustic system and a microwave tomographic system.

²We need to maintain the number of measurements in the calculation of the permittivity and conductivity of the tissue. Without sufficient number of measurements, the search space for optimal permittivity and conductivity is enlarged and the solution that minimizes (6.1) may not be unique.

Chapter 7

Summary

7.1 Thesis Contributions

This thesis is a collection of contributions in the area of microwave breast imaging. Recent characterization of the dielectric properties in the microwave range has shown a contrast between the malignant and healthy tissue lower than what had previously been reported in the literature [84, 86]. We derived the analytic expression of the scattered field in the problem of a plane wave scattered by a multi-layer sphere. We also predicted the strength of the tumor response as the tumors were buried in the three kinds of breast tissue categorized in [84, 86]. These results identify the requirement on the power resolution and bandwidth of a mono-static microwave radar system for breast tumor detection.

Currently available numerical breast models for the studies in microwave breast imaging consist of hundreds of thousands of solids to approximate the heterogeneity of breast tissue, which render the Modeller of commercial electromagnetic software unusable. We applied the classification and regression tree analysis to the heterogeneous tissue. The solid-wise approximation of the tissue averaged the inherent noise present in the magnetic resonance images and provided a complexity penalty for users to determine the number of solids needed in the breast model. Equipped with these breast models, users can take advantage of commercial electromagnetic software to include complex antennas and perform full-wave electromagnetic simulations.

We also evaluated the microwave radar techniques and the microwave-induced thermoacoustic techniques. We confirmed that the contrast in radar signals is due to the contrast in permittivity and conductivity of malignant and healthy tissue, and found that the con-

trast in thermoacoustic signals is due to the contrast in conductivity-heat capacity ratio. In addition, we found that due to the strong diffraction and dispersion, the microwave radar techniques experienced difficulty to image a breast with heterogeneous tissue. Since the wavelengths associated with thermoacoustic signals are smaller than the dimension of tumors, the microwave-induced thermoacoustic techniques have the potential to provide more spatial details that constitute the heterogeneous anatomy.

Finally, we conclude that it is not feasible to construct a single system with antennas that simultaneously meet the requirements of a microwave-induced thermoacoustic system and a microwave tomographic system.

7.2 Future Works

7.2.1 Measurements of Dielectric Properties

An independent tissue characterization effort was conducted at the Dartmouth college in 2009 [49]. The authors confirmed similar results on the dielectric properties of adipose-dominant tissue reported in the early work [17, 129, 15, 66] and the recent work [84, 86]. It is known that the dielectric properties of *in vivo* tissue differ from *ex vivo* tissue. The authors observed that within the initial 5 minutes after tissue excision, the malignant tissue dehydrated and its permittivity and conductivity in the frequency range from 0.1 GHz to 9 GHz decreased the most and then stabilized over hours. They also noticed that there was a 5-min to 5-hour lapse between the time that the tissue samples were removed and the time that the *ex vivo* measurements were conducted in [84, 86]. Thus, the authors concluded that the results of the *ex vivo* measurements cannot be readily extrapolated to conclude on the *in vivo* dielectric properties of malignant and healthy tissue. The variation of dielectric properties of tissue, as a function of time elapsed after biopsy deserves further investigation to confirm the findings in [49].

7.2.2 Contrast-Enhanced Microwave Imaging

Contrast agents can loosely refer to chemicals that temporarily alter the physical properties of tissue and have been commonly used in medical imaging. Due to the reduced contrast in the dielectric properties, one line of research in microwave radar imaging is to identify chemicals that would serve as a contrast agent to temporarily and selectively bind

with malignant tissue and elevate its permittivity and conductivity.¹ Microbubbles are known to increase the acoustic speed in injected tissues and have been used in ultrasound imaging. They have been also shown to alter the permittivity and conductivity of malignant tissue [95]. More recently, single-wall carbon nano tubes, used in magnetic resonance imaging and positron emission tomography, have been shown to increase the permittivity and conductivity of tissue-mimic phantom at 3 GHz by 37% and 81%, depending on the concentration [94, 114]. Also, magnetic nano particles being placed in a static polarizing magnetic field, alters the radiated electromagnetic fields as in microwave radar [8]. These contrast agents would benefit microwave radar, microwave tomographic, and microwave-induced thermoacoustic imaging via differential imaging, which has yet been quantified in the literature. The apparent downside of using contrast agents is the need of intravenous injection, which incurs pain and anxiety in the screened patients. This limits their use in medical screening and jeopardizes the main attraction of microwave-based techniques - the non-invasiveness and cost-effectiveness.

7.2.3 Contrast Resolution Trade-off in Microwave Radar Imaging

Current microwave radar systems perform measurements in the frequency range from 1 GHz to 15 GHz depending on the choice of the matching medium. The frequency-domain measurements are converted to the time domain, and the outputs are convolved with incident pulses to produce the time-domain signals. These time-domain signals are inputs to the imaging algorithms. The results in Chapter 3 have predicted that most of the energy reflected by tumors concentrates in the frequency range from 0.5 GHz to 5.0 GHz in the presence of a low level of dielectric contrast. Based on this prediction, we could perform convolution with pulses that occupy this frequency range, which effectively filters the clutter response and may increase the signal-to-clutter ratio. The price paid for the reduced bandwidth of the pulse is a possible loss in spatial resolution in the images. This trade-off, perhaps, can be characterized by the modulation transfer function [116, pp. 66], which denotes the curve of contrast plotted against spatial frequency.

¹It should be noted that the gadolinium-based contrast agents used in magnetic resonance breast imaging temporarily shorten the T1 relaxation time. This increases the signal intensity from both healthy and malignant tissue [57]. The aim is to enhance signals from the noise floor but not to discriminate malignant tissue from healthy tissue.

Appendix A

Proof of (3.23)

The results in (3.23) are restated below

$$\frac{P_n^1(x)}{\sin \theta} \Big|_{x=\cos \theta} = (-1)^n \frac{n(n+1)}{2}, \quad \theta = \pi, \quad (\text{A.1a})$$

$$\sin \theta P_n^{1'}(x) \Big|_{x=\cos \theta} = (-1)^n \frac{n(n+1)}{2}, \quad \theta = \pi. \quad (\text{A.1b})$$

which are also stated in [7, pp. 656]. The derivation is explicitly shown here.

To prove (A.1a), we use one of the recurrent relation of the associated Legendre polynomial, which is

$$P_{n+1}^1(x) = \frac{2n+1}{n} x P_n^1(x) - \frac{n+1}{n} P_{n-1}^1, \quad$$

where $x = \cos \theta$. and thus

$$\frac{P_{n+1}^1(x)}{\sin \theta} = \frac{2n+1}{n} x \frac{P_n^1(x)}{\sin \theta} - \frac{n+1}{n} \frac{P_{n-1}^1(x)}{\sin \theta}. \quad (\text{A.2})$$

Let us define $c_n(x) = \frac{P_n^1(x)}{\sin \theta}$, then (A.2) can be rewritten as

$$c_{n+1}(x) = \frac{2n+1}{n} x c_n(x) - \frac{n+1}{n} c_{n-1}(x). \quad (\text{A.3})$$

Since

$$\begin{aligned} P_1^1(x)|_{x=\cos\theta} &= -\sin\theta, \\ P_2^1(x)|_{x=\cos\theta} &= -3\cos\theta\sin\theta, \\ P_3^1(x)|_{x=\cos\theta} &= -\frac{3}{2}(5\cos^2\theta - 1)\sin\theta, \end{aligned}$$

then $c_1 = -1$, $c_2 = -3\cos\theta$ and $c_3 = -\frac{3}{2}(5\cos^2\theta - 1)$. Together with (A.3), we can calculate all terms of c_n for $n > 2$. When $\theta = \pi$ and $n = 2$, the first three terms, $c_1 = -1$, $c_2 = 3$, and $c_3 = -6$, satisfy (A.1a). Assume that (A.1a) is true when $n = k$, then from (A.3) we have

$$\begin{aligned} c_{k+1} &= -\frac{2k+1}{k}c_k - \frac{k+1}{k}c_{k-1} \\ &= -\frac{2k+1}{k}\frac{k(k+1)}{2}(-1)^k - \frac{k+1}{k}\frac{k(k-1)}{2}(-1)^{k-1} \\ &= (-1)^{k+1}\frac{(k+1)(k+2)}{2} \end{aligned}$$

which is (A.1a) at $n = k + 1$. \square

The proof of (A.1b) relies on the recurrent relation

$$\sin\theta P_n^{1'}(x) = (n+1)\frac{P_{n-1}^1(x)}{\sin\theta} - n\cos\theta\frac{P_n^1(x)}{\sin\theta}$$

which can be rewritten as

$$\sin\theta P_n^{1'}(x) = (n+1)c_{n-1} - nxc_n. \quad (\text{A.4})$$

We can use c_n and (A.4) to calculate all terms of $\sin\theta P_n^{1'}(x)$ for $n > 1$ and $\sin\theta P_1^{1'}(x) = \cos\theta$. When $\theta = \pi$, (A.4) becomes

$$\begin{aligned} \sin\theta P_n^{1'}(\cos\theta) &= (n+1)\frac{n(n-1)}{2}(-1)^{n-1} + n\frac{n(n+1)}{2}(-1)^n \\ &= (-1)^n\frac{n(n+1)}{2} \end{aligned}$$

which is (A.1b). \square

References

- [1] A. M. Abbosh, M. E. Bialkowski, and S. Crozier, "Investigations into optimum characteristics for the coupling medium in UWB breast cancer imaging systems," in *Proc. IEEE International Symposium on Antennas and Propagation (AP-S'08)*, San Diego, CA, Jul. 2008.
- [2] "Agilent 2-Port and 4-Port PNA-X Network Analyzer: N5241A - 10 MHz to 13.5 GHz N5242A - 10 MHz to 26.5 GHz Data Sheet and Technical Specifications," Agilent Technologies, Santa Clara, CA.
- [3] O. E. Allen, D. A. Hill, and A. R. Ondrejka, "Time-domain antenna characterizations," *IEEE Trans. Electromagn. Compat.*, vol. 35, no. 3, pp. 339–336, Aug. 1993.
- [4] R. K. Amineh, A. Trehhan, and N. K. Nikolova, "TEM horn antenna for ultra-wideband microwave breast imaging," *Progress in Electromagnetics Research B*, vol. 13, pp. 59–74, 2009.
- [5] G. B. Arfken and H. J. Weber, *Mathematical Methods for Physicists*, 6th ed. Amsterdam, Holland: Academic Press, 2001.
- [6] A. Atalar, "Photoacoustic effect as a liquid absorbance detector," *Applied Optics*, vol. 19, no. 18, pp. 3204–3210, 1980.
- [7] C. A. Balanis, *Advanced Engineering Electromagnetics*. New York, NY: John Wiley & Sons, Inc., 1989.
- [8] G. Bellizzi, O. M. Bucci, and I. Catapano, "Magnetic nanoparticles as a contrast agent for microwave breast cancer imaging," in *Proc. European Conference on Antennas and Propagation (EuCAP'10)*, Barcelona, Spain, Apr. 2010.
- [9] C. F. Bohren and D. R. Huffman, *Absorption and Scattering of Light by Small Particles*. New York, NY: John Wiley & Sons, Inc., 1983.
- [10] E. J. Bond, X. Li, S. C. Hagness, and B. D. van Veen, "Microwave imaging via space-time beamforming for early detection of breast cancer," *IEEE Trans. Antennas Propag.*, vol. 51, pp. 1690–1705, 2003.

- [11] J. Bourqui, E. Fear, and M. Okoniewski, "Versatile ultrawideband sensor for near-field microwave imaging," in *Proc. European Conference on Antennas and Propagation (EuCAP'10)*, Barcelona, Spain, Apr. 2010.
- [12] J. Bourqui, M. Okoniewski, and E. C. Fear, "Balanced antipodal Vivaldi antenna with dielectric director for near-field microwave imaging," *IEEE Trans. Antennas Propag.*, vol. 58, no. 7, pp. 2318–2326, 2010.
- [13] L. Breiman, J. H. Friedman, R. A. Olshen, and C. J. Stone, *Classification and Regression Trees*. Belmont, CA: Wadsworth International Group, 1984.
- [14] T. Cameron, T. C. Williams, J. Bourqui, M. Okoniewski, and E. C. Fear, "Comparison of microwave and laser surface detection for microwave imaging systems," in *Proc. International Symposium on Antenna Technology and Applied Electromagnetics (ANTEM)'09*, Banff, Canada, Feb. 2009, pp. 1–4.
- [15] A. M. Campbell and D. V. Land, "Dielectric properties of normal and malignant human breast tissue measured *in vitro* at 3.2 GHz," *Physics in Medicine and Biology*, vol. 37, pp. 193–210, Jan. 1992.
- [16] Canadian Cancer Society, "Canadian cancer statistics 2009," 2009. [Online]. Available: <http://www.cancer.ca/canada-wide/about%20cancer/cancer%20statistics/%canadian%20cancer%20statistics.aspx>
- [17] S. S. Chaudhary, R. K. Mishra, A. Swarup, and J. M. Thomas, "Dielectric properties of normal and malignant human breast tissues at radiowave and microwave frequencies," *Indian Journal on Biochemistry and Biophysics*, vol. 21, pp. 76–79, 1984.
- [18] G. Chen, Z. Zhao, Z. Nie, and Q. H. Liu, "Computational study of time reversal mirror technique for microwave-induced thermo-acoustic tomography," *Journal of Electromagnetic Waves and Applications*, vol. 22, no. 16, pp. 2191–2204, 2008.
- [19] W. C. Chew, "Imaging and inverse problems in electromagnetics," in *Advances in Computational Electrodynamics - The Finite-Difference Time-Domain Method*, A. Taflov, Ed. Boston, MA: Artech House, 1998.
- [20] W. C. Chew and W. H. Weedon, "A 3-D perfectly matched medium from modified Maxwell's equations with stretched coordinates," *Microwave and optical technology letters*, vol. 7, no. 13, pp. 90–92, 1995.
- [21] W. C. Chew, *Waves and Fields in Inhomogeneous Media*. Piscataway, NJ: IEEE Press, 1995.
- [22] R. Ciocan and H. Jiang, "Model-based microwave image reconstruction: simulations and experiments," *Medical Physics*, vol. 31, no. 12, pp. 3231–3241, 2004.

- [23] K. S. Cole and R. H. Cole, "Dispersion and absorption in dielectrics - I. Alternating current characteristics," *Journal of Chemical Physics*, vol. 9, pp. 341–352, Apr. 1941.
- [24] M. Converse, E. J. Bond, B. D. van Veen, and S. C. Hagness, "A computational study of ultra-wideband versus narrowband microwave hyperthermia for breast cancer treatment," *IEEE Trans. Microw. Theory Tech.*, vol. 54, no. 5, pp. 2169–2180, 2006.
- [25] I. J. Craddock, M. Klemm, J. Leendertz, A. Preece, and R. Benjamin, "Development and application of a UWB radar system for breast imaging," in *Proc. Loughborough Antennas and Propagation Conference (LAPC'08)*, Loughborough, UK, Mar. 2008, pp. 24–27.
- [26] S. K. Davis, E. J. Bond, X. Li, S. C. Hagness, and B. D. van Veen, "Microwave imaging via space-time beamforming for early detection of breast cancer: beamformer design in the frequency domain," *Journal of Electromagnetic Waves and Applications*, vol. 17, no. 3, pp. 357–381, 2003.
- [27] S. K. Davis, H. Tandradinata, S. C. Hagness, and B. D. van Veen, "Ultrawideband microwave breast cancer detection: a detection-theoretic approach using the generalized likelihood ratio test," *IEEE Trans. Biomed. Eng.*, vol. 52, no. 7, pp. 1237–1250, 2005.
- [28] A. P. Dempster, N. M. Laird, and D. B. Rubin, "Maximum likelihood from incomplete data via the EM algorithm," *Journal of the Royal Statistical Society, Series B*, vol. 39, no. 1, pp. 1–38, 1977.
- [29] G. J. Diebold and T. Sun, "Properties of photoacoustic waves in one, two, and three dimensions," *Acustica*, vol. 80, no. 4, pp. 339–351, 1994.
- [30] M. Djordjević and B. M. Notarös, "Double higher order method of moments for surface integral equation model of metallic and dielectric antennas and scatterers," *IEEE Trans. Antennas Propag.*, vol. 52, no. 8, pp. 2118–2129, 2004.
- [31] F. A. Duck, *Physical properties of tissue: A comprehensive reference book*. San Diego, CA: Academic Press, 1990.
- [32] N. Duric, P. Littrup, L. Poulo, A. Babkin, R. Pevzner, E. Holsapple, O. Rama, and C. Glide, "Detection of breast cancer with ultrasound tomography: first results with the Computed Ultrasound Risk Evaluation (CURE) prototype," *Medical Physics*, vol. 34, no. 2, pp. 773–785, 2007.
- [33] M. El-Shenawee, "Resonant spectra of malignant breast cancer tumours using the three-dimensional electromagnetic multipole mode," *IEEE Trans. Biomed. Eng.*, vol. 51, no. 1, pp. 35–44, 2004.

- [34] B. Erdmann, J. Lang, and M. Seebass, "Optimization of temperature distributions for regional hyperthermia based on a nonlinear heat transfer model," *Annals of the New York Academy of Sciences*, vol. 858, pp. 36–46, 1998.
- [35] Q. Fang, "Computational methods for microwave medical imaging," Ph.D. dissertation, Dartmouth College, Dec. 2004.
- [36] Q. Fang, P. Meaney, S. Geimer, A. Streltsov, and K. Paulsen, "Microwave image reconstruction from 3-D fields coupled to 2-D parameter estimation," *IEEE Trans. Med. Imag.*, vol. 23, no. 4, pp. 475–484, 2004.
- [37] Q. Fang, P. M. Meaney, and K. D. Paulsen, "Microwave image reconstruction of tissue property dispersion characteristics utilizing multiple-frequency information," *IEEE Trans. Microw. Theory Tech.*, vol. 52, no. 8, pp. 1866–1875, Aug. 2004.
- [38] E. C. Fear, J. Sill, and M. A. Stuchly, "Experimental feasibility study of confocal microwave imaging for breast tumour detection," *IEEE Trans. Microw. Theory Tech.*, vol. 51, no. 3, pp. 887–892, 2003.
- [39] E. Fear and M. Stuchly, "Microwave detection of breast cancer," *IEEE Trans. Microw. Theory Tech.*, vol. 48, no. 11, pp. 1854–1863, 2000.
- [40] D. Feng, Y. Xu, G. Ku, and L. V. Wang, "Microwave-induced thermoacoustic tomography: reconstruction by synthetic aperture," *Medical Physics*, vol. 28, no. 12, pp. 2427–2431, 2001.
- [41] S. Gabriel, R. Lau, and C. Gabriel, "The dielectric properties of biological tissues. III. parametric models for the dielectric spectrum of tissues," *Physics in Medicine and Biology*, vol. 41, no. 11, pp. 2271–2293, 1996.
- [42] C. Geuzaine and J.-F. Remacle, *GMSH Reference Manual*, 2010, edition 2.5. [Online]. Available: <http://www.geuz.org/gmsh>
- [43] D. Gibbins, M. Klemm, I. Craddock, J. ALeendertz, A. Preece, and R. Benjamin, "A comparison of a wide-slot and a stacked patch antenna for the purpose of breast cancer detection," *IEEE Trans. Antennas Propag.*, vol. 58, no. 3, pp. 665 – 674, 2010.
- [44] B. Guo, J. Li, H. Zmuda, and M. Sheplak, "Multifrequency microwave induced thermal acoustic imaging for breast cancer detection," *IEEE Trans. Biomed. Eng.*, vol. 54, pp. 2000–2010, 2007.
- [45] R. Haberman, *Applied Partial Differential Equations: with Fourier Series and Boundary Value Problems*, 4th ed. Upper Saddle River, NJ: Prentice Hall, Inc., 2003.

- [46] S. C. Hagness, A. Taflove, and J. E. Bridges, "Wideband ultralow reverberation antenna for biological sensing," *IEE Electron. Lett.*, vol. 33, pp. 1594–1595, 1997.
- [47] —, "Two-dimensional FDTD analysis of a pulsed microwave confocal system for breast cancer detection: fixed-focus and antenna-array sensors," *IEEE Trans. Biomed. Eng.*, vol. 45, no. 12, pp. 1470–1479, 1998.
- [48] —, "Three-dimensional FDTD analysis of a pulsed microwave confocal system for breast cancer detection: design of an antenna-array element," *IEEE Trans. Antennas Propag.*, vol. 47, no. 5, pp. 783–791, 1999.
- [49] R. J. Halter, T. Zhou, P. M. Meaney, A. Hartov, R. J. Barth, Jr., K. M. Rosenkranz, W. A. Wells, C. A. Kogel, A. Borsic, E. J. Rizzo, and K. D. Paulsen, "The correlation of *in vivo* and *ex vivo* tissue dielectric properties to validate electromagnetic breast imaging: initial clinical experience," *Physiological Measurement*, vol. 30, no. 6, pp. S121–S136, Jun. 2009.
- [50] G. W. Hanson and A. B. Yakovlev, *Operator Theory for Electromagnetics: An Introduction*. New York, NY: Springer, 2001.
- [51] Z. Harmany, R. Willett, A. Singh, and R. Nowak, "Controlling the error in f-MRI: Hypothesis testing or set estimation?" in *Proc. IEEE International Symposium on Biomedical Imaging (ISBI'08)*, Paris, France, May 2008.
- [52] R. F. Harrington, *Time-Harmonic Electromagnetic Fields*. Piscataway, NJ: IEEE Press, 2001.
- [53] D. M. Healy, Jr. and J. B. Weaver, "Two applications of wavelet transforms in magnetic resonance imaging," *IEEE Trans. Inf. Theory*, vol. 38, no. 2, pp. 840–860, 1992.
- [54] W. R. Hendee and E. R. Ritenour, *Medical Imaging Physics*, 4th ed. New York, NY: John Wiley & Sons, Inc., 2002.
- [55] C. G. Hoelen and F. F. M. de Mul, "Image reconstruction for photoacoustic scanning of tissue structures," *Applied Optics*, vol. 39, no. 31, pp. 5872–5883, 2000.
- [56] J. H. Hubbell and S. M. Seltzer, "Tables of X-ray mass attenuation coefficients and mass energy-absorption coefficients from 1 keV to 20 MeV for elements $z = 1$ to 92 and 48 additional substances of dosimetric interest," 1996. [Online]. Available: <http://www.nist.gov/pml/data/xraycoef/index.cfm>
- [57] N. M. Hylton, "Breast magnetic resonance imaging techniques," in *Breast MRI: Diagnosis and Intervention*, E. A. Morris and L. Liberman, Eds. New York, NY: Springer Science+Business Media, Inc., 2005.

- [58] *IEEE Standard Letter Symbols for Quantities Used in Electrical Science and Electrical Engineering*, IEEE Std., 1991.
- [59] *IEEE Standard for Safety Levels with Respect to Human Exposure to Radio Frequency Electromagnetic Fields, 3 kHz to 300 GHz*, IEEE Std., 2005.
- [60] A. Ishimaru, *Electromagnetic Wave Propagation, Radiation, and Scattering*. Upper Saddle River, NJ: Prentice Hall, Inc., 1991.
- [61] J. D. Jackson, *Classical Electrodynamics*, 3rd ed. New York, NY: John Wiley & Sons, Inc., 1998.
- [62] V. P. Jackson, R. E. Hendrick, S. A. Feig, and D. B. Kopans, "Imaging of the radio-graphically dense breast," *Radiology*, vol. 188, no. 2, pp. 297–301, Aug. 1993.
- [63] H. Jiang, C. Li, D. Pearlstone, and L. L. Fajardo, "Ultrasound-guided microwave imaging of breast cancer: tissue phantom and pilot clinical experiments," *Medical Physics*, vol. 32, no. 8, pp. 2528–2535, 2005.
- [64] H. E. Johns and J. R. Cunningham, *The Physics of Radiology*, 4th ed. Springfield, IL: Charles C. Thomas Books, 1983.
- [65] D. H. Johnson and D. E. Dudgeon, *Array Signal Processing: Concepts and Techniques*. Upper Saddle River, NJ, USA: Prentice Hall, Inc., 1993.
- [66] W. T. Joines, Y. Zhang, C. Li, and R. L. Jirtle, "The measured electrical properties of normal and malignant human tissues from 50 to 900 MHz," *Medical Physics*, vol. 21, no. 4, pp. 547–550, 1994.
- [67] H. Kanj and M. Popović, "A novel ultra-compact broadband antenna for microwave breast tumour detection," *Progress in Electromagnetics Research*, vol. 86, pp. 169–198, 2008.
- [68] L. E. Kinsler, A. R. Frey, A. B. Coppens, and J. V. Sanders, *Fundamentals of Acoustics*, 4th ed. New York, NY: John Wiley & Sons, Inc., 2000.
- [69] W. L. Kiser, Jr., "Numerical simulations of the thermoacoustic computed tomography breast imaging system," Ph.D. dissertation, Purdue University, 1999.
- [70] M. Klemm, I. Craddock, J. Leendertz, D. Gibbins, M. Shere, A. Preece, and R. Benjamin, "Clinical trials of a UWB imaging radar for breast cancer," in *Proc. European Conference on Antennas and Propagation (EuCAP'10)*, Barcelona, Spain, Apr. 2010.

- [71] M. Klemm, I. Craddock, J. Leendertz, A. Preece, and R. Benjamin, "Experimental and clinical results of breast cancer detection using UWB microwave radar," in *Proc. IEEE International Symposium on Antennas and Propagation (AP-S'08)*, San Diego, CA, Jul. 2008.
- [72] M. Klemm, I. J. Craddock, A. Preece, J. Leendertz, and R. Benjamin, "Evaluation of a hemi-spherical wideband antenna array for breast cancer imaging," *Radio Science*, vol. 43, no. 6, p. RS6S06, Dec. 2008.
- [73] M. Klemm, J. Leendertz, A. Preece, M. Shere, I. Craddock, and R. Benjamin, "Clinical experience of breast cancer imaging using UWB microwave radar system at bristol," in *Proc. IEEE International Symposium on Antennas and Propagation (AP-S'10)*, Toronto, Canada, Jul. 2010.
- [74] M. Klemm, J. A. Leendertz, D. Gibbins, I. J. Craddock, A. Preece, and R. Benjamin, "Microwave radar-based differential breast cancer imaging: Imaging in homogeneous breast phantoms and low contrast scenarios," *IEEE Trans. Antennas Propag.*, vol. 58, no. 7, pp. 2337–2344, 2010.
- [75] P. Kosmas and C. M. Rappaport, "Time reversal with the FDTD method for microwave breast cancer detection," *IEEE Trans. Microw. Theory Tech.*, vol. 53, no. 7, pp. 2317–2323, 2005.
- [76] P. Kosmas and C. Rappaport, "FDTD-based time reversal for microwave breast cancer detection-localization in three dimensions," *IEEE Trans. Microw. Theory Tech.*, vol. 54, no. 4, pp. 1921–1927, 2006.
- [77] R. A. Kruger, W. L. Kiser Jr., K. D. Miller, and H. E. Reynolds, "Thermoacoustic ct: imaging principles," in *Proc. SPIE*, vol. 3916, 2000, pp. 150–159.
- [78] R. A. Kruger, K. K. Kopecky, A. M. Aisen, D. R. Reinecke, G. A. Kruger, and W. L. Kiser, Jr., "Thermoacoustic CT with radio waves: a medical imaging paradigm," *Radiology*, vol. 211, no. 1, p. 275278, 1999.
- [79] R. A. Kruger, D. R. Reinecke, and G. A. Kruger, "Thermoacoustic computed tomography-technical considerations," *Medical Physics*, vol. 26, no. 9, pp. 1832–1837, Sep. 1999.
- [80] R. A. Kruger, K. Stantz, and W. L. Kiser, Jr., "Thermoacoustic CT of the breast," in *Proc. SPIE*, vol. 4682, 2002, pp. 521–525.
- [81] C. Kuhl, "The current status of breast MR imaging part I. choice of technique, image interpretation, diagnostic accuracy, and transfer to clinical practice," *Radiology*, vol. 244, no. 8, pp. 356–378, Aug. 2007.

-
- [82] ———, “The current status of breast MR imaging part II. clinical applications,” *Radiology*, vol. 244, no. 8, pp. 672–691, Sep. 2007.
 - [83] A. Lazaro, D. Girbau, and R. Villarino, “Wavelet-based breast tumor localization technique using a UWB radar,” *Progress In Electromagnetics Research*, vol. 98, pp. 75–95, 2009.
 - [84] M. Lazebnik, L. McCartney, D. Popovic, C. B. Watkins, M. J. Lindstrom, J. Harter, S. Sewall, A. Magliocco, J. H. Booske, M. Okoniewski, and S. C. Hagness, “A large-scale study of the ultrawideband microwave dielectric properties of normal breast tissue obtained from reduction surgeries,” *Physics in Medicine and Biology*, vol. 52, no. 10, pp. 2637–2656, 2007.
 - [85] M. Lazebnik, M. Okoniewski, J. H. Booske, and S. C. Hagness, “Highly accurate Debye models for normal and malignant breast tissue dielectric properties at microwave frequencies,” *IEEE Microw. Wireless Compon. Lett.*, vol. 17, no. 12, pp. 822–824, 2007.
 - [86] M. Lazebnik, D. Popovic, L. McCartney, C. B. Watkins, M. J. Lindstrom, J. Harter, S. Sewall, T. Ogilvie, A. Magliocco, T. M. Breslin, W. Temple, D. Mew, J. H. Booske, M. Okoniewski, and S. C. Hagness, “A large-scale study of the ultrawideband microwave dielectric properties of normal, benign and malignant breast tissues obtained from cancer surgeries,” *Physics in Medicine and Biology*, vol. 52, no. 20, pp. 6093–6115, 2007.
 - [87] X. Li, E. J. Bond, B. D. van Veen, and S. Hagness, “An overview of ultra-wideband microwave imaging via space-time beamforming for early-stage breast-cancer detection,” *IEEE Antennas Propag. Mag.*, vol. 47, no. 1, pp. 19–34, 2005.
 - [88] X. Li, S. K. Davis, S. C. Hagness, D. W. van der Weide, and B. D. van Veen, “Microwave imaging via space-time beamforming: experimental investigation of tumor detection in multilayer breast phantoms,” *IEEE Trans. Microw. Theory Tech.*, vol. 52, no. 8, pp. 1856–1865, 2004.
 - [89] X. Li and S. C. Hagness, “A confocal microwave imaging algorithm for breast cancer detection,” *IEEE Microw. Wireless Compon. Lett.*, vol. 11, no. 3, pp. 130–132, 2001.
 - [90] X. Li, S. C. Hagness, M. K. Choi, and D. W. van der Weide, “Numerical and experimental investigation of an ultrawideband ridged pyramidal horn antenna with curved launching plane for pulse radiation,” *IEEE Antennas Wireless Propag. Lett.*, vol. 2, no. 1, pp. 259–262, 2003.

- [91] H. B. Lim, N. T. T. Nhung, E.-P. Li, and N. D. Thang, "Confocal microwave imaging for breast cancer detection: delay-multiply-and-sum image reconstruction algorithm," *IEEE Trans. Biomed. Eng.*, vol. 55, no. 6, pp. 1697–1704, 2008.
- [92] Q. H. Liu, Z. Q. Zhang, T. T. Wang, J. A. Bryan, G. A. Ybarra, L. W. Nolte, and W. T. Joines, "Active microwave imaging I: 2-D forward and inverse scattering methods," *IEEE Trans. Microw. Theory Tech.*, vol. 50, no. 1, pp. 123–133, 2002.
- [93] S. Manohar, S. E. Vaartjes, J. C. G. van Hespén, J. M. Klaase, F. M. van den Engh, W. Steenbergen, and T. G. van Leeuwen, "Initial results of *in vivo* non-invasive cancer imaging in the human breast using near-infrared photoacoustics," *Optic Express*, vol. 15, no. 19, 2007.
- [94] A. Mashal, B. Sitharaman, X. Li, P. K. Avti, A. V. Sahakian, J. H. Booske, and S. C. Hagness, "Toward carbon-nanotube-based theranostic agents for microwave detection and treatment of breast cancer: enhanced dielectric and heating response of tissue-mimicking materials," *IEEE Trans. Biomed. Eng.*, vol. 57, no. 8, pp. 1831–1834, 2010.
- [95] A. Mashal, J. H. Booske, and S. C. Hagness, "Toward contrast-enhanced microwave-induced thermoacoustic imaging of breast cancer: an experimental study of the effects of microbubbles on simple thermoacoustic targets," *Physics in Medicine and Biology*, vol. 54, pp. 641–650, 2009.
- [96] T. D. Mast, "Empirical relationships between acoustic parameters in human soft tissues," *Acoustics Research Letters Online*, vol. 37, no. 1, pp. 37–43, 2000.
- [97] —, "Two- and three-dimensional simulations of ultrasonic propagation through human breast tissue," *Acoustics Research Letters Online*, vol. 3, no. 2, pp. 53–58, 2002.
- [98] P. M. Meaney, K. D. Paulsen, and J. T. Chang, "Near-field microwave imaging of biologically-based materials using a monopole transceiver system," *IEEE Trans. Microw. Theory Tech.*, vol. 46, no. 1, pp. 31–45, 1998.
- [99] P. M. Meaney, K. D. Paulsen, J. T. Chang, M. W. Fanning, and A. Hartov, "Non-active antenna compensation for fixed-array microwave imaging—Part II: imaging results," *IEEE Trans. Med. Imag.*, vol. 18, no. 6, pp. 508–518, 1999.
- [100] P. M. Meaney, S. A. Pendergrass, M. W. Fanning, D. Li, and K. D. Paulsen, "Importance of using a reduced contrast coupling medium in 2-D microwave breast imaging," *Journal of Electromagnetic Waves and Applications*, vol. 17, no. 2, pp. 333–355, 2003.

-
- [101] P. M. Meaney, T. Raynolds, L. Potwin, and K. D. Paulsen, "3-point support mechanical steering system for high intensity focused ultrasound," *Physics in Medicine and Biology*, vol. 52, no. 11, pp. 3045–3056, 2007.
- [102] P. M. Meaney, K. D. Paulsen, B. W. Pogue, and M. I. Miga, "Microwave image reconstruction utilizing log-magnitude and unwrapped phase to improve high-contrast object recovery," *IEEE Trans. Med. Imag.*, vol. 20, no. 2, pp. 104–116, 2001.
- [103] P. M. Meaney, T. Zhou, M. W. Fanning, and S. D. G. K. D. Paulsen, "Microwave thermal imaging of scanned focused ultrasound heating: phantom results," *International Journal of Hyperthermia*, vol. 24, no. 7, pp. 523–536, 2008.
- [104] P. Meaney, Q. Fang, T. Rubæk, E. Demidenko, and K. Paulsen, "Log transformation benefits parameter estimation in microwave tomographic imaging," *Medical Physics*, vol. 34, no. 6, pp. 2014–2023, 2007.
- [105] National Cancer Institute. [Online]. Available: <http://training.seer.cancer.gov/breast/anatomy/>
- [106] J. Nocedal and S. J. Wright, *Numerical Optimization*, 2nd ed. New York, NY: Springer, 2006.
- [107] R. D. Nowak, "Wavelet-based Rician noise removal for magnetic resonance imaging," *IEEE Trans. Image Process.*, vol. 8, no. 10, pp. 1408–1419, 1999.
- [108] P. olof Persson and G. Strang, "A simple mesh generator in MATLAB," *SIAM Review*, vol. 46, no. 2, pp. 329–345, 2004.
- [109] A. A. Oraevsky and A. A. Karabutov, "Optoacoustic tomography," in *Biomedical Photonics Handbook*, T. Vo-Dinh, Ed. Boca Raton, FL: CRC Press, 2003, ch. 34, pp. 34–1–34–34.
- [110] W. H. Parsons, *Cancer of the Breast*. Springfield, IL: Charles C. Thomas Books, 1959.
- [111] K. D. Paulsen and P. M. Meaney, "Nonactive antenna compensation for fixed-array microwave imaging—Part I: model development," *IEEE Trans. Med. Imag.*, vol. 18, no. 6, pp. 496–507, Jun. 1999.
- [112] H. H. Pennes, "Analysis of tissue and arterial blood temperature in the resting human forearm," *Journal of Applied Physiology*, vol. 1, no. 2, pp. 93–122, Aug. 1948.
- [113] S. P. Poplack, K. Paulsen, A. Hartov, P. Meaney, B. Pogue, T. Tosteson, M. Grove, S. Soho, and W. Wells, "Electromagnetic breast imaging: average tissue property values in women with negative clinical findings," *Radiology*, vol. 231, pp. 571–580, 2004.

- [114] M. Pramanik, “Dual-modality thermoacoustic and photoacoustic imaging,” Ph.D. dissertation, Washington University in St. Louis, 2010.
- [115] M. Pramanik, G. Ku, C. Li, and L. V. Wang, “Design and evaluation of a novel breast cancer detection system combining both thermoacoustic (TA) and photoacoustic (PA) tomography,” *Medical Physics*, vol. 35, no. 6, pp. 2218–2223, 2008.
- [116] J. L. Prince and J. M. Links, *Medical Imaging Signals and Systems*. Upper Saddle River, NJ: Prentice Hall, Inc., 2006.
- [117] C. Rappaport, “Determination of bolus dielectric constant for optimum coupling of microwaves through skin for breast cancer imaging,” *International Journal of Antennas and Propagation*, vol. 2008, pp. 1–5, 2008.
- [118] M. P. Robinson, M. J. Richardson, J. L. Green, and A. W. Preece, “New materials for dielectric simulation of tissues,” *Physical and Medical Biology*, vol. 36, no. 12, pp. 1565–1571, 1991.
- [119] T. Rubæk, O. S. Kim, , and P. Meincke, “Computational validation of a 3-D microwave imaging system for breast-cancer screening,” *IEEE Trans. Antennas Propag.*, vol. 57, no. 7, pp. 2105–2115, 2009.
- [120] Z. S. Sacks, D. M. Kingsland, R. Lee, and J. F. Lee, “Perfectly matched anisotropic absorber for use as an absorbing boundary condition,” *IEEE Trans. Antennas Propag.*, vol. 43, p. 12, 1995.
- [121] S. M. Salvador and G. Vecchi, “Experimental tests of microwave breast cancer detection on phantoms,” *IEEE Trans. Antennas Propag.*, vol. 57, no. 6, pp. 1705–1712, 2009.
- [122] A. Samani and D. Plewes, “An inverse problem solution for measuring the elastic modulus of intact *ex vivo* breast tissue tumours,” *Physics in medicine and biology*, vol. 52, no. 5, pp. 1247–1260, 2007.
- [123] A. Samani, J. Zubovits, and D. Plewes, “Elastic moduli of normal and pathological human breast tissues: an inversion-technique-based investigation of 169 samples,” *Physics in Medicine and Biology*, vol. 52, pp. 1565–1576, 2007.
- [124] *SEMCAD-X Reference Guide*, Schmid & Partner Engineering AG, Zurich, Switzerland, 2008, release 14.2.
- [125] C. D. Scott, R. M. Willett, and R. D. Nowak, “CORT: Classification or regression trees,” in *Proc. IEEE International Conference on Acoustics, Speech, Signal Processing*, Hong Kong, China, Apr. 2003.

- [126] J. Shea, P. Kosmas, S. Hagness, and B. van Veen, "Contrast-enhanced microwave imaging of breast tumors: A computational study using 3-D realistic numerical phantoms," *Inverse Problems*, vol. 26, no. 074009, 2010.
- [127] J. M. Sill and E. C. Fear, "Tissue sensing adaptive radar for breast cancer detection: experimental investigation of simple tumour models," *IEEE Trans. Microw. Theory Tech.*, vol. 53, no. 11, pp. 3312–3319, 2005.
- [128] J. A. Stratton, *Electromagnetic Theory*. New York, NY: McGraw-Hill Companies Inc., 1941.
- [129] A. J. Surowiec, S. S. Stuchly, J. R. Barr, and A. Swarup, "Dielectric properties of breast carcinoma and the surrounding tissues," *IEEE Trans. Biomed. Eng.*, vol. 35, no. 4, pp. 257–263, 1988.
- [130] A. Taflove and S. C. Hagness, Eds., *Computational Electrodynamics: the Finite-Difference Time-Domain Method*, 3rd ed. Boston, MA: Artech House, 2005.
- [131] "AMIRA User's Guide," Visage Imaging, Berlin, Germany, 2009, release 4.3.
- [132] J. Werner and M. Buse, "Temperature profiles with respect to inhomogeneity and geometry of the human body," *Journal of Applied Physiology*, vol. 63, no. 3, pp. 1110–1118, 1988.
- [133] W. Wiesbeck, G. Adamiuk, and C. Sturm, "Basic properties and design principles of UWB antennas," *Proc. IEEE*, vol. 97, no. 2, pp. 372–385, 2009.
- [134] T. C. Williams, J. M. Sill, J. Bourqui, and E. C. Fear, "Tissue sensing adaptive radar for breast cancer detection: Practical improvements," in *Proc. IEEE International Symposium on Antennas and Propagation (AP-S'10)*, Toronto, Canada, Jul. 2010.
- [135] T. C. Williams, J. M. Sill, and E. C. Fear, "Breast surface estimation for radar-based breast imaging systems," *IEEE Trans. Biomed. Eng.*, vol. 55, no. 6, pp. 1678 – 1686, 2008.
- [136] D. W. Winters, J. Shea, E. L. Madsen, G. Frank, B. van Veen, and S. Hagness, "Estimating the breast surface using UWB microwave monostatic backscatter measurements," *IEEE Trans. Biomed. Eng.*, vol. 55, no. 1, pp. 247–256, 2008.
- [137] W. J. Wiscombe, "Improved Mie scattering algorithms," *Applied Optics*, vol. 19, no. 9, pp. 1505–1509, 1980.
- [138] Y. Xie, B. Guo, J. Li, G. Ku, and L. V. Wang, "Adaptive and robust methods of reconstruction for thermoacoustic tomography," *IEEE Trans. Biomed. Eng.*, vol. 55, pp. 2741–2842, 2008.

-
- [139] Y. Xie, B. Guo, L. Xu, J. Li, and P. Stoica, "Multistatic adaptive microwave imaging for early breast cancer detection," *IEEE Trans. Biomed. Eng.*, vol. 53, no. 8, pp. 1647–1657, 2006.
- [140] M. Xu and L. V. Wang, "Pulsed-microwave-induced thermoacoustic tomography: filtered backprojection in a circular measurement configuration," *Medical Physics*, vol. 29, pp. 1661–1669, 2002.
- [141] Y. Xu, D. Feng, and L. V. Wang, "Exact frequency-domain reconstruction for thermoacoustic tomography—I: planar geometry," *IEEE Trans. Med. Imag.*, vol. 21, no. 7, pp. 823–828, Jul. 2002.
- [142] Y. Xu, M. Xu, and L. V. Wang, "Exact frequency-domain reconstruction for thermoacoustic tomography—II: cylindrical geometry," *IEEE Trans. Med. Imag.*, vol. 21, no. 7, pp. 829–833, Jul. 2002.
- [143] S. Yang, H. Kim, and H. J. Lee, "Circular-harmonic vector analysis of dielectric waveguide with a cross-cut-circle cross section," *Applied Optics*, vol. 34, pp. 7705–7713, Nov. 1995.
- [144] G. Ye, "PSTD method for thermoacoustic tomography (TAT) and related experimental investigation," Ph.D. dissertation, Duke University, 2009.
- [145] K. Yee, "Numerical solution of initial boundary value problems involving Maxwell's equations in isotropic media," *IEEE Trans. Antennas Propag.*, vol. 14, no. 3, pp. 302–307, 1966.
- [146] C. Yu, M. Yuan, J. Stang, E. Bresslour, R. George, G. Ybarra, W. Joines, and Q. H. Liu, "Active microwave imaging II: 3-D system prototype and image reconstruction from experimental data," *IEEE Trans. Microw. Theory Tech.*, vol. 56, no. 4, pp. 991–1000, 2008.
- [147] E. Zastrow, S. K. Davis, M. Lazebnik, F. Kelcz, B. D. van Veen, and S. C. Hagness, "Development of anatomically realistic numerical breast phantoms with accurate dielectric properties for modelling microwave interactions with the human breast," *IEEE Trans. Biomed. Eng.*, vol. 55, no. 12, pp. 2792–2800, 2008.
- [148] S. Zhang and J. Jin, *Computation of Special Functions*. New York, NY: John Wiley & Sons, Inc., 1996.
- [149] M. Zhao, J. Shea, S. Hagness, D. van der Weide, B. D. van Veen, and T. Varghese, "Numerical study of microwave scattering in breast tissue via coupled dielectric and elastic contrasts," *IEEE Antennas Wireless Propag. Lett.*, vol. 7, pp. 247–250, 2008.